UNIVERSITY OF SOUTHAMPTON

SHEAR CRACK INITIATION AND PROPAGATION IN FOAM CORE SANDWICH STRUCTURES

by Philippe Noury

Faculty of Engineering and Applied Science

DEPARTMENT OF SHIP SCIENCE

Doctorate of Philosophy

April 2000

UNIVERSITY OF SOUTHAMPTON

ABSTRACT

FACULTY OF ENGINEERING AND APPLIED SCIENCE
DEPARTMENT OF SHIP SCIENCE
Doctorate of Philosophy
SHEAR CRACK INITIATION AND PROPAGATION IN FOAM CORE SANDWICH STRUCTURES
by Philippe Noury

The subject of this thesis was on the fatigue and fracture behaviour of PVC cellular foam core materials used in sandwich constructions. The investigation was restricted to a special type of PVC called cross-linked after their chemical structure. The mechanical and physical characteristics of the material tested throughout the investigation were typical of the one used in the marine industry.

The first investigation reports on mixed-mode fracture in rigid cellular PVC foam based on experimental and numerical analyses. Experiments were performed on sharp-cracked specimens using the compact-tension-shear (CTS) test loading device. Foams of three different densities were tested. The CTS specimen was, in association with a special loading device, an appropriate apparatus for experimental mixed-mode fracture analysis. Experimentally obtained fracture toughness results show good consistency. K_{IC} fracture toughness was marginally different in different directions. The ratio K_{IIC}/K_{IC} was found to be between 0.4 and 0.65 depending on the foam density. For mixed-mode loading, Richard's criterion - using experimentally obtained K_{IIC} and K_{IC} - was the best in predicting accurately fracture locus and fracture angle. When no experimental data were used, the maximum tangential stress criterion predicted best kinking angle. The principal strain criterion predicted the best fracture locus. Fracture boundary curve and kinking angle were best predicted for low mode-II contribution. The theory appeared to be deficient in predicting accurately both fracture locus and fracture angle.

The fatigue crack growth in rigid PVC cellular foam under combined mode-I and mode-II loading was then investigated. Experiments were performed on sharp-cracked specimens using the same CTS test technique, as in the previous investigation. Loading conditions ranging from pure mode-I (opening mode), mixed-mode, to pure mode-II (shearing mode), were generated using a simple loading device. Linear elastic fracture mechanics (LEFM) and plane strain conditions were assumed. Crack path γ, da/dN versus ΔK and crack growth behaviour for each loading condition were ascertained. Fatigue data were compared with results obtained from static tests in similar configurations. A refined fatigue and fracture process model was proposed.

The final experimental investigation reported on flexural fatigue in glass-reinforced-plastic (GRP) sandwich foam core beams using a 4-point-bending (4PTB) test specimen. S-N curves, load-deflection and load-strain history curves compared well with independent results. The flexural fatigue was characterised by 2 regimes: a creep regime inducing small permanent deformation followed by fatigue and fracture regime, typically much sorter, responsible for a catastrophic shear stiffness degradation. Damage formation, crack initiation and growth were described for both single and multiple shear cracks. Mode-I crack propagation rates were found to reach 10^{-2} mm/cycle towards the end of the fatigue life, and compared well with previous results obtained from the CTS specimen. Fatigue crack growth in a 4PTB foam cored sandwich beams can be considered to be K_I-controlled. Initial crack propagation angle of 65° was in agreement with earlier investigations.

The numerical investigation reports on the fracture behaviour of single shear crack in foam core sandwich beams. A generic sandwich structure with symmetrical isotropic facing

bonded to thick homogeneous and isotropic PVC foam core was examined. A numerical study was carried out using a multi-purpose finite element package. The work was concentrated on cracks embedded in the core material itself. LEFM and plane strain conditions are assumed. Strain energy release rate G was determined for a range of physical and mechanical properties, characteristic of a typical sandwich beam. The relationship between mixed-mode toughnesses, K_I and K_{II}, was also characterised. Finally, the numerical results were compared to a set of experimental data on mixed-mode fracture toughness testing and 4PTB. A fracture envelope and stress intensity factor variations were deduced for the structure under consideration.

KEY WORDS

PVC foam - shear cracks - mixed-mode - sandwich construction- toughness - fracture - CTS testing - finite element analysis - cellular material - fatigue - crack growth - 4PTB

LIST OF CONTENTS

LIST OF TABLES

LIST OF FIGURES

PREFACE

At the end of the M.Sc. Course undertaken in naval architecture, Professor Ajit Shenoi proposed me to join the Composite Materials Group at the Department of Ship Science in the University of Southampton. The boundaries of the subject, I was given, were simple: composite materials and naval architecture.

Having spent the last 5 previous years studying and working on yachts and small crafts design, I decided to look more closely at the problems of shear cracks in PVC cellular foam sandwich structures. The subject was already a popular one and a very much spoken one by skippers, yacht designers, naval architects, researchers and students. It is a common practical problem with little academic-type research done on the topic: it reflects the bridge between pure research and practical application.

The work gathered in this doctoral thesis has been carried out at the Department of Ship Science between February 1996 and February 1999. During the spring of 1996, I was given the opportunity to go and study at the Department of Naval Architecture and Offshore Engineering in the Technical University of Denmark. The contents of the background and literature review chapters were mainly written at this stage.

At the end of spring 1997, I was invited by Professor Karl-Axel Olsson to come and visit the Lightweight Structures Division of the Department of Aeronautics at the Royal Institute of Technology in Stockholm for few days. Researchers from this department have largely contributed to the subject of sandwich structures over the last twenty years. This visit gave me the chance to meet Doctor Dan Zenkert and Doctor Stephan Hallström, and compare my work on the fracture mechanics of PVC foam, presented in Chapter 4, with their work. The emphasis placed by this department on high standard of research helped me to put my own work into its proper perspective.

In February 1999, I moved to Norway and it is there that I progressively managed to finish the write up of the final version of the thesis.

Oslo, February 2000.

Philippe Noury

ACKNOWLEDGEMENTS

Such a project, as a Ph.D. thesis, would not have been possible without the help and co-operation from a number of people. I want to thank Professor Gerant Price, the head of the Ship Science department, and Professor Ajit Shenoi, my supervisor, for making possible this doctoral thesis. I also want to thank Professor Peter Gregson and Doctor Ian Sinclair from the department of Engineering Materials for their collaborations and enthusiasm; the experimental investigations have been entirely carried out in the Engineering Materials laboratories.

I would like to thank Professor Juncher Jensen, Doctor Hans-Jurgen Riber and everyone of the department of Ocean Engineering at the Technical University of Denmark, Lyngby, for their hospitality and kindness during my stay there.

I also take the opportunity to thank everyone, especially Professor Olsson, Doctor Dan Zenkert and Doctor Stephan Hallström from the Royal Institute of Technology, Stockholm.

Additionally, the experimental investigations would not have been possible without the precious assistance of the University's technicians. I would like to thank especially Dave Goldsworthy and Chris Norvall in this respect.

I would also like to thank my fellow students and researchers, Ketut Utama, Martin Prince, Frederic Louarn, Simon Clark and numerous housemates for their constant encouragement and good humour.

Finally, but most, I would like to thank my family and Lisa.

NOMENCLATURE

a	:	crack length
b	:	beam breadth
b	:	beam width
B(z)	:	second moment of area
c_i	:	constant
d	:	distance between the neutral axis of faces
d*	:	distance between crack tip on upper interface and beam end
D	:	flexural rigidity
D_0	:	flexural rigidity of face about the beam neutral axis
e	:	distance between the neutral axis of the beam and the interface core/face
E	:	Young's modulus
f(a/w)	:	geometrical factor
f_I	:	mode-I geometrical factor
f_{II}	:	mode-II geometrical factor
g(φ)	:	general solution of bi-harmonic solution
G	:	shear modulus
G	:	strain energy release rate
h	:	beam height
k	:	Shear factor
K_{IC}	:	fracture toughness in mode-I
K_{IIC}	:	fracture toughness in mode-II
K_I	:	ModeI stress intensity factor
k_I	:	local mode-I stress intensity factor
K_{II}	:	Mode-II stress intensity factor
k_{II}	:	local mode-II stress intensity factor
ΔK	:	K_{max}-K_{min}
K_Q	:	provisional fracture toughness evaluated from P_Q
K_{cyclic}	:	K_{max} at fracture
$K_V(\psi)$	:	equivalent fracture toughness
L*	:	45° maximum shear crack length between the interface, or $\sqrt{2}$ c
M_x	:	bending moment
N_x	:	axial load
P	:	load
P_{max}	:	maximum load
P_Q	:	apparent crack initiation load
q(x)	:	distributed load
t	:	thickness
t_f	:	face thickness
t_c	:	core thickness
r	:	radial polar co-ordinate
R	:	rotary inertia
R	:	P_{min} / P_{max} ratio, or K_{min} / K_{max}
S	:	strain energy density factor
S	:	shear stiffness
t	:	time
T_x	:	shear force
w	:	specimen width
w	:	total deformation
w_b	:	deformation due to bending
w_s	:	deformation due to shear

x-dir.	:	longitudinal direction, rolling direction manufacturing
y-dir.	:	transverse direction, perpendicular to rolling direction
z	:	co-ordinate
α	:	loading angle on CTS loading device
α_1	:	fracture toughness ratio, $\alpha_I = K_{II}/ K_I$
α_1	:	parameter equal to experimentally-obtained K_{IC}/K_{IIC}
α_{ij}	:	scalar parameter
β_{eq}	:	equivalent crack angle, β_{eq} = Arctan (K_I/K_{II})
δ	:	displacement given by extensometer
ε_z	:	strain in z-direction
φ	:	angular polar co-ordinate
φ_c	:	criterion dependent critical value at which a crack initiates, polar co-ordinates
φ	:	angular polar co-ordinate
κ	:	$\kappa=(3-4\nu)$
κ	:	$\kappa=(3-\nu)/(1+\nu)$
λ	:	strength of the singularity
ν	:	Poisson's ratio - taken equal to 0.32 for the foams under considerations
τ	:	shear stress or shear strength
σ	:	direct stress
σ_y	:	yield strength equals to strength at 0.2% offset of strain
σ_i	:	principal normal stress, (i=1,2,3)
σ_V	:	equivalent stress
ρ	:	density
ρ_{rel}	:	relative density, ρ_{foam} / $\rho_{polymeric\ material}$
ρ^*	:	surface mass
Φ	:	Airy stress function
ψ	:	kinking angle
$0(r)$	:	negligible term
c	:	subscript c refers to the core
f	:	subscript f refers to the face
tens	:	subscript tens refers to tensile properties
comp	:	subscript comp refers to compressive properties
ult	:	subscript ult refers to ultimate properties
limit	:	subscript limit refers to properties taken at the upper end of the linear range

1 INTRODUCTION

Composites structures based on lightweight composite materials bonded to a low-density core are presently being used in a large number of applications where weight, stiffness and strength are primary design requirements. Sandwich structures are now commonly used in structural components ranging from the rotor blade of helicopters to the hull shell of racing yachts.

Traditionally, the design of structures and sandwich structures for marine applications is principally based on a strength-of-materials approach, with stiffness and stability criteria forming constraining influences. The two possible modes of failure taken into account are yielding or excessive plastic deformations. However, it was found that structures, designed according to the first two modes, very often failed in a sudden manner due to unstable crack propagation.

In marine applications, some high speed craft, having sandwich hulls with Fibre-reinforced-plastic (FRP) laminate and foam polymer cores, have experienced damage that is believed to be due to repeated slamming loads. The load characteristics encountered in these cases has caused cyclic stresses and has resulted in consequential core fracture.

Fatigue behaviour and fracture of foam core have not been significantly studied and reported in the literature, in recent years. However, some research work has been carried out on fracture analyses of various sandwich core materials and face/core interface layers.

1.1 Sandwich structures

1.1.1 Sandwich concept

The ASTM defines a sandwich structure as follows[1]:

"A structural sandwich is a special form of a laminated composite comprising of a combination of different materials that are bonded to each other so as to utilise the properties of each separate component to the structural advantage of the whole assembly."

A sandwich structure is typically composed of 3 main parts as shown in Figure 1.

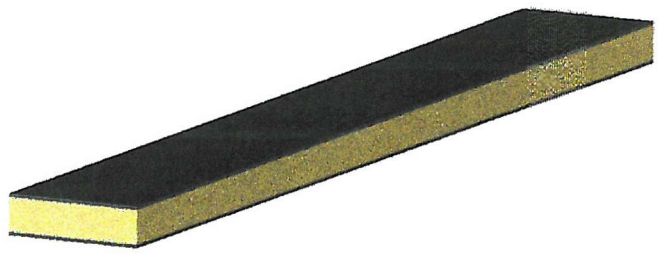

Figure 1: Typical sandwich beam

It consists of two thin stiff and strong layers of dense material separated by a thick layer of low-density material, which is much less stiff and strong. The core is bonded to the faces by an adhesive whose function is to transfer the load between the components. The characteristics of a sandwich structure are identical to an I-beam. "Most" of the material is situated away from the neutral axis. Just enough material is left in the middle to make the whole structure work. This allows the assembly to resist shear and buckling. The main benefit of such a structure is the high stiffness and strength to weight ratios. There are additional advantages such as acoustic and thermal insulation, high-energy absorption, manufacturing process and buoyancy. Research into sandwich structures has revolved primarily around the areas of theory, failure modes and envelopes, optimisation and design procedures, finite element modelling, impact resistance, fatigue and fracture analysis. Disadvantages should also not be overlooked by engineers and scientists. Some typical drawbacks are the newness of production methods, a complicated quality control, the lack of understanding of load introduction and joining, and the lack of knowledge concerning the effect of damage.

1.1.2 Marine applications of sandwich structures

The first serious use of FRP for boat construction appears to have been made by the US Navy in the early 1940s[2]. Development of hand lay-up techniques employing cold-cure polyester resin with E-glass reinforcement led to a rapid expansion of FRP boat construction: in the UK, the proportion of boat hulls constructed in FRP was 80 % by the 1970s.

FRP is now employed in a very wide range of boat hulls including sailboards, dinghies, canoes, speedboats, coastal and ocean-going yachts, work-boats, pilot and passenger launches and lifeboats. Its success in this field, where wood is a traditional building material, is attributable to competitive first cost, (particularly in production); trouble-free performance and low maintenance costs and the ease with which complex shapes can be fabricated.

The most common form of construction for shells, decks and bulkheads in large and small FRP hulls is single skin laminate reinforced as necessary by stiffeners. In smaller craft, adequate hull rigidity may be provided by sandwich construction. Sandwich decks, bulkheads and superstructures are commonly combined with single skin shells. New materials and construction techniques are developed and these results in a constant improvement in FRP structures properties[3,4].

Olsson and Lonno[4] suggest that, for high-speed marine vehicles, conventional test methods used for sandwich structures do not account for load cases incorporating

slamming, fatigue, impact or environmental effects. The procedures are inadequate to determine all the relevant material properties required for design purpose. The risk of faulty design is apparent and the potential of composites structures cannot be fully utilised. There is a need for further research on the characterisation of loading of these structures, their structural response, and their fatigue and fracture.

1.2 Shear cracks

1.2.1 Failure modes in sandwich panels

Sandwich beams loaded in bending can fail in several ways. The tension and compression faces may fail uni-axially, by either yielding or fracturing[5,6,7,8]and the compression faces may buckle locally, by either wrinkling or dimpling. Wrinkling involves local buckling of the face into the core, causing compression of the core[9]. Dimpling, which occurs only in honeycomb cores, involves a similar local buckling of the compression face, but in this case, the half-length of the buckling is equal to the cell size of the honeycomb. The core, too, can fail, although this seems to have attracted less attention than face failure. The most common mode of core failure is shear[10]; other possible modes are tensile or compressive yield and, if the core is made of brittle material, tensile fracture. Finally the bond between the face and the core can fail; since the resin adhesives are usually brittle, debonding is by brittle fracture[11]. Similar failure modes occur in end-loaded sandwich columns; face yield has been described by Akers[12], Wittrick[13] and Wrzecioniarz[14], and face wrinkling by Ackers[12], Wittrick[13], Allen[9], Ciba-Geigy[8] and Wrzecioniarz. In addition, columns can fail by overall Euler buckling or by shear buckling.

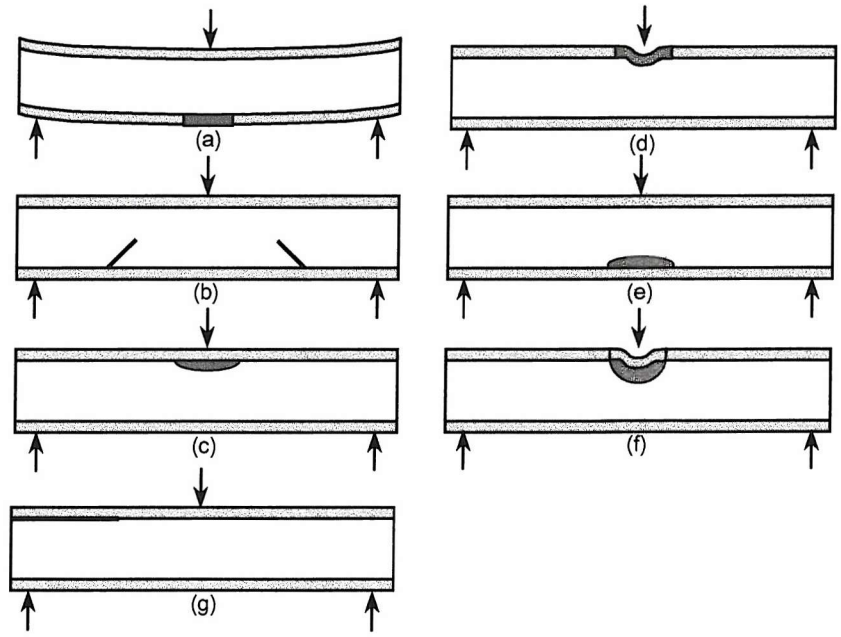

Figure 2: The failure modes in a sandwich beam: (a) face yielding; (b) face wrinkling; (c) core shear; (d) core tensile yield; (e) core compressive yield; (f) core indentation; (g) debonding.

1.2.2 Reported failure in sandwich hull structure

1.2.2.1 Sailing yachts

An inspection of the yachts that completed the last Whitbread Race revealed that few entrants suffered structural damage. Typically, such yachts have sandwich hulls with FRP laminates and foamed/honeycomb polymer cores. The modes of failure were reported as localised core shear failure followed by delamination in the W60 fleet[15,16] and debonding at the outer face-to-core interface in the Maxi fleet. Damage areas were situated around hull bottom forward of the keel. Single-handed Open 60 yachts also encountered delamination problem during the previous Vendee Globe Challenge; both boats, *Fujicolor* and *Sofap Helvim*, suffered delamination in forebody and on large area of topside. Figure 3 shows a close-up view of an area of extensive core shear failure and delamination. The important thing to recognise here is that core shear failure has come first, and the delamination is a secondary effect[17].

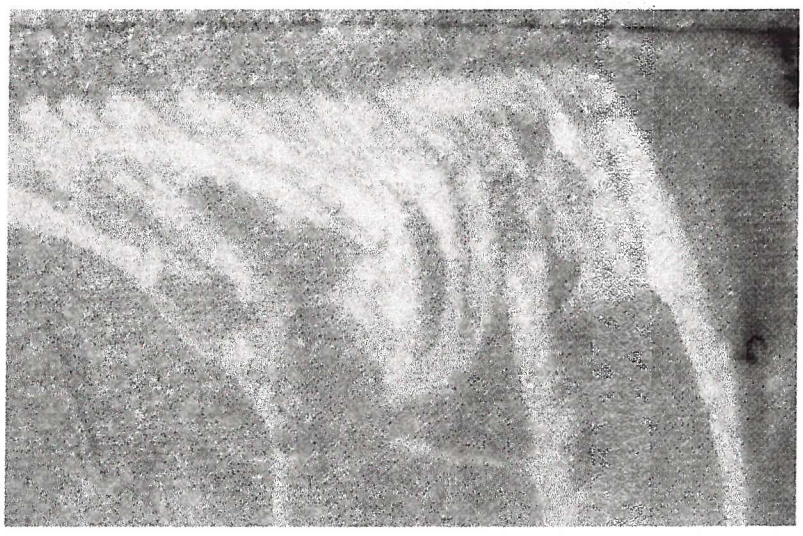

Figure 3: Damage to sandwich bottom panel (500 mm x 350 mm) due to slamming: light areas correspond to face-to-core delamination following shear crack propagation through the core [18]

1.2.2.2 Other high speed light craft - fast ferries and rescue craft

Some rescue craft having sandwich hulls with FRP laminates and foamed polymer cores have experienced damage that is believed to have been caused by (here also) extreme and/or repeated slamming loads exceeding the design load levels. The mode of failure has been predominantly shearing cracking of the core followed by delamination[19,20]. Figure 4 presents a large area of delamination, or more correctly separation of the outer skin from the core, with extensive destruction of the PVC foam core.

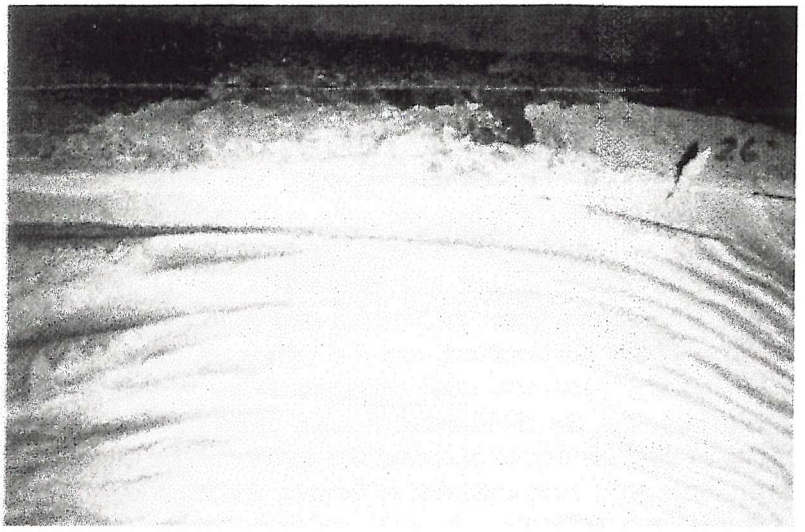

Figure 4: Slamming damage to sandwich hull after removal of outer skin: ripples correspond to the surface fracture within the core [18].

1.3 Crack initiation and growth in cellular foam core sandwich structures

1.3.1 Manufacture and in-service flaws in sandwich structures

Cracks in the core may be present as a result of manufacturing irregularities or in-service damage. Flaws of different kinds may arise during the construction of the sandwich structure, or the production of the core material. The types of flaws considered in this investigation are sub-surface, that are in the core material or in the face-to-core interface, as schematically illustrated in Figure 5a-f.

Unwanted large voids in cellular cores may act as initiation points for crack growth. More severe problem may occur in the manufacturing of sandwich panels. Poor, or even, totally missing adhesive bonding due to errors in the manufacturing will result in debonded areas either between blocks of core materials or in the face-to-core interface. These flaws, shown in the Figure 5a and b, will act as stress concentrators, or even as cracks, or cause premature failure due to face buckling. The frequent use of butt joints and the difficulty in their manufacturing is a major problem. If the filler material does not entirely fill the joint, as illustrated in Figure 5c and d, a part of the structure will be empty of load carrying material and stress concentrators will be created.

There are many types of in-service induced flaws arising from overloading or misuse, such as impact damages, local denting, tensile or compressive failure, and local buckling of the faces. These represent surface failure, which can be detected by a visual inspection. However, damages in the core may not certainly be easily detected. High transverse forces, static or cyclic, result in high core shear stresses and may cause core shear fracture, as illustrated in Figure 5e. Such a fracture will propagate a crack through the core in a 45-degree angle (perpendicular to the maximum tensile stress). A core shear crack will initiate

at the mid-plane of the core, which is the point of maximum stress, or from a material discontinuity, e.g., a void. The crack will eventually meet and follow the face-to-core interface. High shear stresses may also cause fracture in the adhesive joint, which will result in debonding. If the joint is properly manufactured and fulfils the requirement to be stronger than the core, high transverse forces should cause core shear failure before debonding. Debonding may also result from impact, fatigue and thermal loads.

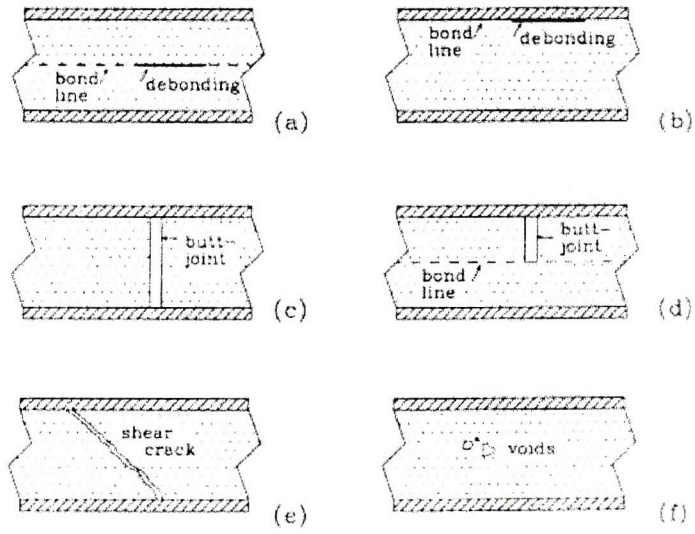

Figure 5: Plausible sub-surface manufacture & in-service induced flaws in foam core sandwich structure[64]

1.3.2 Fracture mechanics & fatigue

1.3.2.1 Fatigue approach to design

There are four different approaches to design against fatigue: oversized-design, fail-safe, safe-life, and damage tolerance.

Damage tolerance uses fracture mechanics and assess whether a crack of a given size can propagate, or alternatively if the structure can maintain its integrity for a given flaw size. Damage tolerance is typically used in the aeronautical industry. Fail-safe is another approach. It consists in designing a components such that, if it fails due to fatigue, the remaining part of the structure is able to maintain its structural integrity until the crack can be detected. Alternatively, components can be designed for a given fatigue life. It will operate over a safe life – beyond which it will be replaced. This approach is typical of aeronautical applications. Finally, structural components can be over-dimensioned and stress levels are kept below the fatigue threshold.

1.3.2.2 Fracture mechanics approach to design

Differences exist between the fracture mechanics approach to design and the traditional approach to structural design and material selection. In the latter case, the anticipated design

stress is compared to the strength properties of candidate materials; a material is assumed to be adequate if its strength is greater than the expected applied stress. Such an approach may attempt to guard against brittle fracture by imposing a safety factor on stress, combined with minimum tensile elongation requirements on the material. The fracture mechanics approach has three important variables, rather than two. The additional structural variable is flaw size and fracture toughness replaces strength as the relevant material property. Fracture mechanics quantifies the critical combinations of these three variables.

1.3.2.3 Fracture mechanics foundations & concepts

Fracture mechanics is a relatively new branch of stress analysis. It evolved from the need for a rational explanation of the several brittle failures-without-warning of ship hull structures, railroads structures etc. The development of fracture mechanics was initiated from several viewpoints. One such viewpoint is the strain energy consideration in a body in which a crack extends by just a small amount. Another approach is the application of linear elasticity for the determination of stress fields at the tip of a crack. Other approaches are equivalent to each other for the elastic behaviour of the material in the close vicinity of the crack tip and diverge for plastic flow. Each approach defines its own version of the resistance of the material to fracture, which may be termed as fracture toughness.

The basic premise in fracture mechanics is the existence of cracks or flaws in all structures. Such flaw can be microscopic in size. For this purpose, local variations in density, micro-voids and orientation can be treated as flaws. These defects are potential sites for the initiation of a crack.

Fracture is the final event, often taking place very rapidly, and resulting in catastrophic failure. Crack growth on the other hand occurs slowly. In PVC cellular material, crack growth takes place by either fatigue due to cyclic loading or creep.

1.4 Purpose of the thesis

The overall purpose of this work is to study the behaviour of material (PVC cellular foam core) and (PVC foam cored sandwich) structural specimens, damaged and undamaged, under a variety of tensile, shear and mixed-mode static and fatigue load cases.

2 CRITICAL REVIEW

2.1 Fracture mechanics of sandwich structures

2.1.1 Fracture mechanics of cellular polymeric foams

2.1.1.1 Properties of cellular foam

Polymeric foams are used as cores for high performance sandwich panels. A comprehensive investigation of the mechanical and physical properties of cellular foams has been published by Gibson and Ashby[21]. However, from a fracture point of view, the behaviour of this core material is relatively not well known.

Rigid foams - like those used in marine application - are linear elastic up to fracture in tension. In compression, stress-strain curves show linear elasticity at low stresses followed by a long collapse plateau, truncated by a regime of densification[22]. Global shear loading is a cross between compressive and tensile loading according to the cell loading. Since the cell edges and walls have less strength in compression than in tension, the first dominant mechanism of failure in shear will be buckling and plastic folding of the cells.

Gibson and Ashby[21] also showed that a few mechanical properties of cellular foams, such as strength and Young's modulus, could be expressed as function of relative density, ρ_{rel}.

2.1.1.2 Macro- microstructure considerations

Inspection of the fracture surface of foam parts leads one to classify the fracture process as "brittle". Macroscopically the fracture surfaces of tensile specimens show some minor irregularities but are nominally flat, and specimens show little evidence of gross yielding or necking[23].

The dimensional frame within which plastic foams might reasonably be assumed to be a continuum is several orders of magnitude larger than most other structural materials. Polymeric foams typically contain large voids and irregularities in structure, which can be easily seen without magnification. The voids in low-density foam account for more than 90% of the volume of the material.

If one places a macroscopic frame of reference, say 10 mm^2, around the crack tip, the discontinuous structure becomes obvious. This fact suggests that any models one might use to represent the crack tip in a foam will not be continuum models but must take the discontinuous nature of the material into account.

2.1.1.3 Fracture behaviour

Ashby *et al.*[24] have treated the fracture behaviour of linear elastic foams. They assume that the crack extends in a discrete way, each step being one cell width. This extension occurs when the stress in the wall of the cell closest to the crack tip is sufficient to cause it to fracture. The problem is solved by considering the equivalent continuum problem and thereby calculating the forces and bending moment on the cell walls. The assumption that the un-notched properties are functions of density yields an expression for the fracture toughness (using a stress intensity factor approach) also a function of density. Folwkes[23] performed fracture toughness tests on PUR foam with specimens of four different geometries from which the critical energy release rate was calculated by the compliance method. Good agreement was found between the different geometries, which tends to verify the validity of the measurements. It was also found that the average cell diameter could be used as an inherent flaw size in LEFM to predict the tensile behaviour of PUR foams. McIntyre and Anderson[25], on the other hand, found the inherent flaw size to be greater than the average cell diameter for PUR foams. Dependence between G_{Ic} and the cell structure was also found. Zenkert[26] investigated the mode-I crack propagation of PVC cellular foam, see Figure 8. He found that the mode-I fracture toughness was approximately linearly increasing with increasing average cell size, and that apparent mode-II fracture toughness was slightly higher than the mode-I . He suggested that LEFM was applicable to this material.

2.1.1.4 Mixed-mode fracture criteria in homogeneous materials

Zenkert performed mode-II and mixed-mode fracture tests on the same material[27]and found that both fracture stress and propagation angle could be accurately predicted with the strain energy density criterion for the mixed-mode case, originally proposed by Sih[28,29]. A maximum tangential (or hoop) stress criterion - based on Williams's investigation[30] proved also to make good predictions. Grenestedt *et al.*[31] investigated further fracture criteria for wedges. Grenestedt also used successfully Severyn's criterion based on opening stress and un-notched strength of the material for mode-I and mode-II fracture prediction.

2.1.2 Debonding and interfacial crack

Carlsson[32,33,34] investigated the interface crack characterisation in beams using various specimens. Axial and transverse peel forces were main loading parameters. He found that stress intensity factors are larger at the face/adhesive interface than at the core/adhesive interface. The type of adhesive strongly influences the bond fracture resistance but not the behaviour of the fracture angle. The orientation of the laminate also affects greatly the fracture behaviour at the interface. Ductility of the core material promotes interfacial

debonding rather than crack kinking. Mode-I favours crack propagation, whereas mode-II favours crack deflection. In general axial compression loading of the faces produces a state of crack loading, which is highly sensitive to the structural details of the sandwich. Zenkert[35] looked at the interface problem on beams and panels and concluded that interface debonding has a drastic influence on the load bearing capacity of the damaged structure. He also found that mode-II is the dominant loading mode at the crack tip but mode-I is always present.

2.2 Long term fatigue behaviour of sandwich structures

2.2.1 Fatigue damage modeling

2.2.1.1 Representation of data

The traditional curve of applied mean stress level against the number of cycles to failure (S-N curve) forms the oldest and most voluminous form of fatigue data presentation. However, its usefulness is limited because a separate curve for every material, condition, shape, size must be obtained[36]. Attempts to plot S-logN often showed that the function was not only linear but also non-exponential and that the hope for constant exponent in the damage law equation was not really a material constant after all. The number of cycles to failure depends on the stress range and mean stress. Gerber proposed a parabolic relation whereby the endurance limit and/or curves of constant life can be plotted. Goodman diagrams, with linear relationships, are useful means of presenting fatigue data, but in general form the upper and lower range limits for finite life. The need to include the stress ratio R as well as mean stress resulted in the evolution of the Constant Life diagram. These plots indicate the behaviour in terms of constant lifelines for all conditions that are possible to apply. The information is constrained entirely within the Goodman line triangles; regions outside the static boundaries represents stresses greater than the ultimate strengths. The diagrams may be regarded as a collection of S-N curves, each at the appropriate mean stress and stress ratio.

2.2.1.2 Modelling

The most widespread technique for the life prediction of metallic components is linear elastic fracture mechanics, which is based on the growth of single flaws to failure. In composite materials, fatigue is associated with the growth of multiple micro-cracks in the matrix and therefore the applicability of such a technique is severely limited[37,38]. Current techniques that have been developed are based on the phenomenological approach, which is concerned with lifetime predictions without enquiring into the microstructural nature of

fatigue failure within the composite[38]. This approach falls into two categories: namely empirical models and wear-out models.

Empirical models are often statistically based, thus requiring large amounts of data such as static strength, fatigue life and residual stress distributions in order to predict residual strength at any number of cycles. Wear out models are all physically based, relating to the reduction of some physical property such as stiffness or strength, and the ability to predict its decay during fatigue loading. However, a problem arises since the chosen wear out parameter is inevitably dependent on stress. Therefore testing at various stress levels must be undertaken to describe its behaviour.

Many phenomenological approaches have been proposed, each with its own failure criterion depending on the degradation variable used. One approach is to measure residual strength with load cycling. Then an S-N curve can be drawn through the focus of data points where the residual strength equals the applied stress. If the application is critical, a Weibull distribution could be used to describe the variations in strengths and probability curves can be drawn through the vast collection of data. Many approaches assume that failure will occur when some critical level of damage in the composite is exceeded. Damage grows with cycling and its growth depends on the cyclic stress range, the load ratio and the current value of damage provided other variables such as temperature and frequency do not change. It follows that the fatigue lifetime is simply the number of load cycles it takes to raise an initial damage state (usually equal to zero) to the final or critical level of damage. The problem is the damage function is not known but this can be associated with the reduction of some property such as stiffness, which can be gathered experimentally. Testing procedures and standards for static and fatigue testing are outlined in reference[39].

2.2.2 Fatigue of cellular polymeric foam core materials

In sandwich structures under cyclic load, failure of the core is usually associated with core shear. Methods of testing are given in ASTM Standards for Composite Materials[40]. Loading is in shear parallel to the plane of the facings. From a complete load deformation curve, it is possible to compute an effective shear modulus. However there is a dependence of the results on the test method used, and no core shear values should be incorporated into design calculations without a full knowledge of the testing procedure and laboratory conditions[39].

2.2.2.1 Flexural fatigue of foam-cored sandwich beams

Developments in Scandinavia have concluded that at high strain rates the core materials become more brittle and hence the ultimate stress and modulus increase while the strain at ultimate stress decreases with increasing strain rate[41]. During cyclic loading, this may mean the material is less damage tolerant and more susceptible to crack propagation[42,43]. Buene

and Hayman give two core failure modes, which are common in flexural fatigue. The mode-I failure that is characterised by a single shear crack. The failure mode is more typical of brittle cross-linked foams. In mode-II, the final shear failure is associated with cracks in a progressively damaged horizontal region in the core, and indicates weakening of the core by progressive damage subsequent to yielding. This is more typical of linear foams, but has been observed in cross-linked PVC material. It was also found that the variation of stiffness during lifetime was very small and that the time from visual crack formation and crack propagation to final fracture was relatively short relative to the total fatigue life. The cross-head displacement was used to evaluate the load-deflection relationship over the fatigue life. The deflection history was assumed to be representative of the core shear deformation variation; no strain measurements were made on the core material itself. This is in agreement with Echtermeyer[44] and Shenoi[45]. Shenoi reported residual plastic distortion for linear variety of PVC foams after fatiguing. Marginal reduction in strength and stiffness were also reported for pre-fatigued specimens.

Burman[46,47] investigated the fatigue crack initiation and propagation in foam-cored sandwich structures using a modified 4-point-bending (4PTB) rig. He studied the damage formation process and crack propagation angle. The fatigue damage initiated in the middle part of the core forming microcracks and eventually grew together and formed an horizontal macro crack located between the load application point and the support. He also investigated the R-dependency of shear load in undamaged beams. For $R>0$, the crack propagated and kinked away towards the interfaces in the direction corresponding to the maximum tangential stress.

2.2.2.2 Fatigue crack growth

A few investigations have been carried out on the fatigue behaviour of polymeric cellular foam materials. Noble and Lilley[48] investigated the fatigue crack propagation in polyurethane cellular foams subjected to mode-I loading using a compact-tension (CT) specimen. Fatigue crack growth rate da/dN and cyclic stress intensity factor range ΔK were successfully correlated using the Paris law. The fatigue crack growth rate was also found to be dependent on the mean stress level. Yau and Mayer[49] investigated the influence of environmental conditions on fatigue crack growth rates in polycarbonate foams.

Fatigue and fracture process of polymeric foam was studied by Fleck and Parker[50]. They proposed that crack extended by one cell diameter through cell wall after repeated flexion of the cell wall in front of the crack tip.

2.2.2.3 Frequency effects

Cellular polymeric foam is viscoelastic in nature. For foam core sandwich structures under static loading conditions, increasing the strain rate results in the core getting stronger and stiffer[41]. Under cyclic loading conditions, repeated large strain variation results in temperature rises in the core even at reasonably small strain rate. Olsson[51] and Hedlund [52] showed that small increase in temperature in the core reduces fatigue life.

2.2.3 Fatigue of sandwich FRP faces and interface

2.2.3.1 Fatigue of laminates

There are 3 basic failure mechanisms in composite materials associated with fatigue: matrix cracking, interfacial debonding, fibre breakage[53].

2.2.3.1.1 Unidirectional Composites

Damage mechanisms of unidirectional fibre composites in tensile fatigue have been extensively investigated[54]. For unidirectional composites the fibres carry virtually all the load but the experimental evidence suggests fatigue performance is determined principally by the strain in the matrix[37,55]. All non-metallic fibres have a statistical distribution of strength, determined by flaws; thus, a few of the weakest fibres will fail during fatigue loading. Locally high stresses in the matrix and at the fibre/matrix interface lead to the development of fatigue damage. Damage may also develop at local micro defects, such as misaligned fibres, resin rich areas or voids. These can lead to resin cracks developing between fibres, isolating them from adjacent material, rendering them as ineffective load carriers causing fibres to become locally overloaded, resulting in further fibre static failure. Close to failure, the matrix may show extensive longitudinal splitting parallel to fibres caused by resin and interfacial damage, leading to the brush like failure characteristic of most unidirectional materials[37].

Unidirectional composites characteristically show excellent fatigue resistance[55]. However, since fatigue performance is linked mainly to strain in the matrix, the use of stiffer fibres will only show a slight increase in fatigue performance compared to using a modified fatigue resistant resin. The slope of the S-N curve is related directly to the strain in the matrix[37]. Glass fibres with failures strains of 2.5 to 3.5% lead to greater matrix strains when compared to carbon fibres with failures strains of 0.6 to 1.8 %. Therefore, the slope of the S-N curve for the former case is greater. With Aramid fibres fatigue damage mechanism is more complicated since the Aramid fibre are themselves fatigue sensitive and can defibrillate during fatigue loading. This causes the S-N curve to adopt a flat shape, which becomes much steeper at an intermediate number of cycles. Talreja[54] suggests that the shape

of the strain life diagram depends on the relation between the static failure strain of the composite and the fatigue life of the matrix. According to this view, if the matrix fatigue limit is greater than the static failure strain of the composite, broken fibres occur at random during cycling and the life dependence is statistically determinated. If on the other hand, the matrix fatigue limit is less the static failure strain of the composite, progressive fibre fracture can occur and then a slopping curve results which is stress and cycle dependent.

2.2.3.1.2 Laminates

Composites materials are usually formed with a combination of several laminae in various directions, with a stacking sequence based upon design load requirements. Matrix cracking in off-axis plies is usually the first significant damage and grows during fatigue cycling across the laminate[55,56]. Transverse cracks couple together by interface debonding enhanced by tensile stresses; this mechanism leads to transverse cracks in one lamina spreading into neighbouring laminae. Longitudinal cracking caused by stacking sequence related edge stresses may also assist in crack coupling. An intense damage region then forms where delamination growth is driven by interlaminar stresses and some fibre fracture takes place in the 0° plies eventually causing specimen rupture. However, the ultimate tensile fatigue failure of composites is still usually determined by the unidirectional layers. Thus, the tensile S-N curves for multi-directional laminated composites are still relatively shallow, although steeper than for fully uni-directional composites[54].

2.2.3.2 Frequency effects

It has now long been recognised that FRP laminates (polymer matrix composites and fibres) are viscoleastic materials. Strength and stiffness of these materials may vary according to temperature and strain rate. Under cyclic loads, hysteresis-heating effects may therefore occur, but also increase noticeably for increasing frequency. This heating effect is particularly apparent in resin-rich laminates[37]. Further, in most FRP, the effects of an increasing strain rate will result in an apparent higher strength and a lower strain to failure. Thus, when collecting data for fatigue tests, it is desirable to carry out static tests at the same strain rate as fatigue tests.

2.2.3.3 *Edge effects*

Edge induced stresses are especially a problem in fatigue and testing policy is usually aimed at minimising edge effects and the damage that inevitably results. Both shear and normal stresses can develop at coupon edges; these arise from a mismatch of properties between the layers[37]. The magnitude of the stresses changes both with temperature (as layers have different expansion coefficients) and with moisture content (as layers expend to different

extents on absorbing external moisture). Thus, layer-staking sequence is a critical variable. In general, laminates with evenly distributed layers lead to the lowest edge effects for both tensile and compressive externally applied loads.

2.2.3.4 Fatigue of the interface

Composite materials owe their very existence to adhesion between resin matrix and reinforcement and additionally with core materials. This requires a tough adhesive, which is compatible with the skin and the core material. Consideration needs to be given to the stress regime, joint geometry and fabrication methods proposed. Additionally, the mechanical, thermal, creep and durability properties of the adhesive must be considered before selection.

In general, toughened adhesives in the top of the acrylic stiffness range and the spectrum of cold/warm cure two part epoxies are all true structural adhesives for FRP applications. The fatigue characteristics of the interface of sandwich structures are generally excellent if loading is moderate. Peak stress levels should be specified within the elastic range of the adhesive at all times. It follows that cyclic loads should be maintained significantly lower than the limit loads indicated by static results. However, debonding of the skin from the core can take place especially during high rate dynamic loading like slamming, impact, and explosive shocks as often encountered by coastal waters in the marine environment[41]. Several debonding failures have been encountered by coastal rescue vessels in Norway[42] where there was an under estimation of loads experienced in the design and approval for the vessel. Some core adhesives are considerably stiffer than the other core materials they are expected to join. Thus when loaded, they develop appreciably higher stresses than the surrounding foam core. With repetitive slamming loads, the low ductility adhesive cracks at an early stage and the foam core takes on a more brittle, less damage tolerant behaviour. The crack in the adhesive can initiate cracking in the core. Thus, it is important to match the properties of adhesive and core as closely as possible and to ensure the combination is damage tolerant.

Burman[47] recently investigated the fatigue performance of damaged sandwich beams subjected to fatigue loading; two types of sub-surface flaws were investigated: a face/core interface disbond and a flawed butt-joint. It was found that the change of compliance was not a good way to determine the crack initiation. R-dependency was found to be less significant for damaged specimens.

2.3 *Theoretical modelling*

2.3.1 Analytical closed form methods

2.3.1.1 Sandwich structures

For static analysis of sandwich beams, classical beam theory is a well-known method for calculating section properties such as flexural stiffness and is covered by numerous sources[57,58,59,60,61,62,63,64,65,66,67]. Allen suggests that sandwich beams and panels can be classified into three regimes: composite beam behaviour where core shear strains are small; thin-face sandwich behaviour where core shear strains lead to significant additional deflections; thick-face sandwich behaviour where the load is split into two parts, one resisted by a beam analogous to a thin-face sandwich beam, and the other by a local bending action of the faces themselves.

However, the most common case is thin-face sandwich behaviour. A realistic assumption is that the core does not contribute to the bending stiffness of the sandwich, so that the shear stress is approximately uniform throughout the depth of the core. Bending/shear deflections and stresses are therefore easily calculated for different boundary conditions and loading cases. For simply supported beams, the shear deflection occurs quite independently of the bending deflection and has no major effect on the stresses in the face.

For plate panels, Allen, Pagano[68], Mace[69] and others present linear theories of composite plates (monolithic or sandwich) in the three regimes.

In practice for marine applications, the faces are not always of equal thickness because FRP is weaker in compression than in tension. The bottom exterior face is therefore thicker, partly as it is in compression and partly as it is more likely to be over-engineered as it is the first line of defence against water penetration. Classical beam theory can still accommodate this if the actual position of the neutral axis is found.

Theulen and Peijs[70] give an optimisation of bending stiffness and strength as design parameters. This can be extended to plate theory in 3-D for various loading conditions assuming isotropic or orthotropic material properties.

2.3.1.2 Fracture mechanics

The first systematic investigation of fracture phenomena was carried out by Griffith[71] nearly seventy years ago. He postulated the existence of flaws, and that the crack growth was controlled by the balance between the available strain energy and the energy required to form new crack surfaces. The subject was further developed by Sneddon[72] by investigating the behaviour of a simple penny-shaped crack. Another important contribution by Irwin was that he demonstrated the universality of the crack-tip stress field and introduced the stress

intensity (K) approach. Theoretical fracture mechanics is based on the basic principles of solid mechanics and can be formulated in terms of energy or stress field for 2D or 3D problems. Analytical solutions of the elasticity equations of crack problems in linear elastic fracture mechanics are usually limited to highly idealised problems which do not adequately model real engineering structures. However, it is often possible to incorporate part of the idealised solutions into real problems, leading to semi-empirical approaches. In limited cases, it is possible to obtain a closed-form analytical solution for the stresses and strains and therefore the stresses in the body must be estimated numerically.

2.3.2 Numerical solution techniques

2.3.2.1 Fundamentals

The most common form of numerical analysis is finite element analysis (FEA) and there are numerous references[73,74,75,76] covering the basic principles. In this context, the finite element method (FEM) uses basic principles of elasticity on a mesh of identical representative elements substituted for the actual structure. The most common form of FEM is the displacement-based method. The steps in the typical solution for a linear elastic structural problem is as follows[77]: idealisation of the structural problem, subdivision of the continuum in finite elements, modelling of the displacement field for each finite element, generation of the stiffness matrices and the nodal equivalent loads for each element, assembling the element stiffness matrices into a global stiffness matrix, taking into account the connection between the elements, specifying the displacement boundary conditions, solution of all equilibrium equations to obtain all element nodal point displacements, evaluation of the element stresses by equations relating displacements to strains and stresses.

Commercially available FE codes such as ANSYS (used in this investigation), NASTRAN, ABAQUS, NISA, I-DEAS and so on, can deal with very complex situations.

The key to a successful use of FEM is an accurate approximation of the theoretical exact solution. This implies the control of the modelling errors, discretisation errors and computing errors. In that respect, sandwich structures must be given special considerations. The inhomogeneous and often anisotropic build-up of the sandwich should be carefully thought about.

The shear deformation in the core must be considered in most cases. The anisotropic nature of the composite face materials must be accounted for. Due to low stiffness and strength in the thickness direction of the sandwich, local load introductions, corners and joints have to be checked by 2D or 3D analyses to a larger extent than cases for metal structures. For the same reason, curved panels with small radii of curvature (less than ten times the sandwich thickness) will have to be analysed in 2D or 3D to account for the

transverse normal stresses not included in shell elements. Boundary conditions for sandwich plates may be different from ordinary structures. For example, a simple support could be *soft* - bending moment at support point is zero and shear strain varies linearly across the thickness of the beam. Or on the contrary, it could be *hard* - the opposite case, where the shear strain is nil and a bending moment prevents rotations while allowing for displacements in the normal directions

2.3.2.2 Numerical fracture mechanics

A variety of numerical techniques have been applied to problems in sold mechanics, including finite difference, finite element and boundary integral equation methods. In recent years, the latter two numerical methods have been applied almost exclusively. The vast majority of analyses of cracked bodies utilise finite elements. Although the boundary integral method may be useful in limited circumstances - when the boundary quantities are of primary interest.

The approaches outlined below can be divided into two categories: point matching and energy methods. The former technique entails inferring the stress intensity factor from the stress or displacement fields in the body, while energy methods compute the energy release rate in the body and relate G to stress intensity. One advantage of energy methods is that they can be applied to non-linear material behaviour; a disadvantage is that it is often difficult to separate energy release rate into the different mode-I and mode-II K components.

Most of the techniques listed below can be implemented with either finite element or boundary element methods: stress and displacement matching, element crack advance, contour integration, virtual crack extension - stiffness derivative formulation, virtual crack extension - continuum approach.

Shih *et al.*[78] have recently formulated the energy domain integral methodology, which is a general framework for numerical analysis of the J integral. This approach is extremely flexible. It can be applied to both quasi-static and dynamic problems with elastic, plastic, or viscoelastic material response, as well as thermal loading. Moreover, the domain integral formulation is relatively simple to implement numerically, and it is very efficient. This approach is very similar to the virtual crack extension method.

Zenkert[26,27,64,79,80] has treated the numerical modelling of damaged PVC foam core sandwich beams and panels. Models ranges from specimens with horizontal cracks embedded at the mid-plane, specimens with shear cracks embedded in the core, and specimens with interfacial (face/core) cracks. In particular, Zenkert modelled a 4PTB damaged beam with a shear crack embedded in the core; fracture parameters and fracture

loads were computed and compared with experimental fracture loads. The methods of calculation used were the displacement extrapolation method or the J-integral method (non-linear analysis). Typically, 8-node quadratic plane strain elements were used. Carlsson[32,33,34] investigated the interface crack characterisation in beams using models based on different specimens, such as CSB and DCB. The adhesive layer was modelled. Parametric study took into account material and geometry. Falk[81] modelled successfully a simply supported sandwich plate with interface debonding. He conducted a sensitivity study on material and geometry variables. Conclusions showed that fracture parameters followed identical trends as for beam structures. However, Zenkert showed that, for interfacial debond, the ratio mode-I/mode-II is slightly higher for panels (5-15%).

2.4 Analysis of the current status

2.4.1 State-of-the-art

A large amount of work has been carried out on the study of static failure limit of foam core sandwich constructions.

A few investigations have focused on damaged sandwich structures. Previous works include calculations of foam core fracture parameters and characterisations of fracture for shear cracks and interfacial (face/core) cracks. They are, however, limited to pure mode-I or mode-II.

Even fewer studies have been carried out on fatigue crack growth of rigid cellular foam materials; they are also limited to tensile load cases.

A fair amount of work has also been done on the fatigue response of foam core sandwich structures. Up to now, previous works have focused on fatigue life (S/N diagram), fatigue failure mode of the structural component, and little on the damage characterisation of the core.

The mechanical and physical properties of foams have been thoroughly studied. Basic models have been proposed for the fracture mechanisms of cell structures and for the fatigue mechanism of crack propagation and fracture process in cells.

2.4.2 Themes for investigations

There is an obvious difference between the current knowledge on failure mechanism and fatigue response of sandwich structures compared to that of rigid cellular foam materials. Thus there is a need for a better characterisation of the rigid cellular foam materials.
The research work presented in this thesis intends to:

- broaden the understanding of fracture of sharp cracks and fatigue crack growth;

- characterise the material for variety of loading conditions ranging from mode-I, mixed-mode and mode-II;
- correlate experimental investigation and theoretical modelling, either by analytical fracture criterion performance evaluation or numerical modelling;
- establish a correlation between the behaviour of sandwich structure and the rigid cellular material.

3 INVESTIGATION PHILOSOPHY

3.1 Introduction

A large variety of research work has been carried out on the study of sandwich constructions and foam materials. In the sandwich context, crack initiation and propagation though is most important.

Currently, from a material characterisation point of view, the current knowledge of the fatigue and fracture behaviour of foams used in sandwich context is limited. There is thus a need to gain further understanding of the crack initiation and propagation in these materials at both macro and microstructural level.

The ultimate aim of the research work presented in the thesis is to broaden the current understanding of the fatigue and fracture behaviour of foam-cored sandwich structural specimens under a variety of tensile, shear and mixed-mode static and cyclic fatigue load cases.

3.2 Scope

The focus of the thesis is on PVC cellular rigid foam materials used as a structural core component in fibre-reinforced-plastic sandwich structures. The variety of foam is cross-linked (manufactured by AIREX), exhibiting brittle behaviour. Characteristics of the materials and sandwich structures specifications are representative of constructions in the marine industry for high speed light craft. The specimen dimensions are governed by practical and testing constraints. The sandwich structures have thin and stiff faces, and relatively thick and compliant core. Load cases used on the test specimen in the experimental investigations corresponds to a variety of tensile, shear and mixed-mode load; no compressive or buckling loads are used. The load regimes are static and constant cyclic fatigue loading. Only sharp cracks are used as initial flaw in damaged test specimens. All the experimental investigations are carried out at room temperature, normal humidity and atmospheric pressure conditions; the effects of environmental conditions are not in the scope of the thesis. The stress field near the crack tip is assumed to be solely determined by the linear elastic singular solution. On the basis that the foam is brittle and using LEFM makes the problem analysable.

3.3 Means

The aim of this thesis can be achieved by mastering the fields of composite structures, sandwich structures, cellular core materials, fracture mechanics and fatigue of materials.

It is also necessary to be proficient with the investigation methods, i.e. general finite element modelling, finite element modelling of composites and sandwich structures, finite elements modelling of cracked structures, experimental techniques for sandwich structures, experimental techniques for fatigue and fracture of materials.

3.4 Specific objectives

3.4.1 Mode-I, mixed-mode, mode-II fracture in PVC foam

Chapter 4 seeks to extend the understanding of the fracture behaviour of foams through testing and numerical studies.

The main objective of the experiment was to accurately determine the fracture toughness K_{IC} and K_{IIC} for a range of densities. The two other goals were to study the relationship between the stress intensity factors at fracture under mixed-mode conditions and the fracture toughnesses K_{IC} and K_{IIC} in order to establish the fracture behaviour and assess diverse mixed-mode criteria.

3.4.2 Crack growth in rigid cellular foam under a variety of cyclic loading

The aim of this Chapter 5 is to broaden the knowledge of the fatigue crack growth behaviour when subjected to mode-I, mixed-mode and mode-II cyclic loading.

The first specific objective is to determine the crack growth rate under various loading conditions. Another goal is to study the relationship between the stress intensity factors and crack growth rates. The two other goals are to study the fatigue and fracture behaviour at both micro- and macroscopic level and assess diverse mixed-mode criteria.

3.4.3 Flexural fatigue and fracture in foam cored sandwich beams

The main purpose of the Chapter 6 is to extend the understanding of the flexural fatigue in FRP sandwich foam core beams.

The specific objectives of the investigation are to determine the constitutive phenomena governing the flexural fatigue behaviour of cross-linked PVC foam-cored sandwich structures; to determine crack growth rates and crack propagation angles; and to propose a model for fatigue crack initiation and propagation in the damage process area for the material under consideration at both macro and microscopic scale.

3.4.4 Numerical analysis of shear crack in foam core sandwich beams

The investigation presented Chapter 7 seeks to extend the understanding of the fracture behaviour and to map the fracture parameters for shear cracks in foam core sandwich beams through numerical studies of the 4PTB specimen.

The main objectives of the study are to determine strain energy release rate G and stress intensity factors K_I and K_{II} for a range of physical and mechanical properties that are characteristic of a typical sandwich beam. The second goal is to study the relationship between the stress intensity factors. A practical objective is to predict the failure load of a cracked sandwich beam by correlating results from experimentally-determined fracture envelope and stress intensity factors calculated numerically. A final objective is to establish a correlation between stress intensity factors calculated numerically and fracture toughnesses under mixed-mode conditions derived from experiments.

4 MODE-I, MIXED-MODE, MODE-II FRACTURE IN PVC FOAM

4.1 Purpose and objectives

This chapter seeks to extend the understanding of the fracture behaviour of foams through testing and numerical studies.

The main objective of the experiment is to accurately determine the critical fracture toughnesses K_{IC} and K_{IIC} for a range of densities. The two other goals have been to study the relationship between the toughness values under mixed-mode loading and the critical fracture toughnesses K_{IC} and K_{IIC} in order to establish the fracture behaviour, and to assess diverse mixed-mode criteria.

4.2 Test method and set up

4.2.1 Materials

The material used in this investigation is PVC cross-linked cellular foam made by AIREX. It is made of closed cells and typically exhibits low fracture toughness and brittle fracture behaviour. Three different densities were used; with nominal values of 90, 130 and 200 kg/m^3, referred as C70.90, C70.130 or C70.200. A characteristic tensile stress-strain relation is shown in Figure 6.

Typical properties of the foam materials in tension and shear are summarised in Table 1[82].

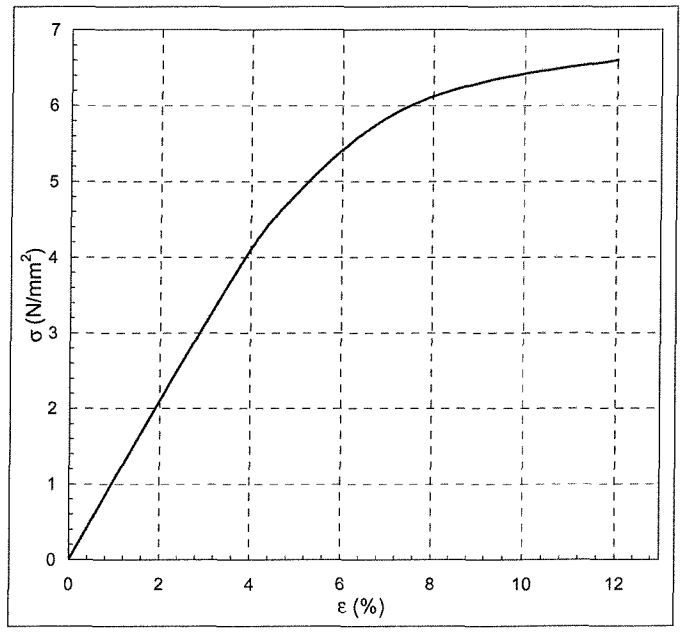

Figure 6: Tensile stress-strain relation of C70.200

Table 1: Properties of C70 AIREX foam in tension and shear

Name	ρ	E_{tens}	$\sigma_{ult.}$	σ_{limit}	σ_{yield}	G	$\tau_{ult.}$
	(kg/m^3)	(MPa)	(MPa)	($N.mm^{-2}$)	($N.mm^{-2}$)	(MPa)	(MPa)
C70.90	90	81	2.6	1.65	2.1	38	1.6
C70.130	130	109	3.7	1.75	2.4	50	2.2
C70.200	200	178	6.6	3.00	4.3	81	3.5

Note that here $\sigma_y = \sigma$ at 0.2% offset ε

The test specimens were cut from blocks in both the longitudinal and transverse direction to the dimensions of 60 x 40 x 10 mm. The dimensions of the CTS specimen used are shown in Figure 7. Three holes were drilled along the top and bottom edges of the specimen. Sharp crack-shaped notches were made with a thin band saw of 0.8-1 mm thickness with a/w = 0.4. The tip part of the crack was made with a razor blade up to a/w = 0.5, or 0.55 for the testing of the C70.90 and C70.130 foam specimens in pure mode-II, see Figure 8. For the C70.90 specimens thin wooden battens were used to spread the load on the specimen faces in order to overcome local foam crushing at pinholes.

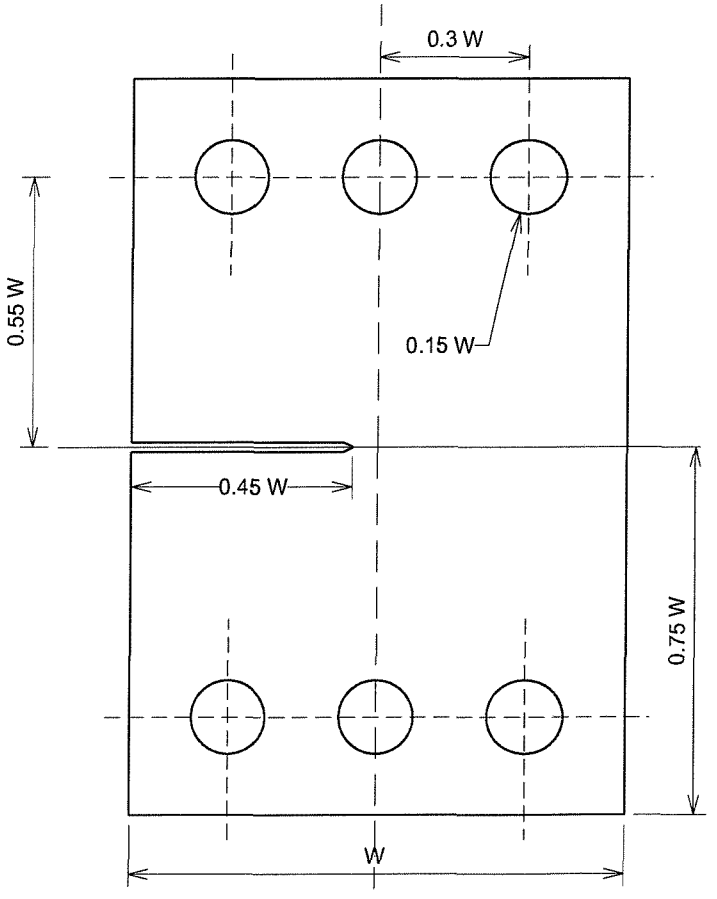

Figure 7: Static CTS fracture specimen geometry

W = 40 mm, thickness = 10 mm

4.2.2 Test rig and set up

A simple and compact fracture mechanics specimen was used for the determination of fracture toughness under mode-I, mode-II and mixed-mode loading conditions. The loading

device is simply installed in the universal testing machine, and generates accurately repeatable multi-axial loading conditions, see Figure 9.

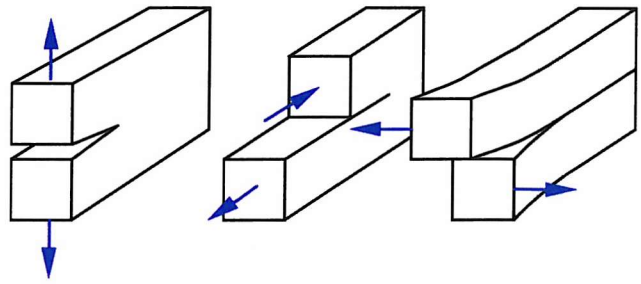

Figure 8: Mode-I (tension), mode-II (shearing) and mode-III loading (tearing)

The tests were displacement-controlled; this was because load-controlled testing was difficult to achieve with the small loads that had to be applied on the specimen. All specimens were tested at the same displacement rate of 1 mm/minute. Load and displacements were recorded with the built-in load cell during the whole test. All tests were carried out using an Instron model 8500 universal-testing machine. Crack mouth displacement was measured with a 5-10 mm gauge extensometer previously calibrated for linearity according to *ASTM Standard E 399* [83]. A total of 72 specimens were tested in this survey. For each of the 3 densities, one mode-I, one mode-II and two mixed-mode loading conditions, were used as shown in Table 2. Mode-I, mode-II or mixed-mode loading conditions were produced by selecting the fastening position of the jig to the machines arms, see Figure 10. Tests were repeated 3 times for both longitudinal (crack in the x-direction of the original block) and transverse (y-direction) specimens.

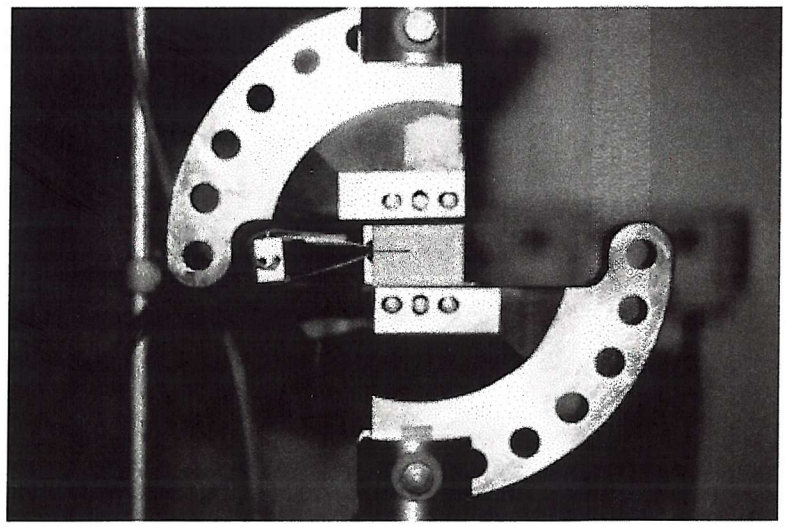

Figure 9: Loading device for mixed-mode loading and specimen

Table 2: Mode-mixity vs. loading angle α

Mode-mixity	pure mode-I	mixed-mode	mixed-mode	pure mode-II
α	0°	30°	60°	90°

4.2.3 Test method

Using a load-displacement curve, the *ASTM Standard E 399* [83] defines an apparent crack initiation load, P_Q, using a 5% secant construction. The standard states that the load must be greater than 1.1 times the maximum load in the test for the result to be valid. The provisional fracture toughness, K_Q, is then calculated from the following relationship:

$$K_Q = \frac{P_Q \sqrt{\pi a}}{wt} f\left(a/w\right) \qquad (1)$$

K_Q value computed from (1) is a valid K_I or K_{II} result only if all the validity requirements were met, see (3-4). K_I and K_{II} are obtained using geometrical factors f(a/w), i.e. f_I or f_{II} respectively in (1) In turn, f_I or f_{II}, are obtained from a finite element model of the CTS test specimen.

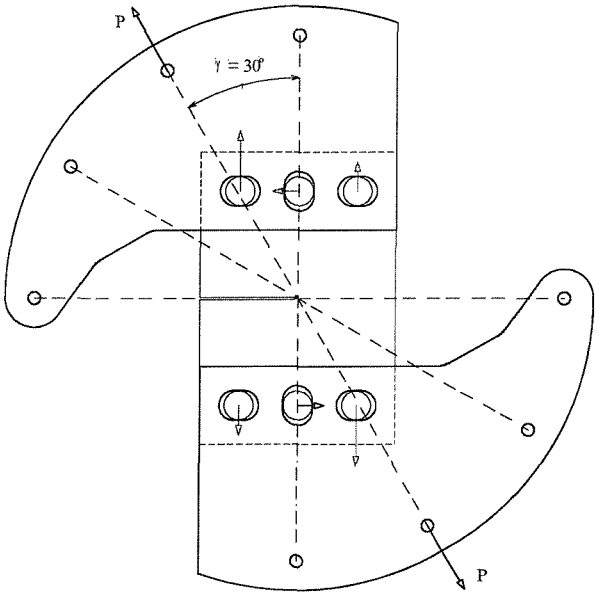

Figure 10: Loading device for mixed mode loading and specimen

4.2.4 Assumptions

ASTM Standards E 399 [83] and *D 5045* [84]give some guidance for plane strain mode-I fracture toughness K_{IC} for metals and plastics, and draft provisions on the specimen sizes. The scalars in (3) and (4), defining the size requirements, are used in both K_{IC} standard for metals [83] and K_{IC} standard polymers [84]. Further, no standard requirements exist for the validity of LEFM and plane-strain conditions for tests with cellular materials. Because the yielding behaviour of metal and plastic are different, and because bulk material and cellular material are also different at microscopic scale, one should not expect both material systems to exhibit the same size limits for a valid K_{IC}.

LEFM is the primary requirement, i.e. linear elastic material behaviour of the cracked specimen, so certain restrictions on linearity of the load displacement diagram are imposed.

A state of plane strain at the crack tip is required. Specimen thickness must be sufficient to ensure this strain state. The crack must be sufficiently sharp to ensure that a minimum value of toughness is obtained. The failure must be a brittle fracture. Imposed ASTM requirements for K_Q to be valid are the following:

$$0.45 < a/w < 0.55 \tag{2}$$

$$t, a, w-a < 2.5 \cdot \left(\frac{K_Q}{\sigma_y}\right)^2 \tag{3}$$

$$P_{max} \leq 1.1 P_Q \tag{4}$$

No standards exist for mode-II fracture toughness and mixed-mode fracture.

4.3 Experimental results

All the tests showed clear linear elastic and brittle material behaviour and an almost straight P-δ curve. Specimens failed at relatively low values of strain with only little elongation after the proportional limit, see Figure 11. Moduli of elasticity of identical specimens were sometimes different and led to some scatter in the K_I and K_{II} values.

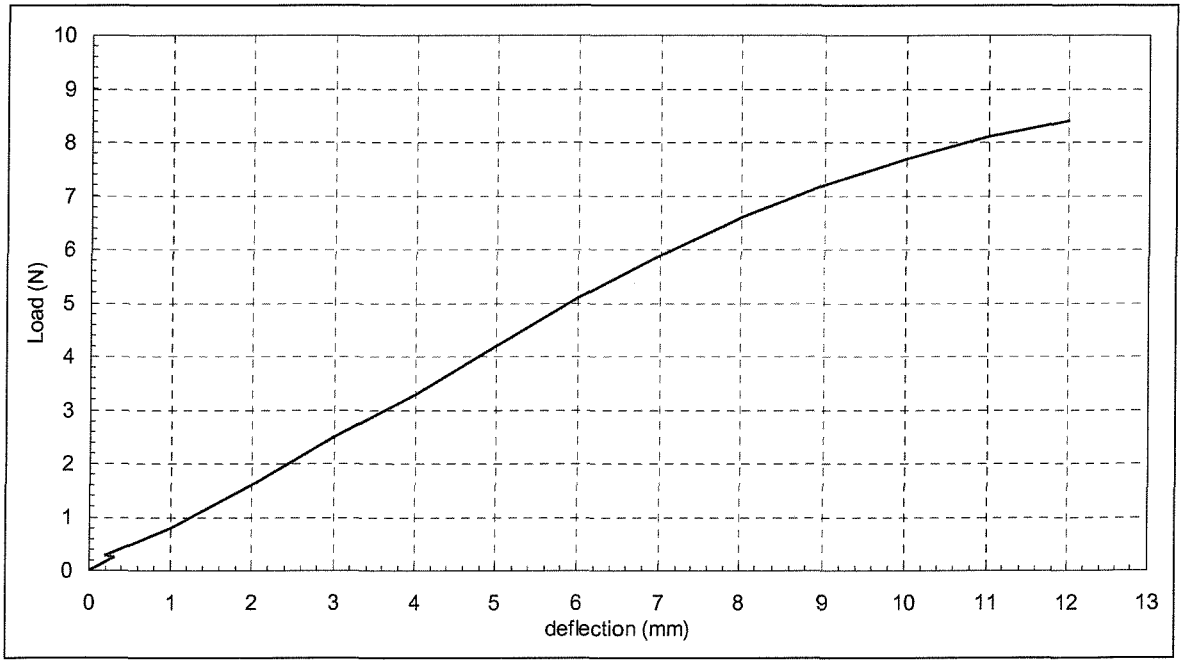

Figure 11: P-δ curve of C70.130

4.3.1 Fracture toughness K_{IC} and K_{IIC}

Fracture toughness values were derived from the load-displacement curves. K_{IC} and K_{IIC} were calculated using the relationship of (1). Table 3 shows the mean values of experimentally determined fracture toughness in mode-I and II. Results are shown for the three densities under consideration and for both in-plane directions, i.e. x-direction and y-direction, of the material. K_{IC} and K_{IIC} decrease with decreasing nominal density. Fracture

toughness in the two in-plane directions is slightly different. This is in accordance with other material properties, e.g. Young's modulus or strength.

Table 3: Fracture toughness values for C70 foams

Density	K_{IC}	K_{IIC}
kg/m^3	$Mpa.m^{0.5}$	$MPa.m^{0.5}$
200 x-dir.	0.515	0.239
200 y-dir.	0.485	0.232
130 x-dir.	0.283	0.148
130 y-dir.	0.255	0.153
90 x-dir.	0.235	0.076
90 y-dir.	0.242	0.098

4.3.2 K_I and K_{II} values at fracture under mixed-mode loading

Mixed-mode toughness values were derived in a similar fashion as K_{IC} and K_{IIC}. Table 4, Table 5 and Table 6 present the mixed-mode toughness values, K_I and K_{II}, at load P_Q under various loading conditions. Each test configuration was repeated three times; results are listed below together with mean values. The circles and crosses in Figure 12 to Figure 14 indicate experimental results; K_{II}/K_{IC} is plotted against K_I/K_{IC} (the value of K_{IC} was that from Table 3). As K_I/K_{IC} decreases and the mode-II loading contribution increases, i.e. as α increases from 0° up to 90°, K_{II}/K_{IC} increases. In the mixed-mode cases, mode-I contribution is greater than that of mode-II; this is true for all three foam densities.

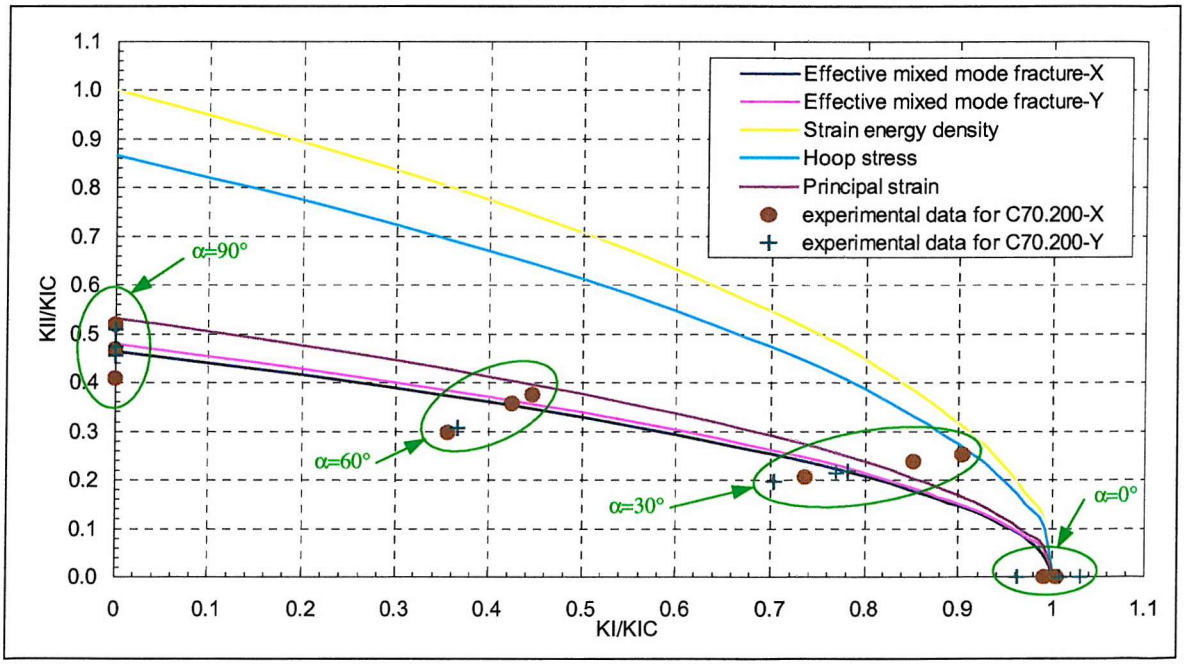

Figure 12: Fracture boundary curve and experimental results for C70.200

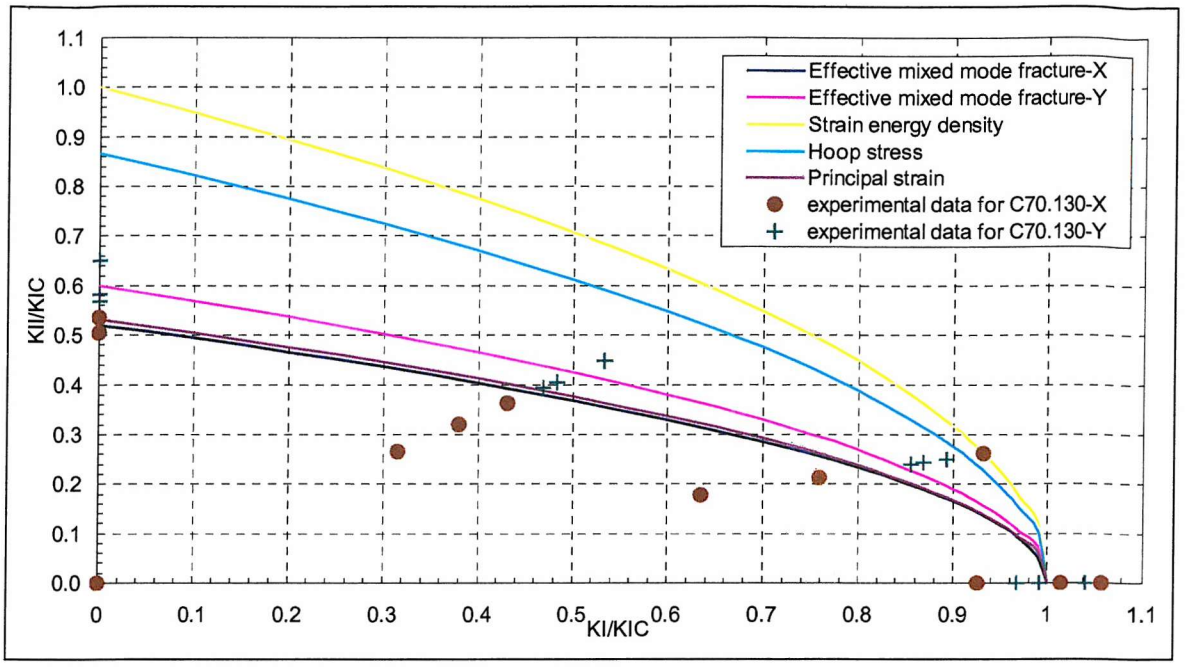

Figure 13: Fracture boundary curve and experimental results for C70.130

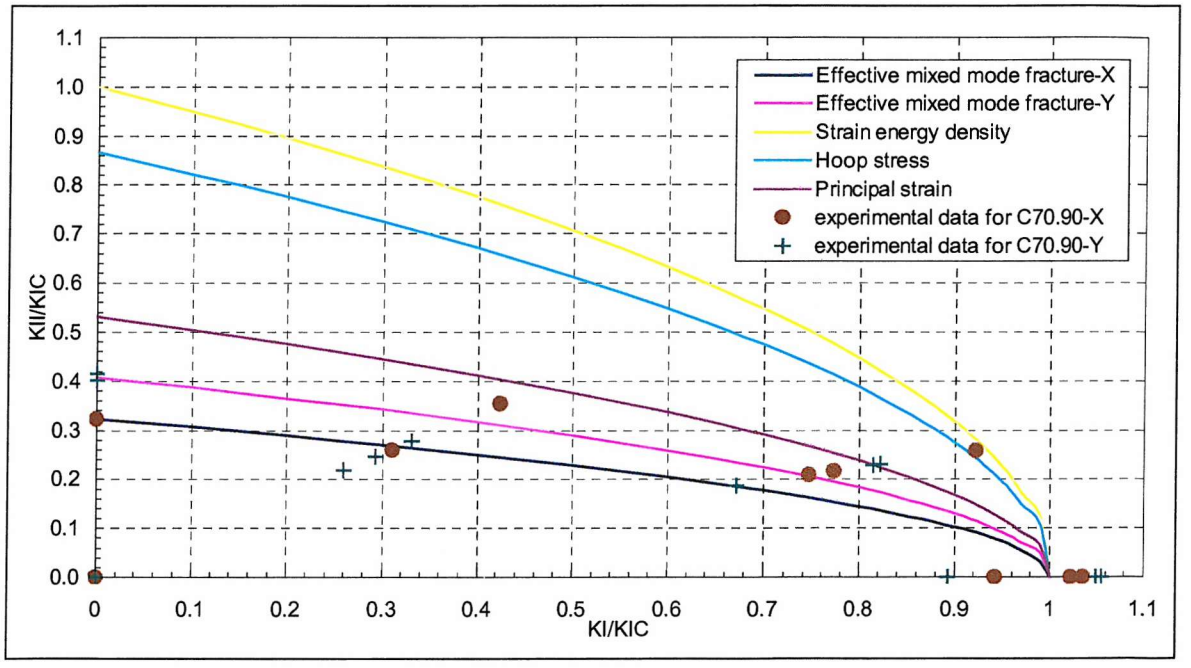

Figure 14: Fracture boundary curve and experimental results for C70.90

Table 4: Mean mixed-mode toughness values K for C70.200, 130 and 90 foams

α	0°	30°		60°		90°
	K_I	K_I	K_{II}	K_I	K_{II}	K_{II}
200 x-dir.	0.515	0.428	0.120	0.211	0.177	0.239
200 y-dir.	0.485	0.364	0.102	0.178	0.149	0.232
130 x-dir.	0.283	0.220	0.061	0.106	0.089	0.148
130 y-dir.	0.255	0.222	0.062	0.126	0.106	0.153
90 x-dir.	0.235	0.191	0.053	0.057	0.048	0.076
90 y-dir.	0.242	0.186	0.052	0.071	0.060	0.098

In order to evaluate the spread of the results shown Figure 12 to Figure 14, a statistical analysis was conducted. Table 5 tabulates the means and ranges for the C70.200 foam. From this, it can be observed that dispersion is small. For the C70.130 and the C70.90 foams as well, although the dispersion is marginally higher, the trends are similar.

Table 5: Statistical data on mixed-mode toughness K for C70.200 foam

α	0°	30°		60°		90°
X-dir.	K_I	K_I	K_{II}	K_I	K_{II}	K_{II}
Mean	0.515	0.428	0.120	0.211	0.177	0.239
Range (%)	0.007	0.087	0.024	0.047	0.039	0.057
Y-dir.	K_I	K_I	K_{II}	K_I	K_{II}	K_{II}
Mean	0.485	0.364	0.102	0.178	0.149	0.232
Range (%)	0.033	0.038	0.011	0.000	0.000	0.026

4.3.3 Kinking angle Ψ

A propagating crack seeks the direction of the maximum crack driving force and the direction of minimum material resistance. It does not need to be confined to its initial plane. The fracture deflection angle or kinking angle may be defined as the angle between the direction of the initial crack and the direction taken by the propagating crack. Theoretical kinking angles can be predicted by the mixed-mode fracture criteria. Experimental results pertaining to the kinking angle versus $K_{II}/(K_I+K_{II})$ are plotted in Figure 15 for C70.200, 130 and 90 foams; see also results in Table 6 for a listing. Pure Mode-I loading induces a nil kinking angle, as expected. As mode-II loading increases relative to Mode-I loading, kinking angle increases up to a maximum value of between 55° and 62°. The trend is similar for the three types of foam. However, kinking angle values are slightly different for each density and seem to decrease marginally as density decreases. The variability of the crack angle is about ± 5°.

Table 6: Mean kinking angle ψ for C70.200, 130 and 90 foams

α	0°	30°	60°	90°
200 x-dir.	0	27	44	61
200 y-dir.	0	29	43	61
130 x-dir.	0	30	43	59
130 y-dir.	0	28	43	59
90 x-dir.	0	27	39	56
90 y-dir.	0	27	38	61

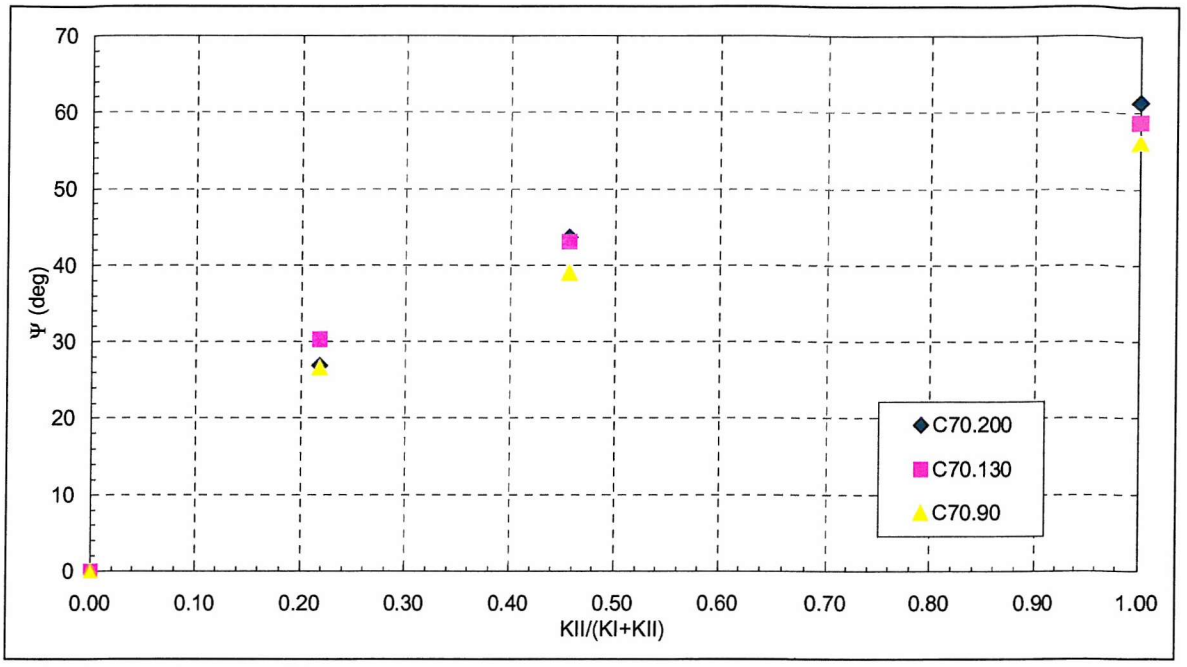

Figure 15: Kinking angle ψ experimental results for C70.200, 130 and 90 foam

4.4 Theoretical model

4.4.1 Elasto-static crack tip solution

Assuming plane strain and the existence of an Airy stress function Φ, the elasticity equation can be written:

$$\nabla^2\left(\nabla^2\Phi\right)=0 \tag{5}$$

The stress function Φ at the tip of a sharp crack is given by:

$$\Phi = r^{\lambda+1}g(\varphi) \tag{6}$$

where (r,φ) are polar co-ordinates and λ is the strength of the singularity at the tip of the crack, see Figure 16.

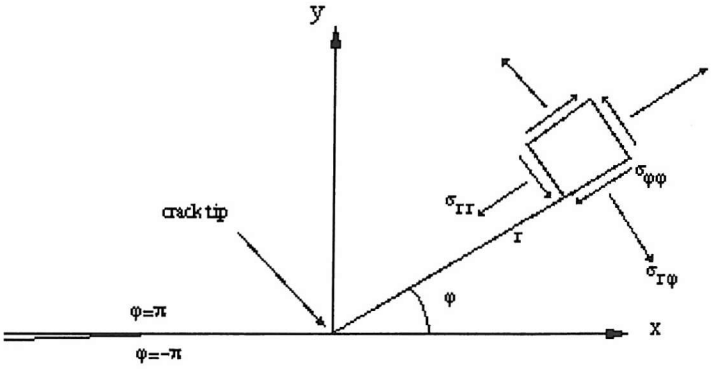

Figure 16: Crack tip in infinite plane body

A general solution of the bi-harmonic equation may be obtained from:

$$g(\varphi)=c_1\cos[(\lambda-1)\varphi]+c_2\sin[(\lambda-1)\varphi]+c_3\cos[(\lambda+1)\varphi]+c_4[(\lambda+1)\varphi] \tag{7}$$

where c_i are constants.

For an isotropic material, the stresses can be derived as follows:

$$\begin{cases} \sigma_{rr} = \dfrac{1}{r}\dfrac{\partial \Phi}{\partial r} + \dfrac{1}{r^2}\dfrac{\partial^2 \Phi}{\partial \varphi^2} = r^{\lambda-1}\left\{(\lambda+1)f + \dfrac{d^2 f}{d\varphi^2}\right\} \\ \sigma_{\varphi\varphi} = \dfrac{\partial^2 \Phi}{\partial r^2} = \lambda(\lambda+1)r^{\lambda-1} f \\ \sigma_{r\varphi} = -\dfrac{\partial}{\partial r}\left(\dfrac{1}{r}\dfrac{\partial \Phi}{\partial \varphi}\right) = -\lambda r^{\lambda-1}\dfrac{df}{d\varphi} \end{cases} \tag{8}$$

or

$$\begin{cases} \sigma_{rr} = \dfrac{K_I}{\sqrt{2\pi r}}\left(\dfrac{5}{4}\cos\left(\dfrac{\varphi}{2}\right) - \dfrac{1}{4}\cos\left(\dfrac{3\varphi}{2}\right)\right) + \dfrac{K_{II}}{\sqrt{2\pi r}}\left(-\dfrac{5}{4}\sin\left(\dfrac{\varphi}{2}\right) - \dfrac{3}{4}\sin\left(\dfrac{3\varphi}{2}\right)\right) + 0(r) \\ \sigma_{\varphi\varphi} = \dfrac{K_I}{\sqrt{2\pi r}}\left(\dfrac{3}{4}\cos\left(\dfrac{\varphi}{2}\right) + \dfrac{1}{4}\cos\left(\dfrac{3\varphi}{2}\right)\right) + \dfrac{K_{II}}{\sqrt{2\pi r}}\left(-\dfrac{3}{4}\sin\left(\dfrac{\varphi}{2}\right) - \dfrac{3}{4}\sin\left(\dfrac{3\varphi}{2}\right)\right) + 0(r) \\ \sigma_{r\varphi} = \dfrac{K_I}{\sqrt{2\pi r}}\left(\dfrac{1}{4}\sin\left(\dfrac{\varphi}{2}\right) + \dfrac{1}{4}\sin\left(\dfrac{3\varphi}{2}\right)\right) + \dfrac{K_{II}}{\sqrt{2\pi r}}\left(\dfrac{3}{4}\cos\left(\dfrac{\varphi}{2}\right) + \dfrac{3}{4}\cos\left(\dfrac{3\varphi}{2}\right)\right) + 0(r) \end{cases} \tag{9}$$

4.4.2 Fracture criteria

When plane mixed-mode conditions - mode-I and mode-II - apply at the tip of a straight sharp crack in a plane specimen, the fracture behaviour may be described in a material-dependent fracture boundary curve, extending between the fracture toughness K_{IC} and K_{IIC} for pure mode-I or mode-II fracture. The fracture criterion also covers a prediction for the deflection angle of crack growth. Different criteria based on the linear elastic stress field were investigated.

4.4.2.1 Maximum hoop stress criterion and maximum shear stress criterion

The maximum hoop stress criterion was proposed by Erdogan and Sih[85]. Assuming the stress state to be determined by the singular part of the linear elastic stress field, the crack extension starts from its tip along the radial direction $\varphi = \varphi_{IC}$ on which $\sigma_{\varphi\varphi}$ becomes maximum. The hypothesis can be expressed mathematically by the relations:

$$\frac{\partial \sigma_{\varphi\varphi}}{\partial \varphi} = 0 \text{ and } \frac{\partial^2 \sigma_{\varphi\varphi}}{\partial \varphi^2} < 0 \tag{10}$$

Fracture starts when $\sigma_{\varphi\varphi}$ has the same value as in equivalent opening-mode, that is

$$\sigma_{\varphi\cdot\varphi}(\varphi = \varphi_{IC}) = \frac{K_{IC}}{\sqrt{2\pi r}} \tag{11}$$

The maximum shear stress criterion hypothesis is equivalent to the previous hoop stress criterion but for a mode-II type growth, i.e. fracture occurs in the radial direction, parallel

with the plane of maximum shear stress. The derivation is identical to that of the maximum hoop stress criterion.

$$\sigma_{r\cdot\varphi}(\varphi=\varphi_{IIC})=\frac{K_{IIC}}{\sqrt{2\pi r}} \tag{12}$$

4.4.2.2 Minimum strain energy density criterion

The minimum strain energy density criterion was suggested by Sih[28,29]. The criterion states that fracture initiation is towards the point where the strain energy density factor M_{in} has a stationary value. The crack criterion is stated as:

$$\frac{dS}{d\varphi}=0 \text{ and } \frac{d^2S}{d\varphi^2}>0 \tag{13}$$

Fracture initiation occurs when S reaches a critical value S_{cr}. S and S_{cr} will then be defined as

$$S=\alpha_{11}K_I^2+2\alpha_{12}K_IK_{II}+\alpha_{22}K_{II}^2 \tag{14}$$

$$S_{cr}=\frac{\kappa-1}{8\pi G}K_{IC}^2 \tag{15}$$

4.4.2.3 Maximum principal strain criterion

The principal strain criterion was suggested by Fisher[86]. The criterion uses deformation (or strain) values instead of stress values in the formulation of fracture criteria. Crack propagation is assumed to initiate in the direction ψ_0, where the maximum principal strain and the corresponding equivalent stress intensity factor K_V become minimum; unstable crack propagation starts when $K_V(\psi_0)$ reaches a critical value equal to K_{IC}.

The equivalent stress is derived from conventional stress analysis assuming plane strain conditions:

$$\sigma_V=(1+\nu)[\sigma_1+\nu(\sigma_1+\sigma_2)] \tag{16}$$

Using the singular terms of the approximate solution for the stress field at the crack tip, the equivalent stress intensity factor K_V is found to be:

$$K_V=\frac{\sqrt{2\pi}.\lim_{r\to 0}\left(\sqrt{r}\sigma_V\right)}{(1+\nu)(1-2\nu)} \tag{17}$$

4.4.2.4 Effective mixed-mode fracture criterion

Many of fracture boundary curves can be expressed in the following way, as shown by Richard[87].

$$\frac{K_I}{K_{IC}}+\alpha_1\left(\frac{K_{II}}{K_{IIC}}\right)^2=1 \tag{18}$$

The fracture toughness ratio α_1 can be empirically obtained, and characterises the material under consideration. This can express experimentally obtained fracture boundary curves, and furthermore, it covers previously known criteria, i.e. with $\alpha_1 = 1.00$ the strain energy density criterion, with $\alpha_1 = 2/3^{0.5}$ the hoop stress criterion, with $\alpha_1 = 1.88$ the principal strain criterion.

4.4.3 FE model

The calculations were performed with a multi-purpose FE program, ANSYS 5.3, running on a SUN station. The specimen was modelled using 2042 eight node quadratic collapsed triangular element under plane strain conditions. The a/w ratio varied between 0.45 and 0.55. The mesh was refined around the crack tip; 552 elements of approximate edge length 0.7 mm were used. Around the crack tip 12 quadratic elements with quarter point location, i.e. displaying $1/r^{0.5}$ stress field singularity, were used. The entire specimen was modelled since numerical instability was encountered with a half model. The method used to calculate the stress intensity factors was a simple displacement extrapolation method: this was performed automatically in the ANSYS postprocessor using the LPATH and KCALC commands.

4.5 Numerical results

4.5.1 CTS stress intensity factors

In order to calculate K_I and K_{II}, geometrical factors f(a/w) for both loading modes were determined. A nominal load was applied and non-dimensional stress intensity factors, i.e. geometrical factor f(a/w), were obtained. The a/w ratio was varied between 0.45 and 0.55 and the mixity angle α was varied between 0 and 90 degrees. Since the CTS specimen developed by Richard[87] has very similar dimensions to the specimen used in the investigation, results were expected to be very close. Results are shown in Table 7, Table 8 and Figure 17 and Figure 18. For pure mode-I loading, f_I is maximum. As mode-II loading contribution increases, f_I decreases down to 0 for pure mode-II loading. Geometrical factors for mode-II loading exhibits the opposite trend; as mode-II loading increases, f_{II} increases.

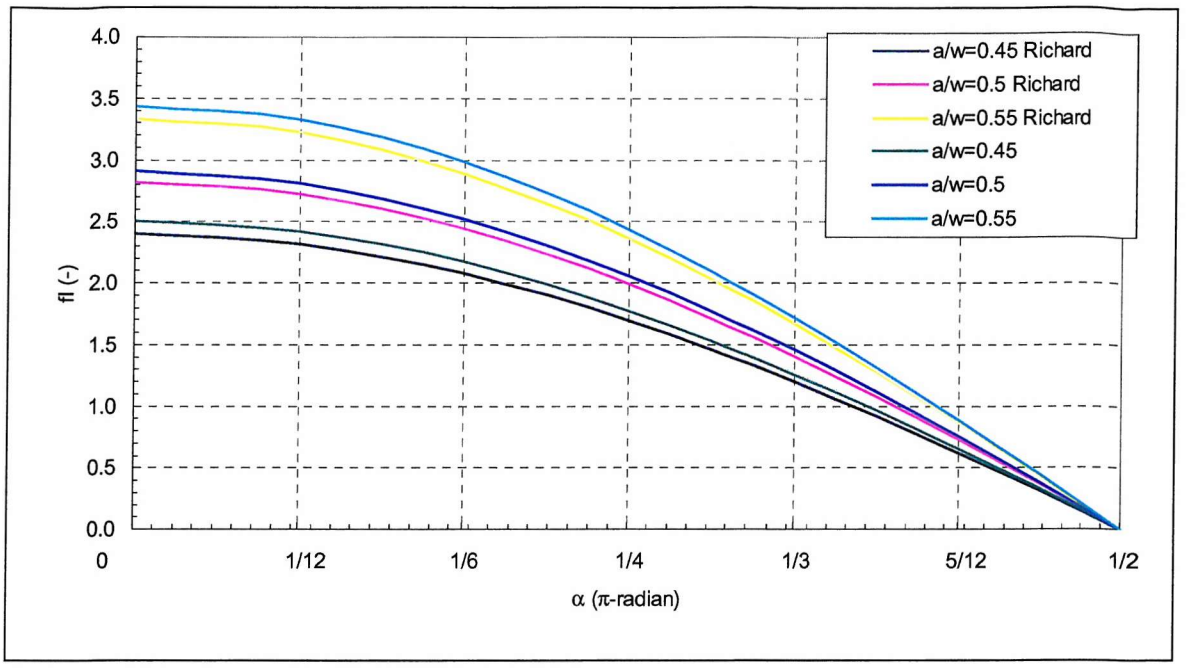

Figure 17: Mode-I geometrical factor comparison

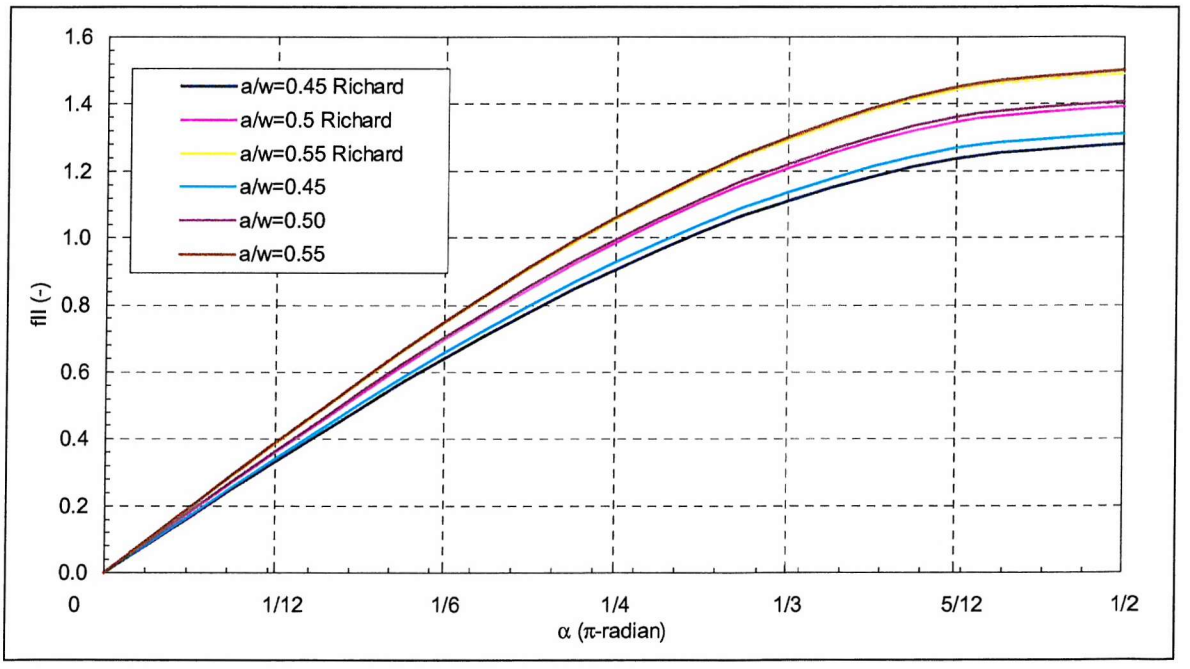

Figure 18: Mode-II geometrical factor comparison

Table 7: Geometrical factor calculated from FE model

α	a/w = 0.45		a/w = 0.50		a/w = 0.55	
(rad)	f_I	f_{II}	f_I	f_{II}	f_I	f_{II}
0	2.5048	0.0001	2.9090	0.0001	3.4388	0.0001
π /12	2.4194	0.3396	2.8108	0.3645	3.3216	0.3885
π /6	2.1692	0.6560	2.5200	0.7041	2.9780	0.7504
π /4	1.7711	0.9276	2.0576	0.9957	2.4315	1.0612
π /3	1.2523	1.1361	1.4550	1.2194	1.7193	1.2996
5□π /12	0.6482	1.2671	0.7531	1.3600	0.8900	1.4495
π /2	0.0001	1.3118	0.0001	1.4079	0.0001	1.5006

Table 8: Geometrical factor for Richard's model

α	a/w = 0.45		a/w = 0.50		a/w = 0.55	
(rad)	f_I	f_{II}	f_I	f_{II}	f_I	f_{II}
0	2.3975	0	2.8140	0	3.3359	0
π /12	2.3158	0.3315	2.7181	0.3607	3.2222	0.3860
π /6	2.0763	0.6405	2.4370	0.6968	2.8889	0.7457
π /4	1.6953	0.9058	1.9898	0.9854	2.3588	1.0546
π /3	1.1988	1.1094	1.4070	1.2068	1.6679	1.2916
5□π /12	0.6205	1.2374	0.7283	1.3460	0.8634	1.4406
π /2	0	1.2810	0	1.3935	0	1.4914

4.5.2 Plastic zone

In the absence of extensive validation of fracture testing methods for polymeric foam in the literature, the ASTM K_{IC} standard for fracture testing of plastics [84] was used. The standard requires the plastic zone size to be smaller than the specimen size. The reasons are to ensure predominant plane strain conditions, and the presence of an elastic singularity zone ahead of the crack tip.

The required sizes were calculated from equation (2) and (3) in order to ascertain the applicability of the specimen dimensions for testing. Table 9 shows the minimum thickness values calculated from (3). The results indicates that the specimen dimensions (a=20 or 22 mm, and t=10 mm) do not fulfil the ASTM size requirements.

Table 9: Thickness requirements according to ASTM K_{IC} standard

ρ	σ_{yield}	K_{IC}	t,a
($kg.m^{-3}$)	($N.mm^{-2}$)	($MPa.m^{0.5}$)	(mm)
200	4.3	0.515	35.9
130	2.4	0.283	34.8
90	2.1	0.242	33.2

Plastic zone sizes for the CTS specimen and the foam materials under considerations were then evaluated from a FE investigation. Figure 19 shows the Von Mises isostress lines resulting from the FE analysis for a given case, i.e. C70.200 foam type and a loading angle $\alpha = 30°$. The applied fracture load was P_Q=271 N corresponding to a K_I=0.428 $MPa.m^{0.5}$ and K_{II}=0.120 $MPa.m^{0.5}$. The stress contours corresponding to a σ_{limit} of 3 MPa and σ_y of 4.3 MPa can be deduced from the figure. By transposing each of the two areas into two circles of equal area, the zone radius is found to be approximately 4.1 mm and 3.2 mm for σ_{limit} and σ_y respectively. These are of the same order of magnitude as the values predicted by LEFM theory as shown in Table 10. Numerical plastic zone size was estimated for the three densities under consideration, and for α ranging from 0° to 90°, see Table 11. The plastic zone radius decreases with decreasing density. The plastic zone size relation to the mode-mixity is not so obvious but it is larger in either pure mode-I or II loading and reaches a

minimum value in mixed-mode loading. Note that the analytical and numerical results show a plastic zone size remaining below the critical value of the specimen thickness, i.e. 10 mm. Although all the specimen sizes are larger than the ASTM required size, the fracture toughness values obtained from the experimental investigations have shown good agreement with independent test results - this will be expanded on later in this chapter. The results have also shown good agreements with fatigue test results presented in Chapter 5. This indicates that: the ASTM size requirements are conservative, and too severe for this material; and that the analytical and numerical values obtained for the plastic zone size are adequate.

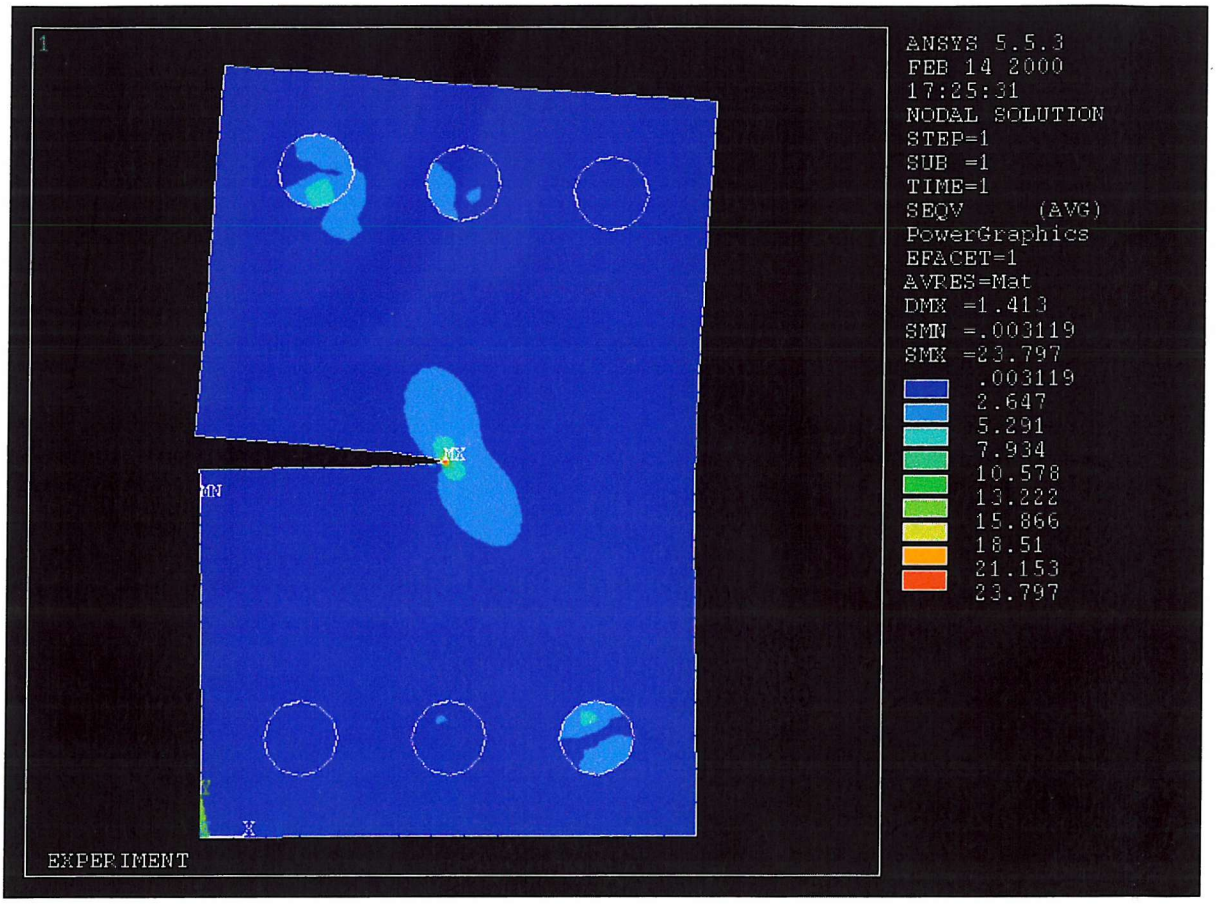

Figure 19: Von Mises isostress lines at fracture load from FEA for C70.200 at $\alpha = 30°$

Table 10: Size of the plastic zone at load P_Q according to LEFM theory in Mode-I

ρ	σ_{limit}	σ_{yield}	K_{IC}	r_I	r_D
($kg.m^{-3}$)	($N.mm^{-2}$)	($N.mm^{-2}$)	($MPa.m^{0.5}$)	(mm)	(mm)
200	3.00	4.3	0.515	1.52	5.63
130	1.75	2.4	0.283	1.48	5.46
90	1.65	2.1	0.242	1.41	5.21

I: according to Irwin for plane strain in Mode-I
D: according to Dugdale for plane stress in Mode-I

Table 11: Size of the plastic zone at load P_Q from FEA

ρ (kg.m^{-3})	α	(deg)	0°	30°	60	90°
200	r_{FE}	(mm)	3.2	4.0	1.9	6.6
130	r_{FE}	(mm)	3.1	3.9	1.8	6.4
90	r_{FE}	(mm)	2.9	3.7	1.7	6.1

4.6 Discussion

4.6.1 Test technique

The CTS specimen in combination with Richard's loading device offers numerous advantages. First, it is a simple test procedure and mixed-mode toughnesses are easily calculated. Reliability of the plane strain condition is high. The specimen is compact and clamping/un-clamping is easy to achieve. Fatigue pre-cracking is available under mode-I and fatigue testing is also available under pure mode-I, -II and mixed-mode. A full range of mixed-mode-I/II combinations can be set accurately and repeated. A four-point bending specimen only offers the possibility to test under pure mode-II at its centre, and very accurate test set-up is necessary to achieve a given mixed-mode.

CTS specimen practical dimensions can be kept to a minimum for testing at small fracture loads. With four-point bending testing, the loads would have been extremely small for the foams considered here.

4.6.2 Fracture toughness K_{IC} and K_{IIC}

The experimental results on pure mode-I and mode-II fracture toughness of AIREX C70 foam are reproducible for the three densities under consideration. The fracture toughness ratio K_{IIC}/K_{IC} varies between 0.4 and 0.65 depending on the foam density.

Table 12[88] shows mode-I fracture toughness data of a similar material from another supplier, DYVINICELL. The DYVINICELL product, like that manufactured by AIREX and used in this study, is a rigid cross-linked PVC foam with very similar chemical composition[89]. The largest difference in fracture toughness, between the DYVINICELL values and the authors is 14%, while the mean difference is about 5%. The average values of experimentally obtained fracture toughness thus compare well with independent values. Figure 20 shows a linear relationship between fracture toughness and density for the range of densities under consideration. It may however be premature to generalise this inference to a larger spectrum of densities. Zenkert[26] found an approximate linear relationship between mode-I fracture toughness and average cell size, which is in agreement with the results of our investigation.

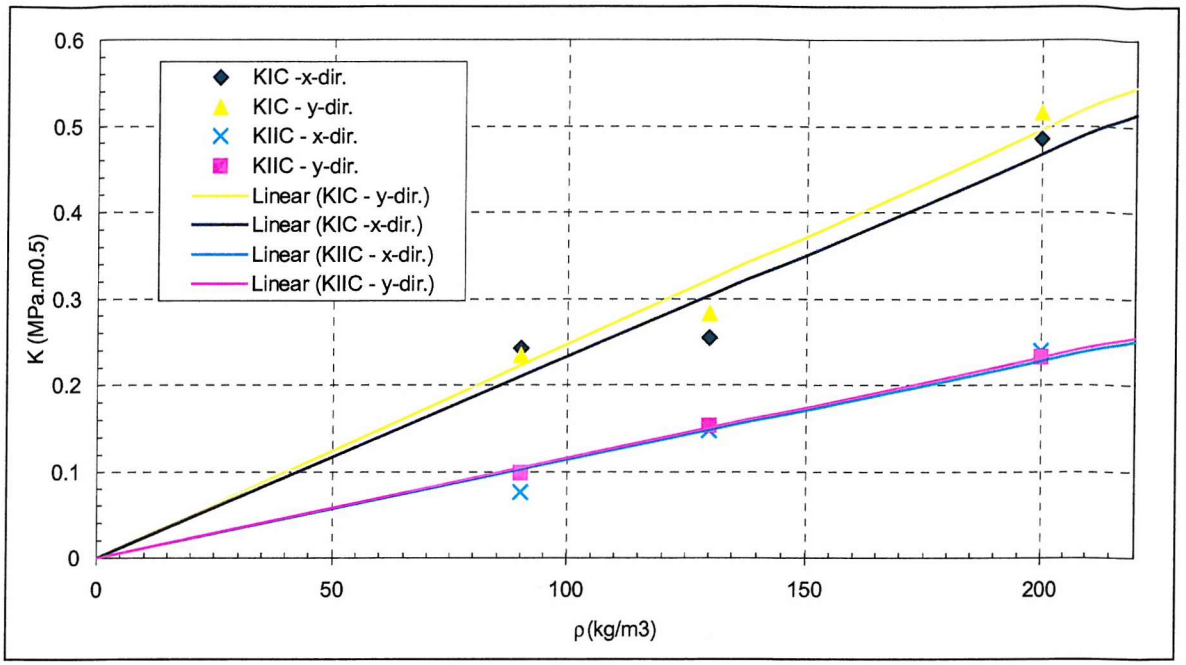

Figure 20: Relationship between fracture toughness and density of C70 foam

Table 12: Mode-I fracture toughness comparison with independent data

Density	K_{IC}	Difference
kg/m^3	MPa.m$^{0.5}$	%
200 x-dir.	0.56	-8.0
200 y-dir.	0.47	3.2
130 x-dir.	0.33	-14
130 y-dir.	0.28	-8.9
90 x-dir.	0.24 (*)	-2.1
90 y-dir.	0.25 (*)	-3.2

(*) linear extrapolation from DYVINICELL H100 [90].

4.6.3 Directionality influence

Fracture toughness is different according to the direction of the material, Table 3. This difference may reach 10% for the C70.130 foam. The directionality effect was also noticed by Stibe [88] when comparing blocks of the same type of material, namely DYVINICELL. Figure 20 shows that a linear relationship exists between fracture toughness and density for the densities under examination. The constant of proportionality is dependent upon crack direction; it is lower for a y-direction crack. The most likely cause is the manufacturing process. First, polymers are foamed using physical or chemical blowing agents; various techniques are used. The product is then rolled in order to produce sheets of a given thickness. During this process, cell morphology can be altered. Cell shape and walls can be slightly stretched in the rolling direction inducing a light orthotropy. This should not have implications for design since variations are small for engineering purpose.

4.6.4 K_I and K_{II} values

The experimental results on mixed-mode fracture appear to be consistent with each other. Figure 12 to Figure 14 show the fracture envelopes of various criteria. First, consider the hoop stress and strain energy criteria. It can be seen that the trends predicted by the criteria correlate well with the experimental values only for high values of K_I/K_{IC} (and low values of K_{II}/K_{IC}), i.e. low mode-II contribution zone. The principal strain criterion is a good predictive model, but for C70.90 it overestimates K_{II} for K_I/K_{IC} values less than 0.8. If no experimental data on K_{IC} and K_{IIC} are available, the principal strain criterion appears to be a good predictive model but not conservative. If test data are available, however, the effective mixed-mode fracture criterion (EMFC) predicts more accurately the fracture envelope. Results of C70.130 foam do not match as well as the C70.200 and C70.90. Here, the fracture loci also are overestimated. A small error in K_{IC} and K_{IIC} experimental values can lead to a poor estimate of the fracture loci, since EMFC is based on experimental K_{IC} and K_{IIC} values.

4.6.5 Kinking angle ψ

The experimental results are homogeneous and present almost no scatter. No influence of directionality was noticed on kinking angle. The kinking angle decreases slightly as density decreases. Fracture criterion predictions for kinking angle ψ are presented in Figure 21 together with experimental results. It is seen that all the theories yield good results for α values ranging from 90° to 60°. For lower α values, the hoop stress, the strain energy density, and the principal strain criteria overestimate largely the fracture angle. Predictions become even higher as α gets close to 0, i.e. pure mode-II. The hoop stress criterion is in better agreement than the two other criteria. Here, if no experimental kinking angle value is available, the maximum hoop stress criterion is the best predictive model. The effective mixed-mode criterion seems to predict more accurately the fracture angle, even if K_{IC} and K_{IIC} are experimentally-obtained for the material considered here.

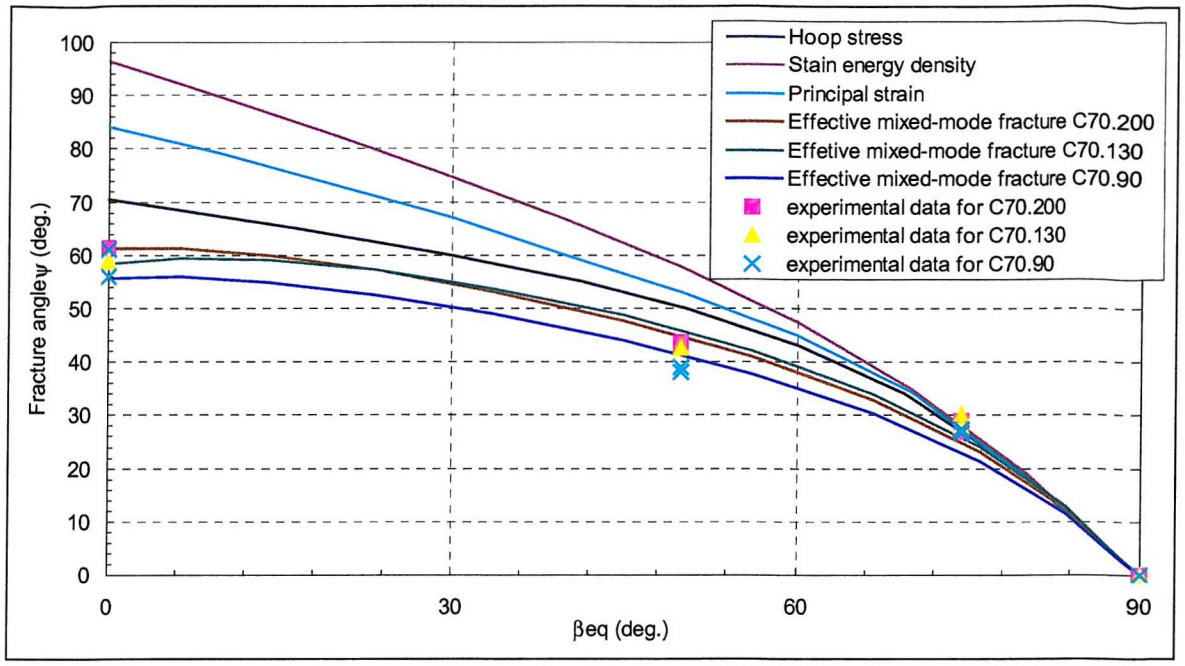

Figure 21: Predicted fracture angle ψ and experimental results

4.6.6 Numerical investigation

The FE determination of the stress intensity factors K_I and K_{II} for the Richard's modified CTS specimen yield good results. They are close to Richard's specimen stress intensity factors values, as expected and compare well with independent FE values, see Figure 17 and Figure 18.

Table 10 and Table 11 show plastic zone size radius calculated using LEFM and FE analysis. Both sets of results are of the same order of magnitude. Figure 19 exhibits a plastic zone having a radius of approximately 4 mm, and consequently smaller than specimen dimensions. This is of the same order of magnitude as the figure predicted by LEFM theory, i.e. 1.5 and 6 mm. The plane-strain state is validated here. The same conclusions apply for all the specimens tested.

4.7 Conclusions

From the results and the discussion, one can draw several conclusions. For the studied dimensions and loading rate, it is found that linear elastic fracture mechanics can be applied with good accuracy to the materials under considerations; FE investigation supports this inference. The CTS specimen, in association with a special loading device, is an appropriate apparatus for experimental mixed-mode fracture analysis. Experimentally obtained fracture toughness values results have shown good accuracy and can therefore be used as fracture parameters for engineering purpose. K_{IC} fracture toughness is higher in either one of the x or y-direction with variations up to 10%. The mode-I fracture toughness is larger than the

mode-II fracture toughness; experimental results show that the ratio K_{IIC}/K_{IC} lies between 0.4 and 0.65.

The mixed-mode fracture criteria also predict $K_{IIC}<K_{IC}$. For mixed-mode loading, Richard's criterion, using experimentally obtained K_{IIC} and K_{IC}, seems to be the best in predicting fracture locus and fracture angle accurately. The principal strain criterion appears to be a good predictive model for fracture locus independently of material characteristics. The maximum hoop stress criterion also predicts the fracture angle well. The theory appears to be deficient in predicting accurately both fracture locus and fracture angle. Fracture locus and kinking angle are best predicted for low mode-II contributions.

5 CRACK GROWTH IN RIGID CELLULAR FOAM UNDER MODE-I, MIXED-MODE, MODE-II CYCLIC LOADING

5.1 Purpose and objectives

Chapter 4 discussed the static fracture behaviour of foams under various loading conditions through testing and numerical studies. The aim of this chapter is to extend the understanding of fatigue crack growth subjected to mode-I, mixed-mode, mode-II cyclic loading.

The first specific objective is to determine the crack growth rate under various loading conditions. Another goal is to study the relationship between the stress intensity factors and crack growth rates. The two other goals are to study the fatigue and fracture behaviour at both micro- and macroscopic level and assess diverse mixed-mode criteria.

5.2 Test method and set up

5.2.1 Materials

The material used in this investigation was a PVC cross-linked cellular foam made by AIREX. It is made of closed cells and typically exhibits low fracture toughness and brittle fracture behaviour. A foam type of nominal density 130 kg/m3, referred as C70.130, was used. The typical cell size ranges approximately from 0.2 mm to 0.4 mm. Representative mechanical properties of the foam materials in tension and shear are summarised Table 13.

Table 13: Properties of C70.130 AIREX foam in tension and shear

σ	E_{tens}	G	σ_{limit}	σ_{yield}	K_{IC}	K_{IIC}
(kg/m^3)	(MPa)	(MPa)	(MPa)	(MPa)	($MPa.m^{0.5}$)	($MPa.m^{0.5}$)
130	109	50	1.75	2.4	0.28	0.15

Note that here $\sigma_y = \sigma$ at 0.2% offset

5.2.2 Test rig and set up

A simple and compact fracture mechanics specimen was used for the determination of fatigue crack growth under mode-I, mode-II and mixed-mode loading conditions. The loading device was simply installed in an Instrom 8500 universal testing machine and generated accurately repeatable multi-axial loading conditions, see Figure 22.

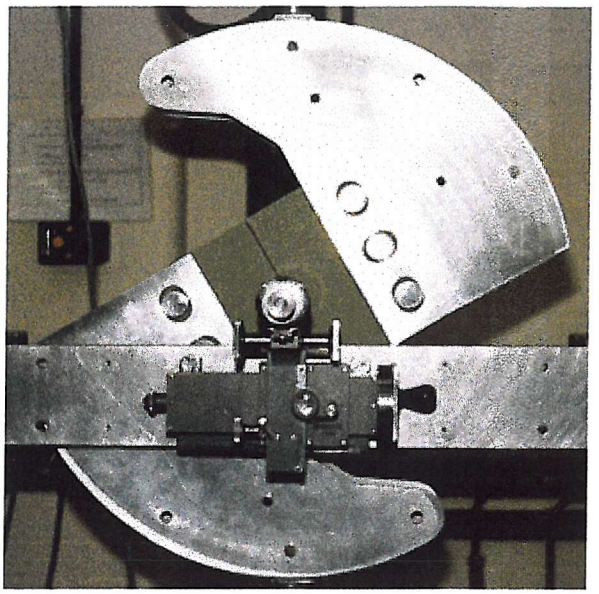

Figure 22: Experimental apparatus (loading jig and travelling microscope) and test specimen in green in a mixed-mode loading configuration

The test specimens corresponded to the dimensions of 300 x 200 x 50 mm, see Figure 23. The specimen size had to be sufficiently large to permit accurate crack growth measurements. The direction of the specimens was kept identical to avoid scatter originating from potential light anisotropy. Three holes were drilled along the top and bottom edges of the specimen. Sharp crack-shaped notches were made with a thin band saw of 0.8-1 mm thickness with a/w = 0.45. The tip part of the crack was made with a razor blade up to a/w = 0.5. None of the specimens was fatigue pre-cracked.

A total of 18 specimens were tested in this survey. Pure mode-I, pure mode- II and two mixed-mode loading conditions were used as shown in Table 14. Tests were repeated 3 times. The tests were load-controlled and the test loading frequency was 1 Hz. The frequency was determined such that the strain rate would not exceed the value of $10\%s^{-1}$ - in order to avoid any visco-elastic effect due to temperature increase [47,51,52]. Specimens were subjected to a constant amplitude sinusoidal load cycles at the same load ratio R equal to 0.1. The specimen loading was started at the mean value of P_{max} and P_{min}. The maximum cyclic load P_{max} was chosen to be approximately 66% of the previously established static fracture load $P_{fracture}$ [91]. For the $\alpha = 30°$ case, two series of tests were carried out with P_{max} equal to 66% and 85% of $P_{fracture}$. Number of cycles and crack tip positions were recorded periodically during each test. An optical travelling microscope having a magnification of up to x50 gave an accurate position of the crack tip. All tests, 18 in total, were carried out using an Instron model 8502 universal testing machine.

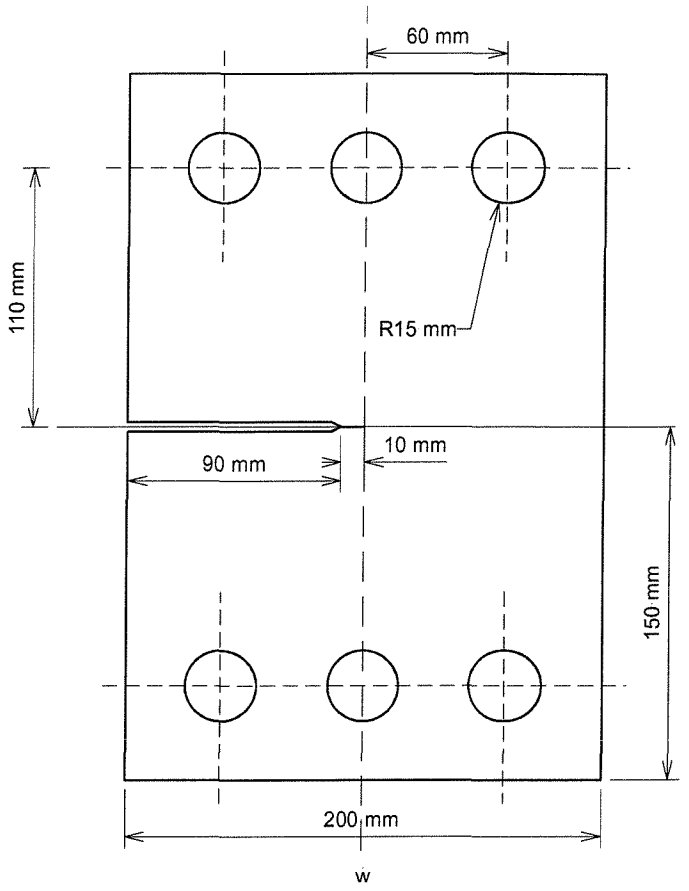

Figure 23: Fatigue CTS fracture specimen geometry

Table 14: Mode mixity and cyclic load values vs. loading angle α

Mode mixity	pure mode-I	mixed-mode	mixed-mode	pure mode-II
α	0°	30°	60°	90°
$P_{fracture}$ (N)	1750	1611	1344	1863
P_{max} (N)	1200	1071	894	1239
P_{min} (N)	120.0	107.1	89.4	123.9

5.2.3 Standard tests and assumptions

The Standard Test Method for Measurement of Fatigue Crack Growth Rates, ASTM E647-93 [92], describes how to determine da/dN as a function of ΔK from an experiment. The test features and specimen design are essentially identical to those required for fracture toughness testing, described in *The Standard Test Method for Plane Strain Fracture Toughness and Strain Energy Release Rate of Plastic Materials*, ASTM E 5045-95 [84]. The main specimen size requirement for fatigue testing is:

$$W - a \geq \frac{4}{\pi}\left(\frac{K_{max}}{\sigma_Y}\right)^2 \qquad (19)$$

This requirement was met by the CTS specimen used in the investigation. Whilst other requirements were not strictly applicable, the same principles were used.

There are no specific requirements on specimen thickness. Accurate optical measurements of the crack length require a travelling microscope. The ASTM standard

E647 suggests two alternative numerical methods to compute the da/dN: a linear differentiation approach or an incremental polynomial approach. LEFM is the primary requirement.

No standards exist for plane strain mode-II fracture toughness and mixed-mode fracture or for fatigue in mode-II / mode (I+II).

5.2.4 Test method

Cracks were grown under cyclic loading, with K_{min}, K_{max}, and crack length being monitored throughout the tests. Crack lengths versus N curves were plotted. These curves were differentiated to infer da/dN using a linear differentiation approach, which is the simplest but subject to scatter:

$$\left(\frac{da}{dN}\right)_a = \frac{a_{i+1} - a_i}{N_{i+1} - N_i} \tag{20}$$

$$a = \frac{a_{i+1} + a_i}{2} \tag{21}$$

Initial applied K_{min} and K_{max} values were calculated from the following equation:

$$\Delta K = K_{max} - K_{min} \tag{22}$$

$$K_{I,II} = \frac{P\sqrt{\pi a}}{wt} f_{I,II}\left(a/w\right) \tag{23}$$

From the mode-I tests, the Paris law material constant, m, was obtained from the slope of da/dN versus ΔK curve plotted on a log scale.

$$\frac{da}{dN} = C(\Delta K)^m \tag{24}$$

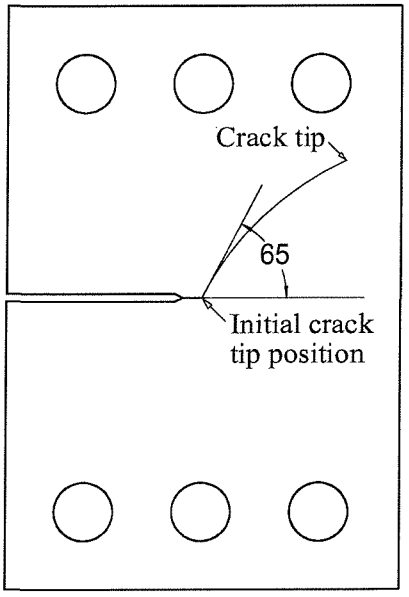

Figure 24: Initial kinking angle for a pure mode-II specimen

Initial kinking angles were measured using a moving protractor in conjunction with an optical microscope (having a magnification from x10 to x50) after test completion. Under mixed-mode and pure mode-II loading conditions, crack deflection occurred on initial loadings, e.g. about 65° for a specimen under pure mode-II loadings, see Figure 24. Initial kinking angles were also computed from the periodic measurements of the crack tip position recorded during the test.

5.3 Experimental results

5.3.1 Crack paths

5.3.1.1 Initial crack deflection angle.

Pure Mode-I loading, i.e. $\beta_{eq} = 90°$ where $\beta_{eq} = \text{Arctan}\,(K_I/K_{II})$, gives a nil kinking angle, as expected. As mode- II loading increases relatively to mode-I loading, i.e. β_{eq} decreases from 90 to 0°, kinking angle increases up to a maximum value of 65° (± 2°), see Figure 25.

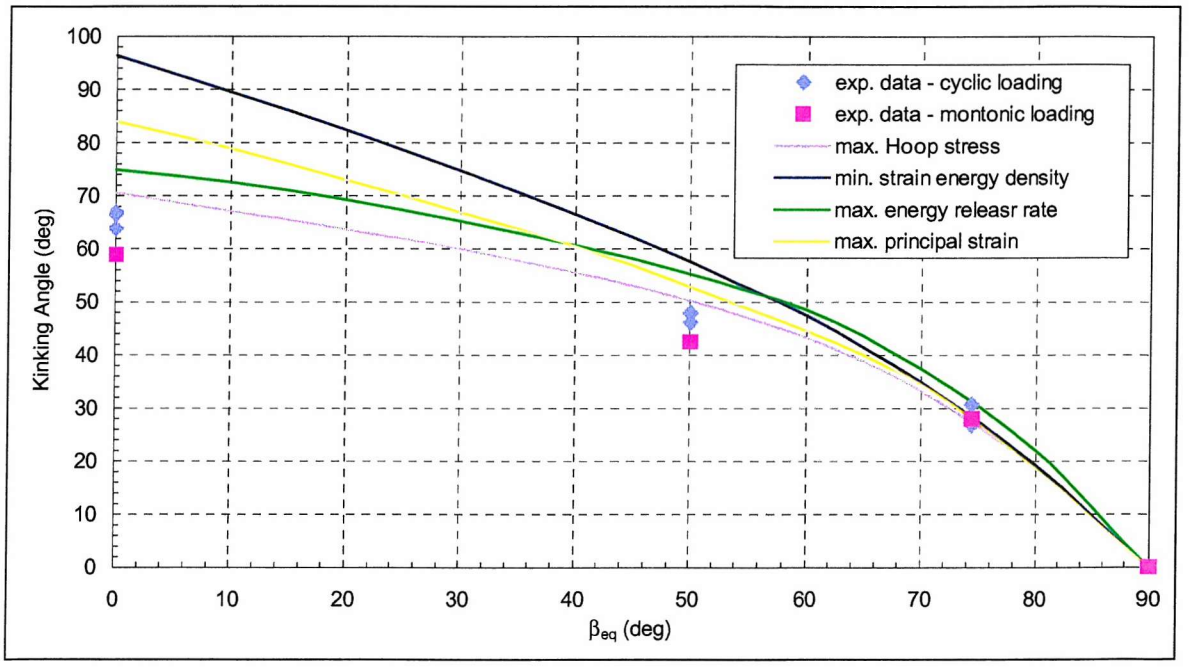

Figure 25: Initial kinking angle as a function of applied load conditions

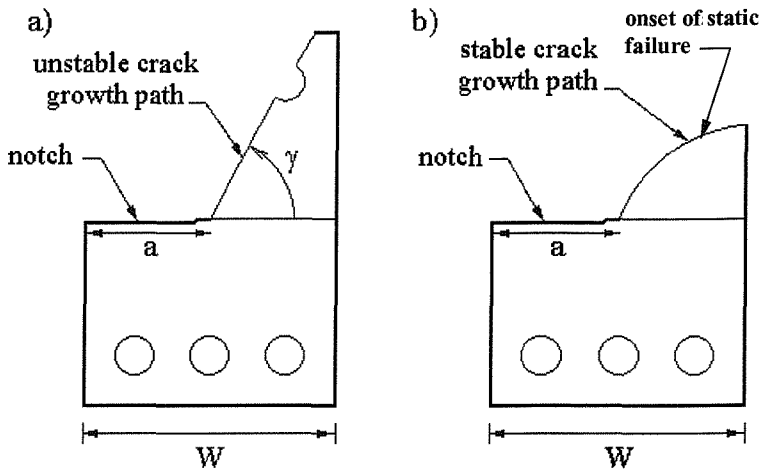

Figure 26: Crack path behaviour associated with mixed-mode and mode-II tests – (a) fracture, (b) fatigue test

5.3.1.2 Macroscopic crack path[PN5]

Overall observations of mixed-mode and pure mode-II specimen show that the direction taken by the propagating crack does not remain constant, i.e. its path is curved. Figure 26a shows the trend under static loading while Figure 26b shows the curved path under fatigue, i.e. where the crack grows in a stable manner. This will be expanded on later.

5.3.1.3 Microscopic observations

Under pure mode-II loading conditions, it was noted that cracks start to propagate in pure shear, i.e. co-planar with the initial notch, over a distance of a few cell widths. After arrest of this co-planar crack propagation, a new crack grew from the notch root and propagated at an initial angle of about 65° until catastrophic failure, see Figure 27.

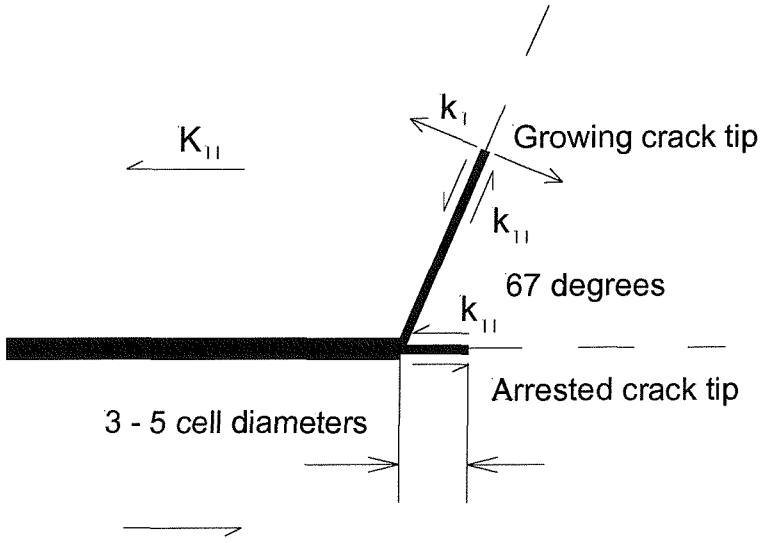

Figure 27: Mode-I versus mode-II crack propagation competition

5.3.2 Crack growth rates

5.3.2.1 Crack propagation

Experimental results for crack length versus number of load cycles, $\alpha = 30°$ and P_{max} = 85% and 66% of $P_{fracture}$ are plotted in Figure 28. The data show that the tests are repeatable and quite consistent with each other. Initially, the rate of crack growth, with increasing N, is small. It, then, extends rapidly in an exponential manner until final failure. Lower P_{max} has a very significant effect; it results in a substantial increase in fatigue life.

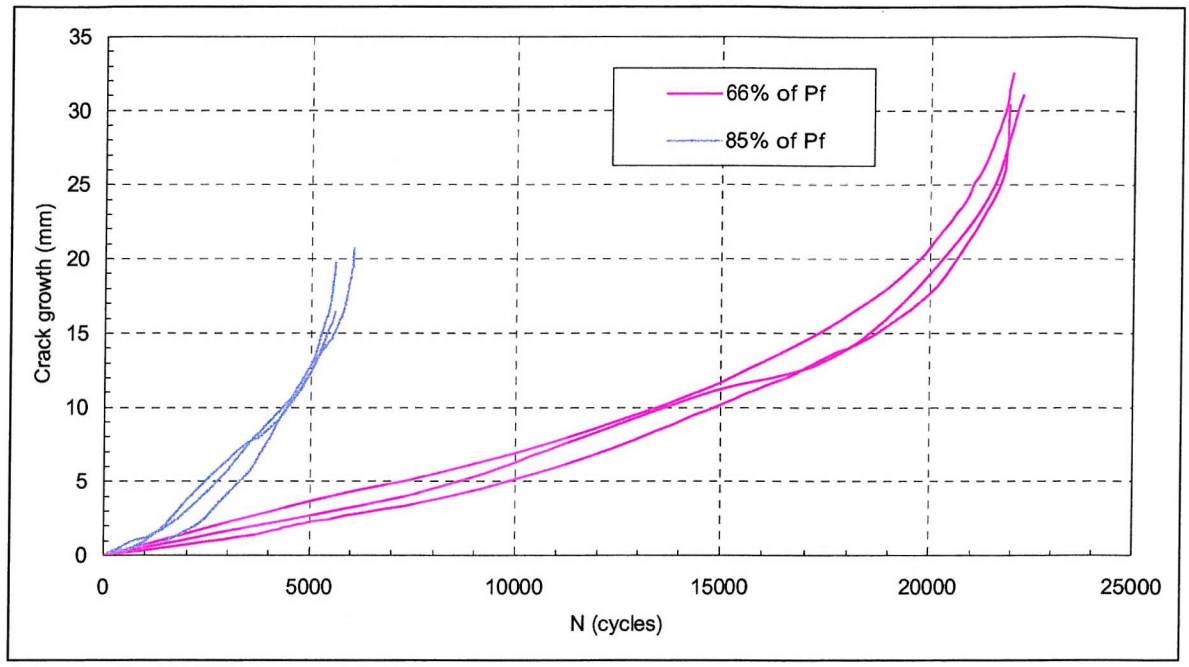

Figure 28: Crack growth vs. number of cycles for 85% and 66% of $P_{fracture}$

5.3.2.2 Initial crack growth rate

For pure mode-I loading, no kinking occurred and therefore full da/dN curves could be obtained from standard compliance functions. For mixed-mode and pure mode-II loading, the crack deflected at the initial crack tip position. ΔK_I and ΔK_{II} were therefore not valid anymore. Local mode-I and mode-II stress intensity factors, Δk_I and Δk_{II}, may be computed for a pupative kinking elastic crack using equations (25,26). Δk_I and Δk_{II} can be expressed in the form:

$$k_I = a_{11}(\gamma)K_I + a_{12}(\gamma)K_{II} \qquad (25)$$

$$k_{II} = a_{21}(\gamma)K_I + a_{22}(\gamma)K_{II} \qquad (26)$$

Experimental results for crack growth rate da/dN versus the variation in local stress intensity factors Δk_I are plotted in Figure 29 and tabulated in Table 15. Local Δk_I and Δk_{II} were computed for the first 5 mm of crack growth, i.e. 5% of the initial crack length an over which equations (25,26) may be expected to be reasonably valid.

Table 15: Variation in local stress intensity factors for the pupative kinked crack

α	0°	30°	60°	90°
Δk_I	2.81 to 9.67	4.62	3.28	3.16
Δk_{II}	0	0.0243	0.139	0.266

As α increases and mode-II contribution increases, Δk_I decreases while Δk_{II} increases. The local mode-II stress intensity factors are therefore present during initial crack growth but remain negligible compared to the mode-I values.

5.3.2.3 Crack growth rate under pure mode-I loading

Experimental results relating to the crack growth rate da/dN versus the variation in mode-I stress intensity factors ΔK_I are plotted in Figure 29. The results are plotted together with measured da/dN for the mixed-mode tests - when plotted in terms of growth rates along the initial kink paths and calculated Δk_I and Δk_{II}. Crack growth rate varies from 0.00025 mm/cycle to 0.12 mm/cycle. Stress intensity variations range from 5.2 to 9.7 MPa.mm$^{0.5}$. Although results show some scatter, a predominant linear variation of log da/dN with log Δk_I seems to emerge.

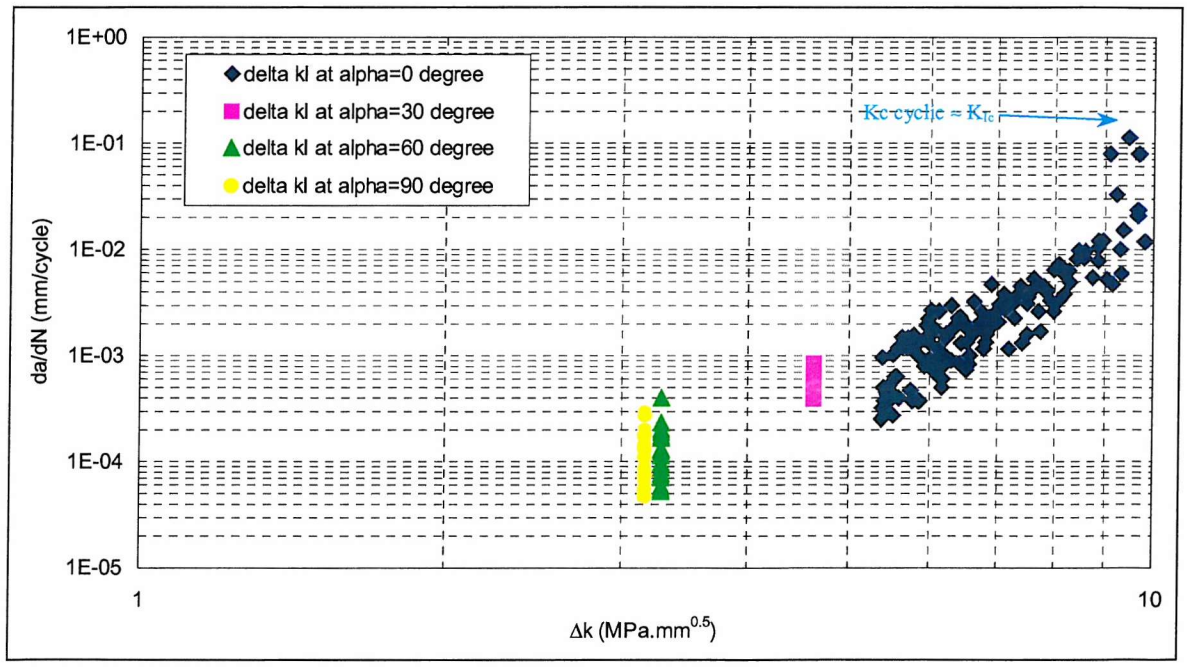

Figure 29: Fatigue growth rate

5.3.3 Microscopic observations on fatigue crack process

For low stress intensity factors, it was observed that cracks propagated by one or several cell diameters through cell wall after repeated flexion of the cell wall in front of the crack tip. Cell wall collapsed plastically after repeated tensile and/or bending deformation, see Figure 30.

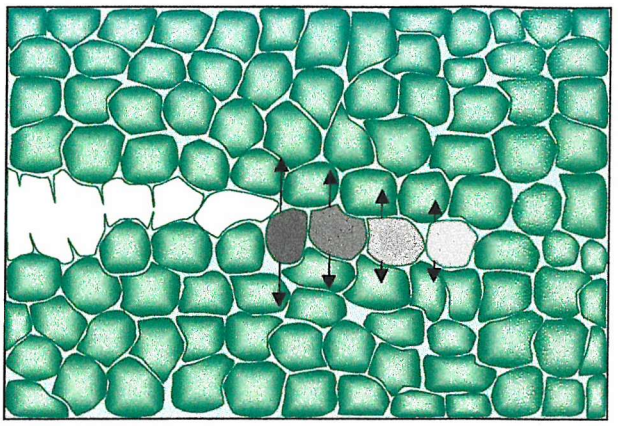

Figure 30: Crack increment at low SIF

For high stress intensity factors, a larger group of the cells located in the vicinity of the crack tip deformed. A large number of cell walls then experienced flexural deformation, see Figure 31.

Additionally, it was observed that a stable crack growth could decrease due to local crack deflection around obstacles, such as thick cell walls, or due to crack-shielding caused by microcracks in the viscinity of the crack tip.

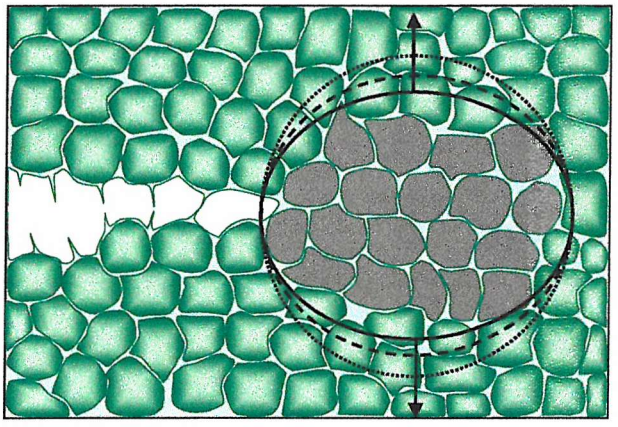

Figure 31: Crack increment at high SIF

5.4 Discussion

5.4.1 Crack paths

5.4.1.1 Initial kinking angle

The experimental results are quite consistent and present little scatter. Fracture criteria predictions for kinking angle γ are presented in Figure 25 together with experimental results. It is seen that all the theories yield good results for β_{eq} values ranging from 65° to 90°. For lower β_{eq} values (below 65°), all the fracture criteria overestimate the fracture angle. Predictions become even higher as β_{eq} gets close to 0, i.e. pure mode-II. Here, if no experimental kinking angle value is available, the maximum hoop stress criterion is the best predictive model oversestimating the fracture angle by 8.5%. This is in accordance with results previously established for this material under static loading conditions [27,91]. The

strain energy density shows, however, poor agreement with experimental results for high mode-II loading contribution, overestimating the fracture angle by about 32%. This is in disagreement with Zenkert findings [27]. Experimentally obtained deflection angles from prior investigation [91] indicate that initial path behaviour for static and fatigue conditions are similar; especially for the low k_{II}/k_I conditions characteristic of growth along the deflected paths.

5.4.1.2 Crack path under mixed-mode or mode-II loading

Under monotonic loading, stable crack propagation takes place relatively quickly with the crack following kinking [91]. Under fatigue loading, crack deviation also occurs at the onset of propagation, but the path is considerably more curved, see Figure 26b. This is consistent with Henn and Richard's findings on the crack path of CTS specimen subjected to cyclic mixed-mode loading. The crack immediately grows in the high k_I direction with a low accompanying k_{II}. The crack deflection angle γ is influenced by the instantaneous mode-I and mode-II loading component.

In terms of the difference in macroscopic path, see Figure 26, under cyclic loading conditions, the onset of stable crack growth occurs at stresses intensity values that are well below the quasi-static fracture toughness. Given the apparent similarity in high β_{eq} path behaviour, for static and cyclic conditions in Figure 26 (i.e. under low k_{II} conditions characteristic of the deflected cracks), the differences in macroscopic paths in static and fatigue loading may be attributed to dynamic effects. The incidence of crack closure along the deflected fatigue crack paths may also be important, with both these issues requiring further investigation.

5.4.1.3 Co-planar growth under pure mode-II loading

The incidence of co-planar growth in the mode-II tests clearly shows the existence of a pure shear growth mode-I this material. The early arrest of shear crack growth is a well-established phenomenon in metallic systems, and is generally attributed to friction force set up in the shear crack wake. The implications of crack wake friction in the present system are not known. However, the present results are consistent with this process being significant.

5.4.2 Crack growth

5.4.2.1 Pure mode-I

The experimental results for mode-I fatigue appear to be moderately scattered. Figure 29 shows a band containing a dense spread of data. A possible explanation for the scatter could follows.

The present material exhibits relatively coarse microstructure. Observations made during the testing and Ashby's cellular foam crack extension model show that the propagation is strongly influenced by the micro-structural features. Crack grows in sudden and rapid bursts and then virtually arrests when barriers such as thick cell boundaries are encountered. The micro-structural cell size effect is most likely to be the source of the scatter in experimental results (it should be noted that the measured crack extensions were always significantly larger than the resolution of the travelling microscope, and, as such, experimental scatter was essentially negligible).

The Paris power law relationship, showing a linear variation of log da/dN with log Δk, is evident over a portion of the total crack growth resistance curve. From Figure 29, the Paris law is established to be:

$$\frac{da}{dN} = 1.77 \cdot 10^{-11} (\Delta K)^{8.026} \qquad (27)$$

At very high ΔK values, the fatigue crack growth rates are higher than those observed in the Paris regime. ΔK increases rapidly and K_{max} approaches the fracture toughness value of the material causing catastrophic failure. Figure 29 shows that fracture occurred at K_{cyclic} approximately equal to 9.7 MPa.mm$^{0.5}$ (or 0.31 MPa.m$^{0.5}$). This value corresponds to a K value that is about 20% higher than the K_{IC} value obtained from static testing, see Table 13, presumably due to the blunting of the crack tip associated with high ΔK increase.

5.4.2.2 Mixed-mode and pure mode-II

Under quasi-static loading, unstable crack growth starts at a critical k value (function of k_I and k_{II} components) and occurs at high speed. This can be predicted using a variety of criteria based on LEFM, see Chapter 4.4.

Under cyclic mixed-mode loading, the instantaneous crack length a(t) is dependent upon the number of load cycles N and the instantaneous stress intensity conditions Δk (function of Δk_I and Δk_{II}). Δk varies continuously with increasing crack length while k_I (t) and k_{II} (t) change as the crack kinks.

The experimental results on mixed-mode fatigue crack growth rate appear to be consistent.

Figure 29 shows that the linear variation of log da/dN with log Δk_I can be extrapolated to the mixed-mode and pure mode-II loading condition. The crack grows in the high k_I direction with a low accompanying k_{II}. Although the crack growth rates are lower (due to lower $P_{fracture}$) than in the pure mode-I case, the trends appear to follow the same k_I-dominated regime.

5.4.3 Microstructural model for the fatigue crack propagation

In earlier studies by Ashby *et al.*[24], a microstructural model for crack propagation proposed a crack extension by one cell diameter through cell wall after repeated flexion of the cell wall in front of the crack tip. Observation supports this model for low stress intensity factors range; cell wall collapses plastically after repeated tensile and/or bending deformation. However, for a highly stressed crack tip, a large group of the cells located in the viscinity of the crack tip deforms. Several cell walls then undergo flexural deformation until the crack advances through the group of cells.

A given number of cycles is required to produce a critical amount of damage, at which time, the crack grows by one step through one or several cell walls. This increment can either be small or large, for a given stress condition at the crack tip, depending on the topology of the cells surrounding the crack. Material distribution in the cell walls is typically highly irregular and is inherent to the poor homogeneity of cellular materials.

The facts above support the conclusion that crack growth is governed by local plastic deformations and local damage accumulation process. A microstructural crack is unlikely to develop at a critical stress but at a critical tensile and/or bending deformation. It is reasonable to suggest a strain-based model – especially in the near-threshold regime where the local microstructure is expected to have a large influence on crack propagation. Crack growth rate could be modelled with volume average local strain, or plastic work done over a given volume, instead of being based on stress intensity factor range ΔK, as in the Paris power law relationship.

5.5 Conclusions

Correlation between growth rates for the various loading conditions tested show that LEFM provides a reasonable description of the material under consideration. The CTS specimen, in association with a special loading device, is an appropriate apparatus for experimental mixed-mode fatigue crack growth analysis. The micro-structural cell size effect can be a source of scatter in the experimental results. The crack tip subjected to mixed-mode cyclic loading immediately deviates and propagates close to the maximum hoop stress direction with a corresponding k_I dominated crack tip condition and a low accompanied k_{II}. A refined model for fatigue and fracture crack advance is described and proposes a simple refinement for high stress intensity conditions at the crack tip. Prediction of crack behaviour based on the maximum hoop stress criterion is reasonably consistent with previous monotonic fracture work. The crack growth regime is accurately modelled by the Paris law. The experimental K_{cyclic} value at fracture extrapolated from fatigue tests is in accordance with mode-I plane strain K_{IC}. Crack growth is governed by local plastic deformations and local

damage accumulation process. For most engineering purposes, fatigue crack growth can be considered to be K_I-controlled. However, the existence of a pure shear growth mode in this material indicates that, under different loading conditions, the K_{II} controlled co-planar crack growth may be significant[93].

6 FLEXURAL FATIGUE AND FRACTURE IN FOAM CORED SANDWICH BEAMS

6.1 Purpose and objectives

So far, only the fatigue and fracture characteristics of the foam material have been discussed. Since rigid foam materials are principally used as core materials, it is important to investigate their behaviour in the sandwich context.

The main purpose of the chapter is to extend the understanding of the flexural fatigue in GRP sandwich foam core beams.

The specific objectives of the investigation are to determine the constitutive phenomena governing the flexural fatigue behaviour of cross-linked PVC foam-cored sandwich structures; to determine the crack growth rates and crack propagation angles; and to propose a model for fatigue crack initiation and propagation in the damage process area for the material under considerations at both macro and microscopic scale.

6.2 Test methods and set up

6.2.1 Materials

The materials used in this investigation were a PVC cross-linked cellular foam, for the core material, and GRP E-glass-epoxy resin, for the faces. The nominal density of the foam used was 130 kg/m^3, referred to as C70.130. A characteristic tensile stress-strain relation and typical properties of the foam materials in tension and shear are shown in Chapter 4. The core, fibre glass and matrix mechanical properties are presented in the Table 16.

Table 16: Typical mechanical properties of the materials.

Component	Name	ρ	t	E_t	$\sigma_{t\ ult.}$	G	$\tau_{ult.}$
		(kg/m^3)	(mm)	(MPa)	(MPa)	(MPa)	(MPa)
fiber	E-glass	2600	-	74000	2200	-	-
matrix	SP-Ampreg-20	1200	-	4500	-	-	-
faces	-	1620	3.85	25400	50	-	-
core	C70.130	130	50	109	3.7	50	2.2

6.2.2 Specimen

The test specimens were cut from a sandwich panel fabricated from the components listed in the previous table. The faces were made of five layers of 600g/m^2 of VETROTEX E-glass (satin of 3) and SP-Ampreg-20 epoxy resin. The volume fraction used was 0.3 and the curing time was 26 hours at 40°C. The specimen was designed such that the intended failure was in shear of the core; it had the dimensions of 550 x 50 x 57.7 mm, see Figure 32. Pads were used at load application and support points in order to avoid skin indentation. The pads were made of Aluminium and had the dimensions of 50x40x5 mm.

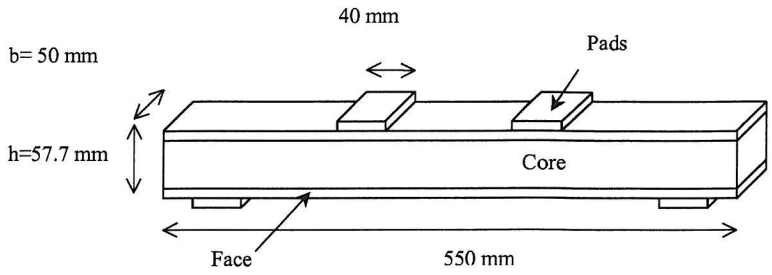

Figure 32: Dimensions of specimen

6.2.3 Test rig and set up

A 4PTB specimen was used for the experiment. The set-up was as shown in Figure 33. A 4PTB loading device was installed in the universal-testing machine, see Figure 34.

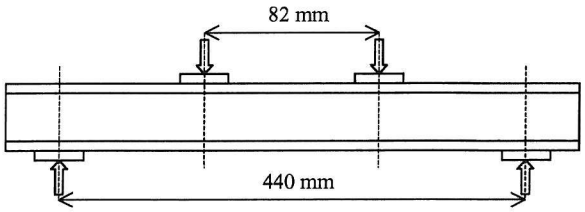

Figure 33: Configuration of 4-point-bending test

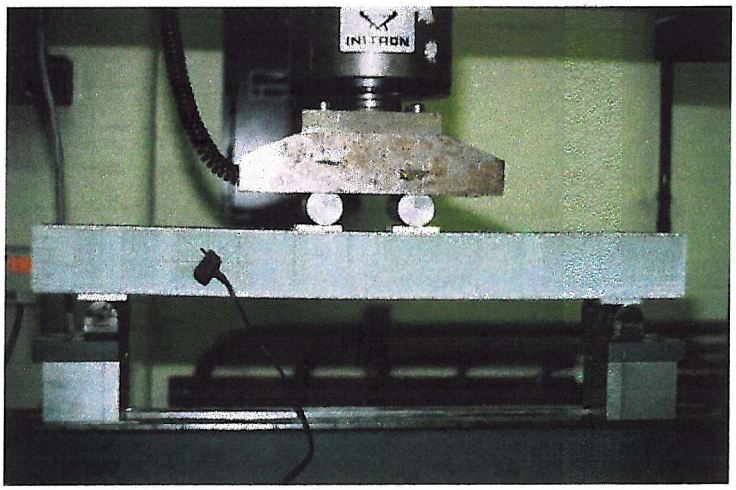

Figure 34: Test apparatus

The static loading tests were displacement-controlled with the same cross-head displacement speed of 1mm/minute. Load and displacements were recorded with a built-in load cell during the whole test. Shear strain was recorded with an extensometer positioned at the centre of the area of maximum shear deformation, and oriented in the direction of the maximum tensile deformation. The accuracy of the extensometer was within 1% of the measured strain. All tests were carried out using an Instron model 8500 universal-testing machine. A total of five specimens were tested in this part of the survey.

For the cyclic loading, 20 specimens were tested using the same 4PTB test set-up. The tests were load-controlled and the test loading frequency was kept between 1 and 3 Hz. The

frequency was determined such that the strain rate would not exceed the value of $10\%s^{-1}$ - in order to avoid any visco-elastic effect due to temperature increase [47,51,52]. Specimens were subjected to constant amplitude sinusoidal load cycles, and at the same load ratio R, equal to 0.1. The specimen loading was started at P_{aean}, the mean value of P_{max} and P_{min} - being the maximum and the minimum cyclic load. Fatigue tests were conducted with varying loads. The maximum cyclic load, P_{max}, was chosen to be 75%, 62.5% and 50% of the ultimate fracture load P_{ult}, which was determined from the static tests. The cyclic load range was thus kept within the linear elastic limit of the material response for the 2 lasts loading cases. Load, deflection and shear strains were recorded continuously using a computerised data acquisition system. Number of cycles to failure was also recorded. For a few tests, crack tip positions were periodically recorded. An optical travelling microscope having a magnification of x20 gave a precise position of the crack tip.

Table 17: Minimum and maximum load level for cyclic fatigue tests

% of P_{ult}	P_{max} (kN)	P_{min} (kN)	τ_{max} (MPa)	τ_{min} (MPa)
75	8.12	0.812	1.52	0.152
62.5	6.77	0.677	1.26	0.126
50	5.42	0.542	1.01	0.101

6.2.4 Standard tests and assumptions

The 4PTB test method was used for the determination of the stiffness of the sandwich beam, and the shear strength and shear modulus of the core, see ASTM *Standard Test Method for Flexural properties of Flat Sandwich Constructions* C393-62 [94].

In the core of a 4PTB sandwich specimen, the stresses are mainly shear stresses between the support and load point, whereas they are mostly axial between the load points. The minimum core shear stress appears at the face-core interface and the maximum in the neutral axis. Further, when assuming a weak core and the faces to be thin, the first order relation can be established as:

$$\tau_{max} = \frac{P}{2bh} \tag{28}$$

$$d = \frac{t_f + t_c}{2} \tag{29}$$

This first order equation (28) is nearly as good as more refined equations for the evaluation of the maximum shear stress in the core. Figure 35 shows the distribution of the core maximum shear stress (light green) in a 4PTB specimen modelled using FE techniques. The maximum value of the core shear stress appears to be constant. In fact, the 4PTB sandwich test does not create a state of constant shear stress between the support and load point, and between the faces. This has been investigated by Burman[47] using FE modelling.

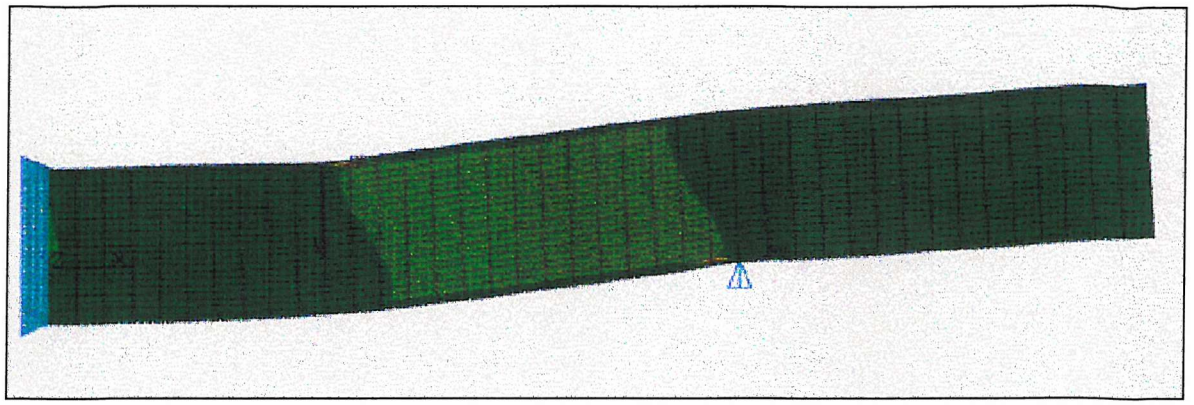

Figure 35: Shear stress distribution in a 4PTB specimen – maximum shear stress (light green)

6.3 Experimental results

6.3.1 Static test results

All the curves showed clearly a non-linear characteristics with large plastic deformations occurring beyond the yield point, but also with an almost straight stress-deflection curve up to the end of the proportional limit, see Figure 37. Specimens failed at different values of strain with rather dissimilar elongation. Stress to failures and stiffness values were rather similar. The mean static fracture load P_{ult} was found to be 11kN, corresponding to a maximum shear stress value of about 2 MPa, see Table 18 and Appendix Figure 76. The upper end of the proportional range was found to be at a shear stress value of about 1.4MPa, see Figure 36.

Table 18: Static test results

Test No.	P_{ult} (kN)	τ_{ult} (MPa)
1	10.46	1.94
2	10.92	2.02
3	11.14	2.07
4	11.30	2.10
5	10.44	1.93
Mean	*10.83*	*2.02*

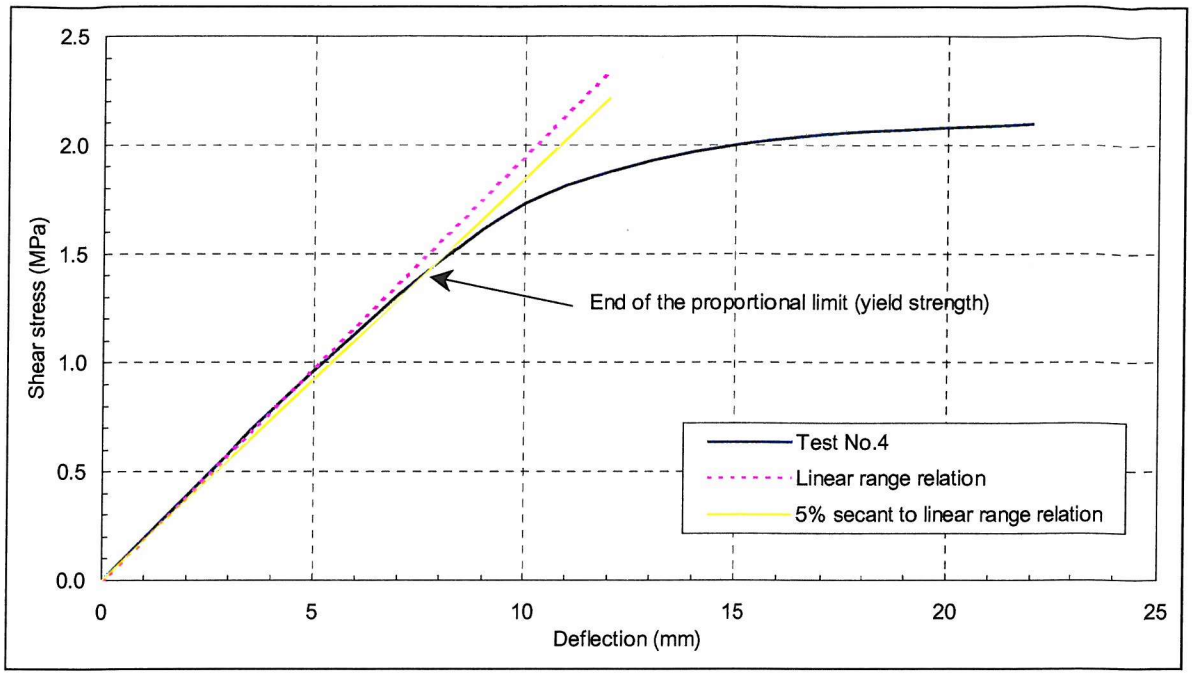

Figure 36 Maximum shear stress vs. deflection curve and yield point determination

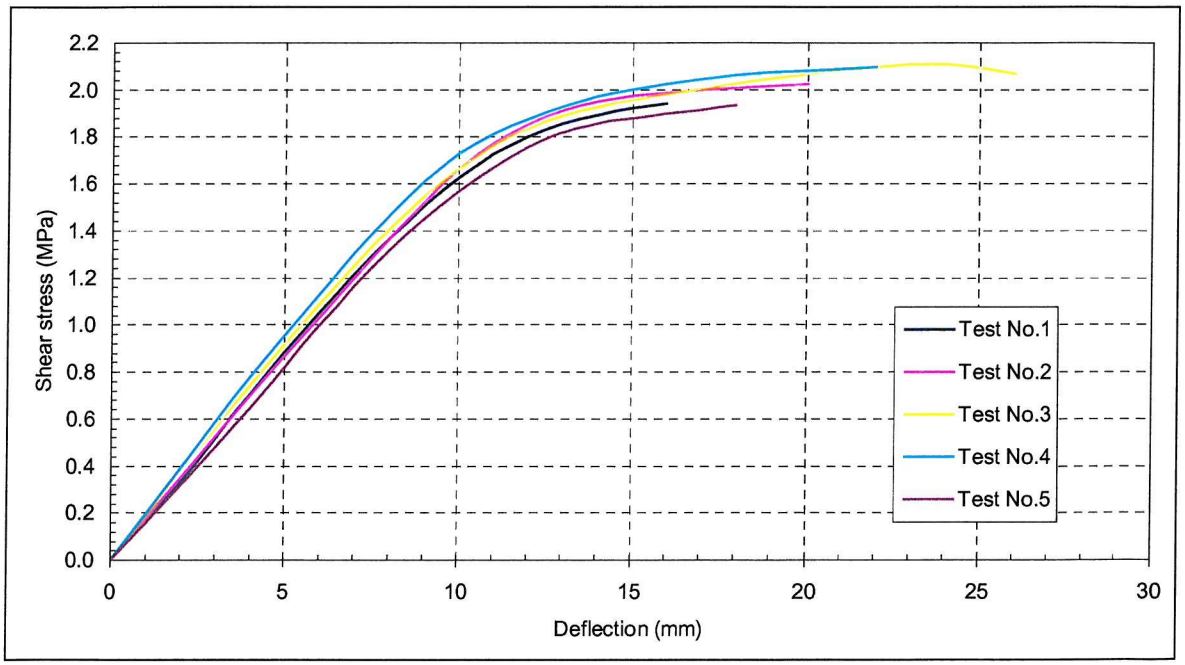

Figure 37: Maximum shear stress vs. deflection curve

The increase in deflection passed the point of non-linearity evidenced a large reduction in stiffness. This is illustrated in Figure 38 where stiffness is plotted as function of the shear stress. In this context, the stiffness is taken as the ratio of the maximum shear force to the corresponding deflection value.

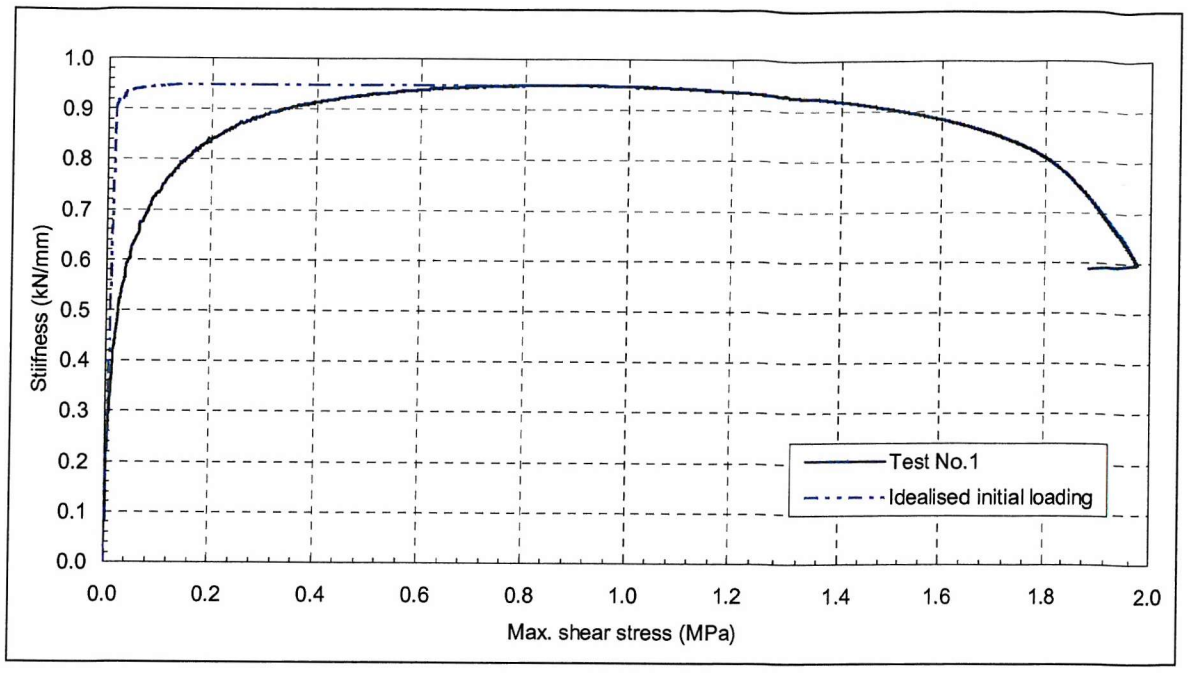

Figure 38: Stiffness vs. maximum shear stress curve

All the tests showed clear ductile behaviour of the core material. The failure mode observed for the five specimen was abrupt core shearing. The fracture was located between the support and load point. The crack angle was oriented at approximately 45° relative to the neutral axis of the beams – and corresponding to the direction of maximum principal stress. The specimens did not show any sign of important damage at the point loads, see Figure 39

Figure 39: Catastrophic core shear failure

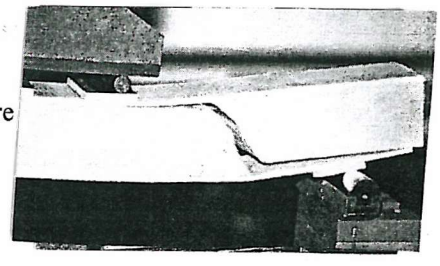

6.3.2 Fatigue Test Results

6.3.2.1 Load-deformation history

Material degradation due to cyclic fatigue loading can be represented graphically in stress-strain loops. Under load-controlled testing conditions, cyclic softening or hardening occurs concurrently with an increase or decrease of the strain amplitude.

The first set of results examines the maximum displacement of the actuator cross-head. The second set looks over the shear strain deformation (measured with an extensometer) in the core before the crack formed.

6.3.2.1.1 Load vs. cross-head displacement

The load-deflection curves for the 3 loading levels under considerations are shown in Figure 40, Figure 41 and Figure 42. All parallel specimens indicated a similar behaviour and a reasonably linear load response for their whole life.

The higher load level was set to P_{max} equal to 75% of P_{ult}; the core maximum shear stress τ_{max} pertained to the non-linear regime of the material response. For this load level, the load deflection curve was linear at cycle number 1, apart from a moderate hysteresis effects. The curved moved to higher deflections and more pronounced hysteresis, maintained its linear character with increasing cycle number - between cycle number 1000 and 3000. Slope, though, decreased significantly. A marked hysteresis occurred just prior to final failure at cycle number 3250. Deflections in the last few cycles did not get recorded but the significance on tests results were negligible.

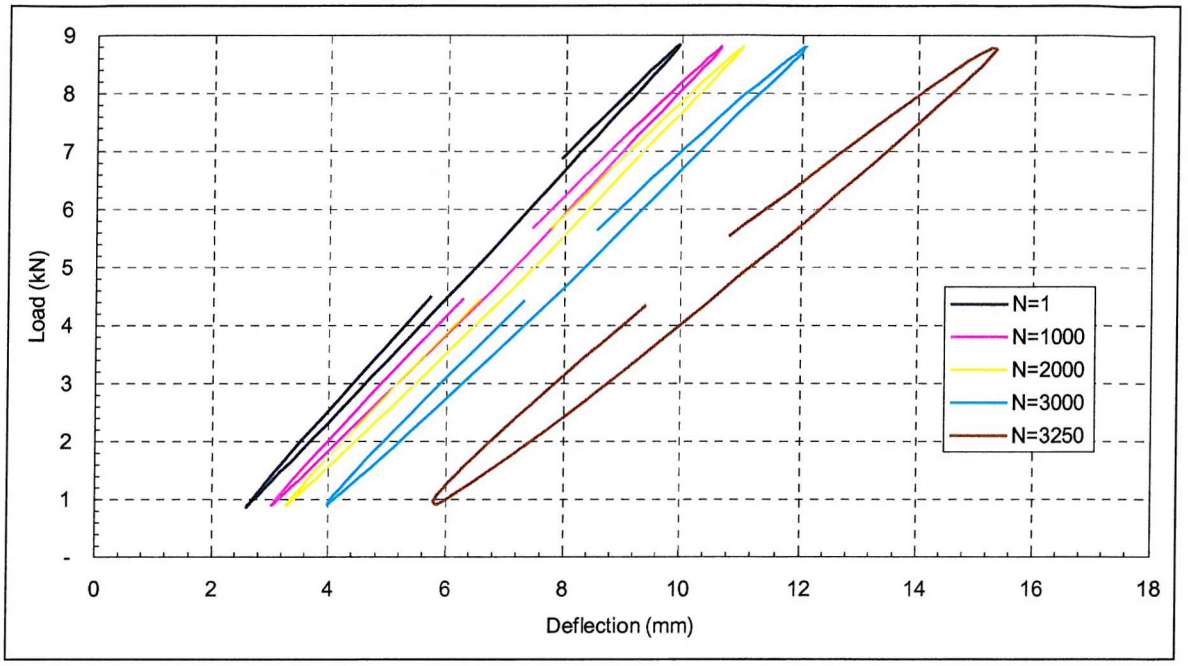

Figure 40: Deflection vs. number of cycles for 75% P_{ult} – Failure at N=3273

For the second load level, i.e. 62.5% of P_{ult} and τ_{max} linear, the load deflection curve was linear for the entire specimen life, accompanied with very moderate hysteresis effects and a moderately decreasing slope. The curve moved to higher deflections with increasing cycle number over the specimen life. Moderate hysteresis effects were present. Here also, deflections in the last few cycles did not get recorded.

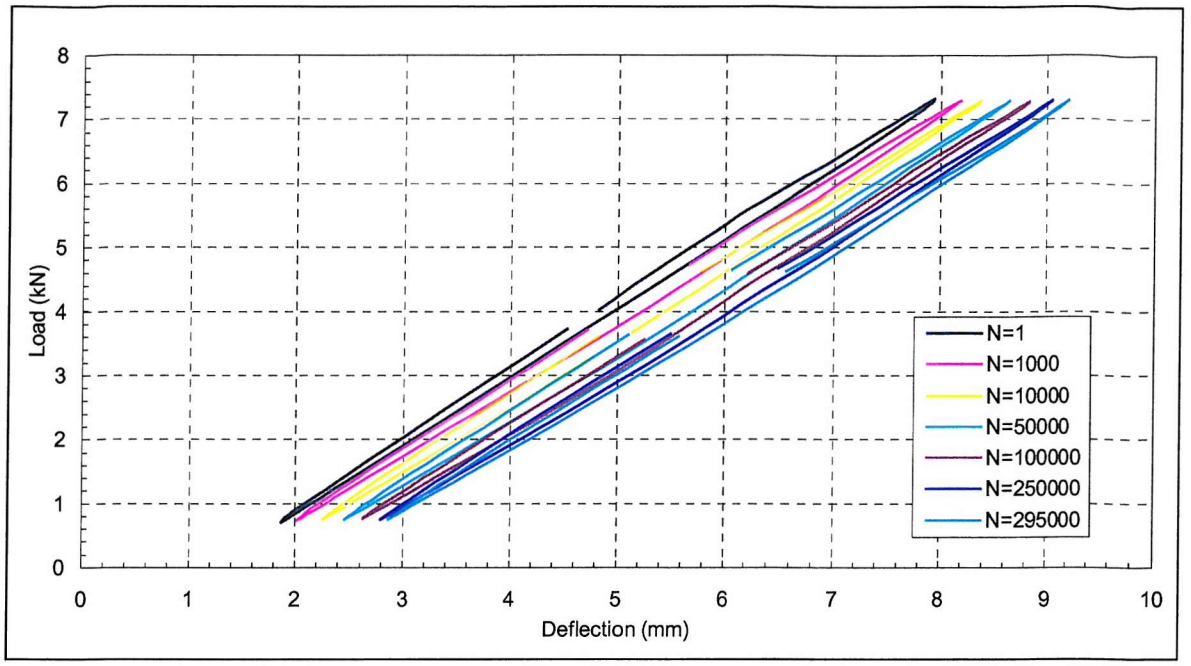

Figure 41: Deflection vs. number of cycles for 62.5% P_{ult} – Failure at N=296869

For the final load level equivalent to 50% of P_{ult}, the load deflection curve was linear for the entire specimen life, accompanied with a minor hysteresis effect and a moderately decreasing slope. The curve moved to higher deflections with increasing cycle number over the specimen life. No pronounced hysteresis effect was present. Deflections in the last few cycles did not get recorded.

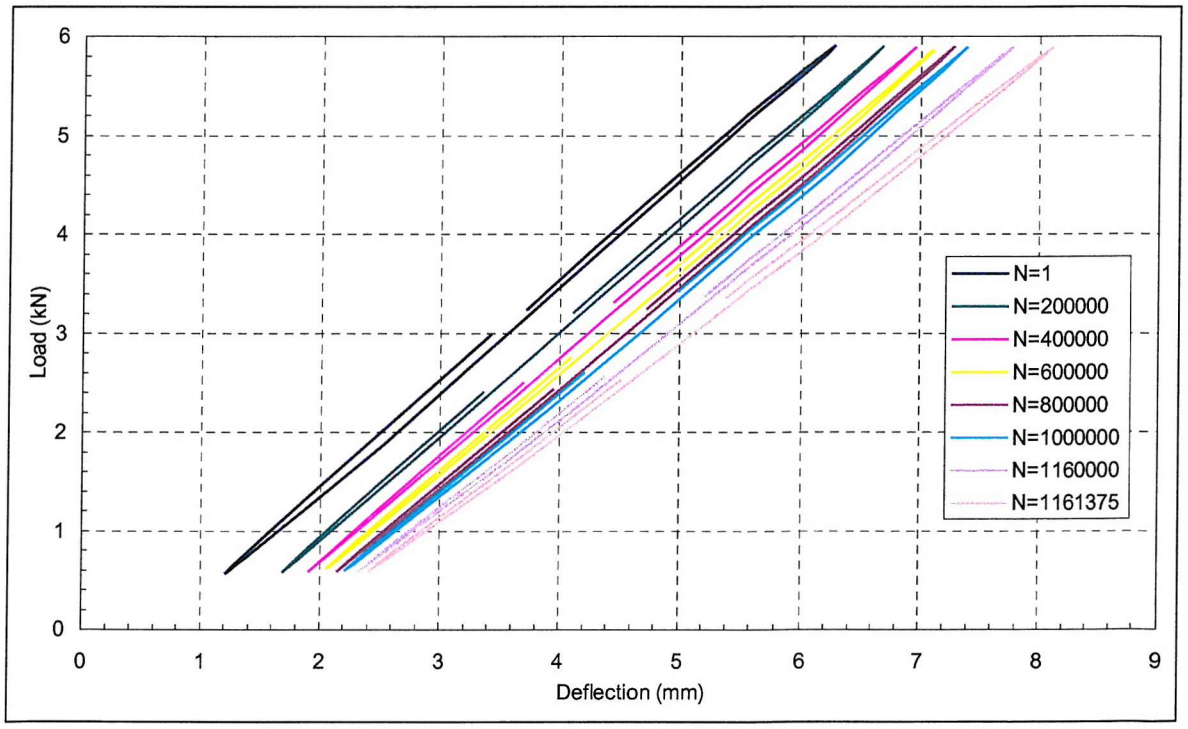

Figure 42: Deflection vs. number of cycles for 50% P_{ult} – Failure at N=1161375

6.3.2.1.2 Load vs. strain

The load-microstrain curves for the 3 loading levels under considerations are shown in Figure 43, Figure 44 and Figure 45.

For P_{max}=75%P_{ult}, the tensile strain increased significantly during the entire fatigue life, whereas stiffness decreased moderately, characteristic of cyclic softening. Further, a pronounced hysteresis occurred just prior to failure. The sandwich structure behaved in a linear fashion for all its lifetime.

Shear deformation in the core did not get properly recorded in the last cycles because of the crack opening located between the extensometer's arms, see Figure 47. The significance of the discrepancies on this part of the tests results was, however, negligible.

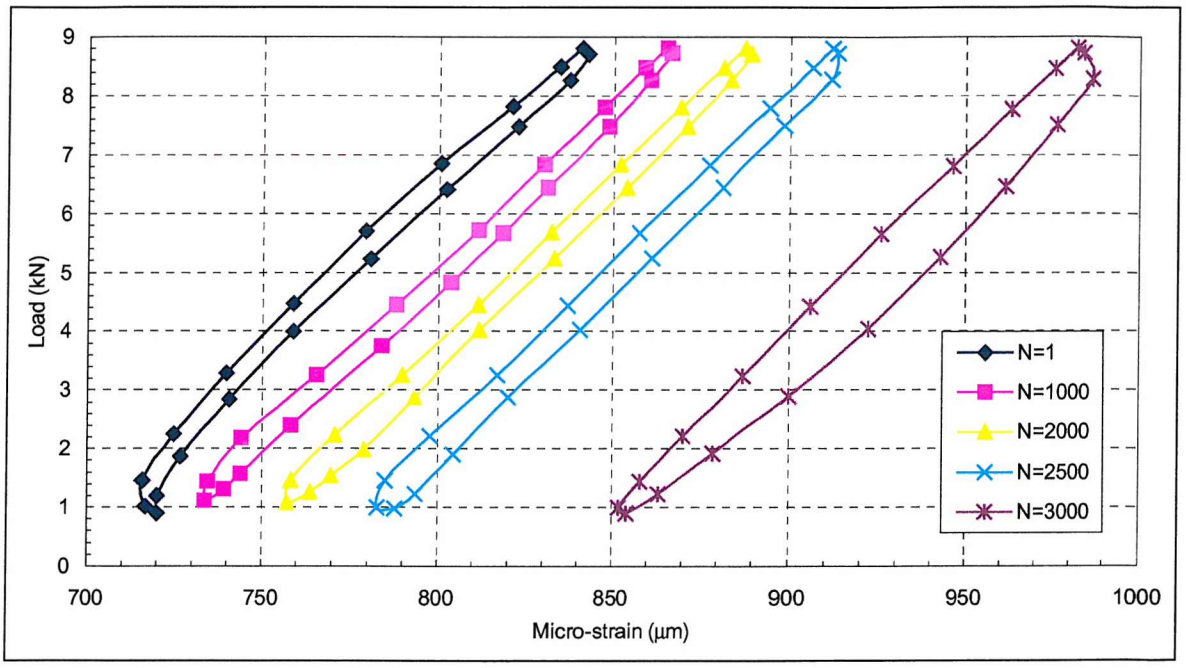

Figure 43: Load vs. microstrain for 75% P_{ult} – Failure at N=3273

For P_{max}=62.5%P_{ult}, the strain increased significantly during the entire fatigue life, whereas stiffness decreased just before failure. Further, no pronounced hysteresis of the specimen occurred. The sandwich structure behaved in a linear fashion until shortly before failure.

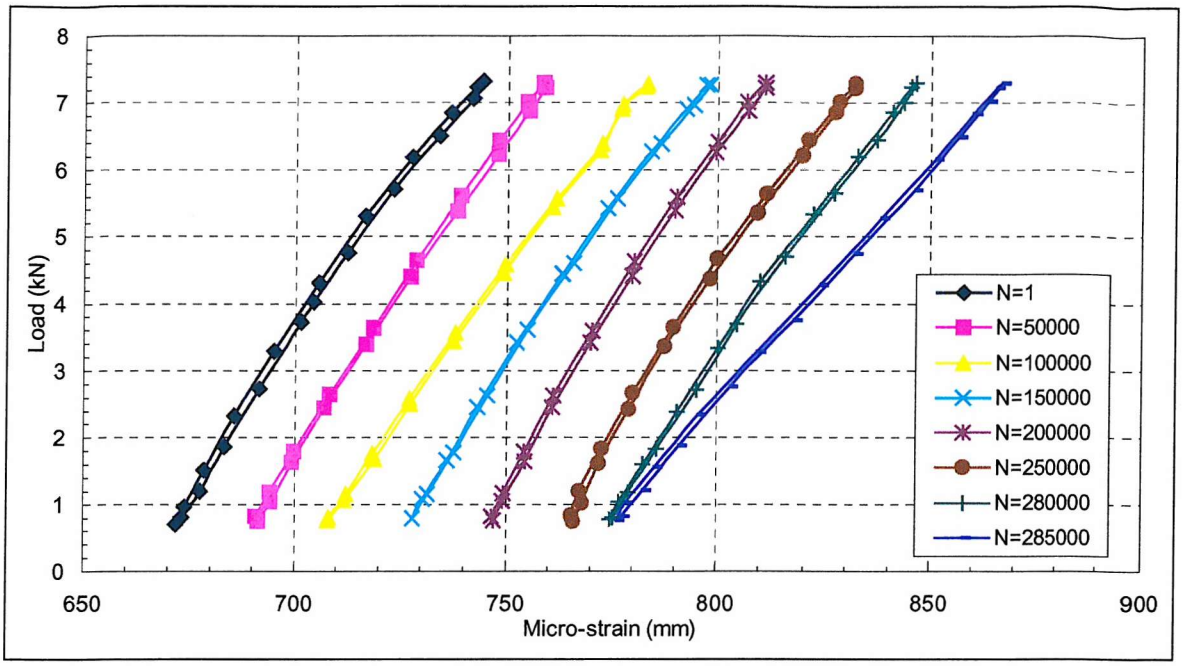

Figure 44: Load vs. microstrain for 62.5% P_{ult} – Failure at N=296869

For P_{max}=50%P_{ult}, the strain increased significantly during the entire fatigue life, whereas stiffness decreased just before failure, characteristic of cyclic softening. Further, a moderate hysteresis of the specimen occurred. Just prior to failure, a marked hysteresis took place. The sandwich structure behaved in a linear fashion until shortly before failure.

Load-deformation history for both strain and cross-head displacement appeared to be related and shows identical trends irrespective of stress level.

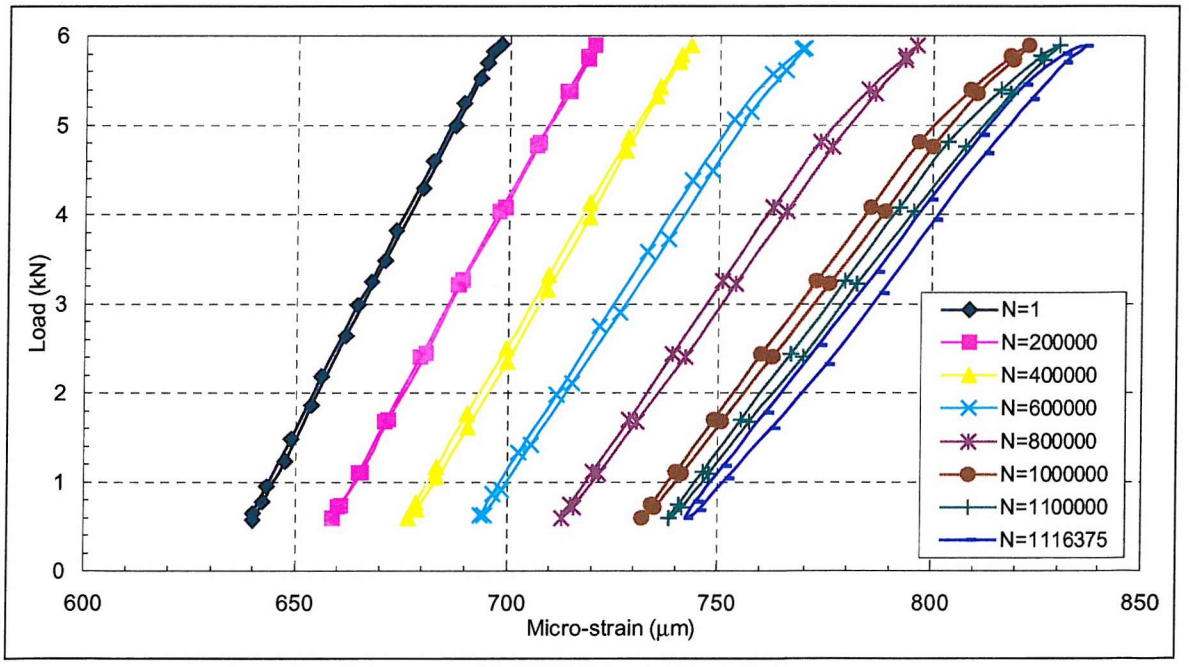

Figure 45: Load vs. microstrain for 50% P_{ult} – Failure at N=1161375

6.3.2.2 *Deflection history*

Fatigue deflection behaviour of a specimen can be characterised as the variation of specimen deflection during the fatigue life. Maximum deflection vs. a function of cycle number plots are used to represent the fatigue deflection behaviour. Maximum and minimum displacement history were identical until shortly before failure. The change of maximum deflection with number of cycles at 3 loading levels is illustrated in Figure 46.

Test results showed that the increase in deflection over fatigue life was stress-dependent: the higher the stress, the higher the deflection at a given cycle number. Deflection increased moderately as cycle number increases over almost the entire fatigue life. Close to the point of failure, deflection then increased very rapidly. For the higher load level, i.e. 75%, the increase in deflection was significantly higher than that of the 2 other load levels over a given cycle range. All equivalent specimens showed a similar behaviour.

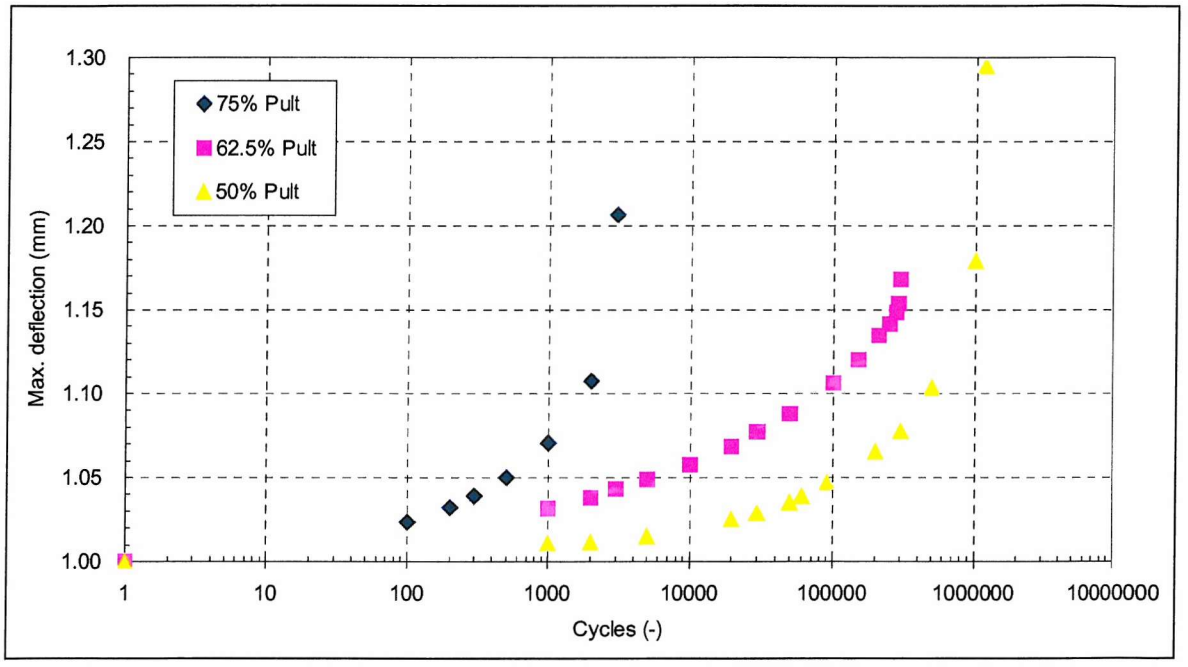

Figure 46: Max. deflection vs. number of cycles

6.3.2.3 *Crack growth rates*

Crack length was measured for visible cracks just before final failure. Experimental results for crack length, number of load cycles and crack growth rates are presented in Table 19 and Table 20 for single-shear-cracked specimens. No crack length measurements were recorded for tests carried at 50% P_{ult} and for multiple cracks.

At the end of the fatigue test, the crack growth rate values were of the same order life, independent of the load level. The crack growth rates significantly increased over the end of the fatigue life until final failure occurred.

Table 19: Crack growth rates for test no.3 - for 75% P_{ult}

N	dN	Δa	da/dN
(-)	(-)	(mm)	(mm/cycle)
2205	120	1	0.00833
2325	120	1.1	0.00917
2505	120	1.2	0.01000
2745	180	1.9	0.01056
3005	240	2.7	0.01125
3273	260	3.2	0.01231

Table 20: Crack growth rates for test no.1 - for 62.5% P_{ult}

N	dN	Δa	da/dN
(-)	(-)	(mm)	(mm/cycle)
296009	120	0.7284	0.00607
296129	120	0.8748	0.00729
296249	120	1.0788	0.00899
296369	120	1.1388	0.00949
296489	120	1.2492	0.01041
296609	120	1.4	0.0118

6.3.3 Observations of the damage process zone

6.3.3.1 Full scale observations

All specimens failed by core shearing in the zone of highest stresses situated between the support and load application point, see Figure 47. No changes could be observed on the specimens sides for most of the fatigue life, but just before ultimate failure. Crack initiation could only be observed visually at the end of the fatigue life. Table 21 shows the earliest possible time of visual detection of cracks from the time of ultimate failure (expressed as a percentage of the specimen life).

Table 21: Earliest possible time of visual detection of crack

P_{max}	Earliest Possible Time
75%	>10%
62.5%	>5%
50%	>3%

6.3.3.1.1 Fracture process zone

The final fracture took place at the end of the fatigue life as a result of repeated large shear deformations due to shear yielding. The fractures were either a single shear crack or multiple shear cracks; about half of the fractures were single shear crack, and half were multiple shear cracks, irrespective of the load level, see Figure 48. Examination of the core on multiple-cracked specimens indicated a "plastic" or permanent deformation near the centreline.

6.3.3.1.2 Damage formation and growth

Observations indicated two steps: a first step where microshearing occurred; and a second step where macroscopic shearing took place.

Soon before failure, signs of shear deformations became visible along the centreline of the fracture process zone. The deformation magnitude increased rapidly, and preceded the initiation of one or several shear microcracks aligned horizontally along the centreline, see Figure 49. A single cracks then formed before any sign of gross cyclic damage. Or alternatively, multiple cracks grew from a population of micro-defects after flagrant yielding along the centreline of the fracture process zone.

For both single and multiple cracks, cracks continuously grew away from the centreline towards the faces. The crack growth direction was measured to be on average about 60 degrees from the centreline, irrespective of the load level. As crack tips got closer to the faces with cycles numbers, the large plastic shear deformations occurring along the centreline deformed the middle part of the crack. This resulted in a Z- or S-shaped crack. The damage formation and growth was very short with respect to fatigue life.

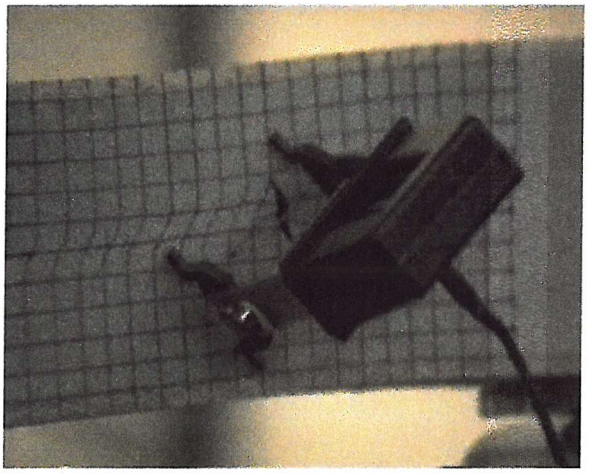

Figure 47: Single shear crack growth

Figure 48: Multiple shear crack growth and microcracks

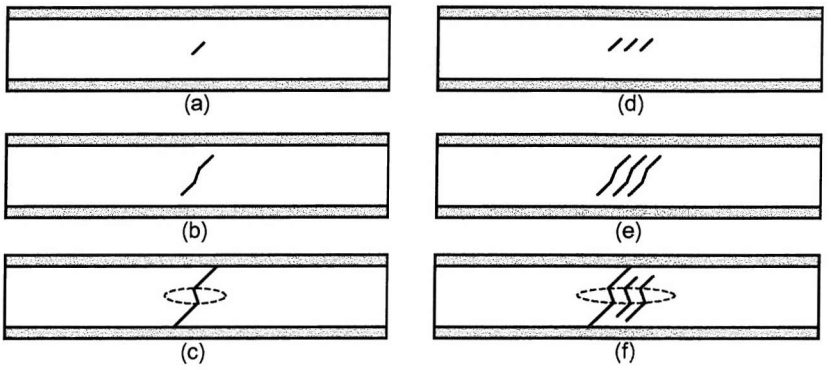

Figure 49: (a-c) single microcrack growing to a single final crack. (d-f) multiple microcracks growing and leading to a single final crack – (c&f) damage process zone exhibiting large core shear yielding and S-shaped crack(s)

6.3.3.2 Microscopic observations on fatigue specimen

Small samples of core material were cut from a few specimens, belonging or adjacent to the damage process zone. The cuts were made in the longitudinal-vertical plane, i.e. the plane showed in Figure 47. These were examined under an optical microscope under various magnifications. The failed specimens were compared against the virgin foam material. Other samples, cut from specimens stopped shortly before any visible crack became apparent - or before any pronounced shear deformation had set in - were also examined.

Samples cut from single-shear-fractured specimens showed no noticeable difference to virgin specimens, see Figure 50 and Figure 51.

Samples cut from multiple-shear-fractured specimens showed a marked difference. In Figure 52, Figure 53 and Figure 54, the fracture process zone exhibited clear shear yielding. The cell walls had re-aligned themselves along the principal tensile stress direction.

Samples cut from stopped specimens showed no noticeable cell structure difference. In Figure 54, the material from the fracture process zone showed already cell wall re-alignment and decohesion (plastic collapse) of the cells with each other. For the C70.130 foam, the typical cell size ranges from 0.2 mm to 0.4 mm.

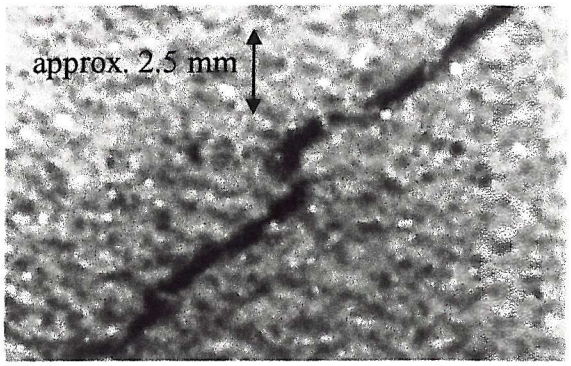

Figure 50: Single shear crack – macroscopic view

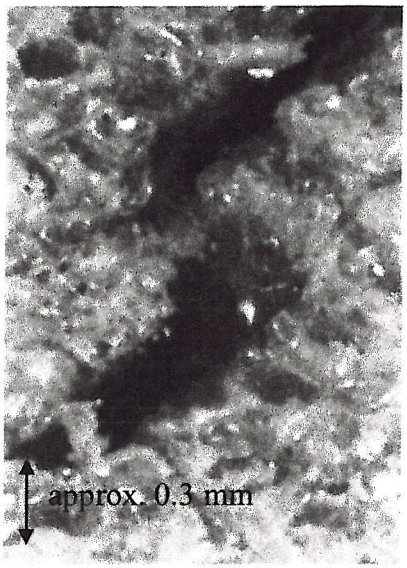

Figure 51: Single shear crack – microscopic view

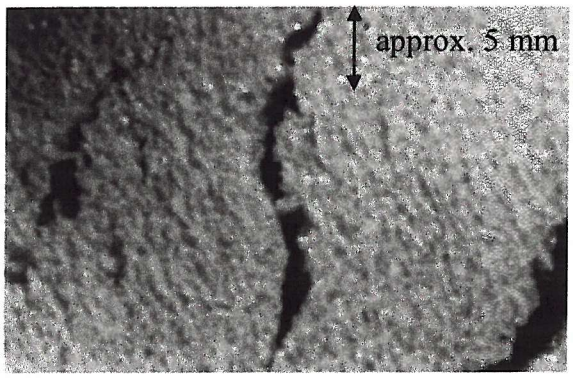

Figure 52: Multiple shear cracks, fracture process zone and core shear yielding

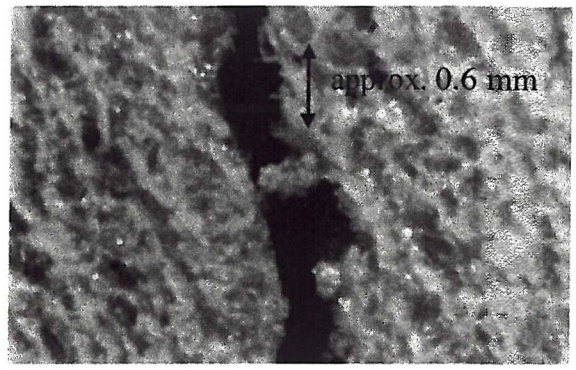

Figure 53: One of the multiple shear cracks and cell wall re-alignment

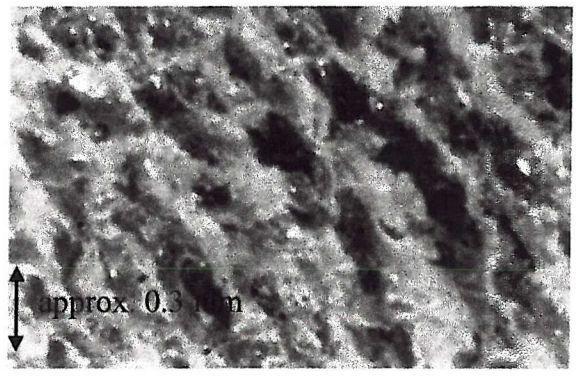

Figure 54: Material from the fracture process zone – cell wall re-alignment and decohesion of the cells

6.4 Discussion

6.4.1 Fatigue life

An S-N curve is presented in the Appendix, Figure 78. For maximum shear stresses beyond the linear limit, fatigue lives of a few thousand cycles were reached, whereas, for maximum shear stresses below the linear limit, fatigue lives lasted for much longer. The results are in accordance with the findings presented by Clark[95]. Fatigue life values are moderately higher but fatigue life threshold appear to tend to the same limit. The source of discrepancies is possibly due to test set-up differences, i.e. 4PTB vs. 10-point bending, and variations in shear strength between the batches.

6.4.2 Creep effects and stiffness degradation

Experimental results show that the cyclic fatigue life of the specimen have two different regimes: a first regime where residual shear distortion dominates; and a second regime, much sorter, where fast and significant shear stiffness degradation takes place.

The variation of stiffness with respect to fatigue life is important over most of the fatigue life for low cycle fatigue - with maximum stress level pertaining to the non-linear range. In contrast, for high cycle fatigue, the stiffness remains quasi constant over most of the fatigue life. Stiffness only begins to degrade just before final failure, see Figure 55. This results are

consistent with the observations of the large core shear deformations made on the side of the specimens; they are also consistent with the increase in hysteresis. Large core shear yielding induced the accumulation of damage in the damage process zone, causing subsequently the stiffness to decrease and the hysteresis to increase. This is in agreement with stiffness degradation for medium and high cycle fatigue presented in earlier work[42-45].

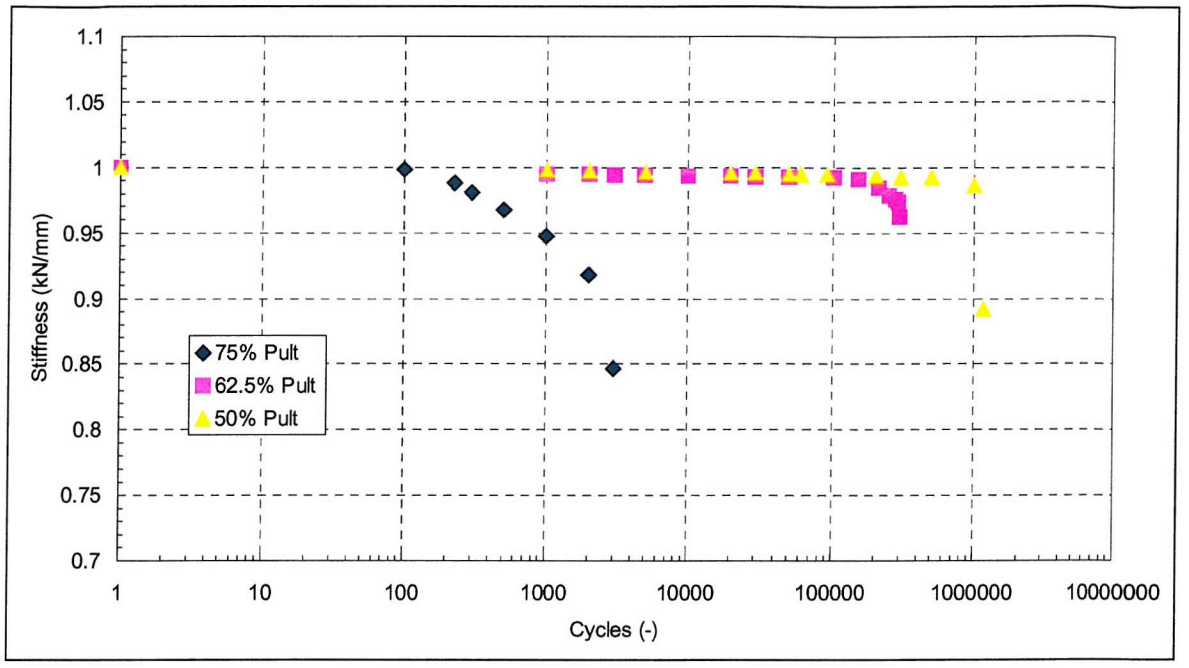

Figure 55: Variation of stiffness vs. number of cycles

The variation of deflection is continuous over the almost entire fatigue life. Both maximum and minimum deflections increase in a similar fashion until large shear crack(s) have formed in the damage process zone, see Figure 56. The behaviour is in agreement with earlier work[43,45]. The deflection increase is believed to be due to creep effects. Results showing constant stiffness and hysteresis during most of the fatigue life are in agreement with the observations made on the specimen sides during testing. To further correlate the creep effects occurring under static and cyclic loading conditions, additional analyses and tests are necessary.

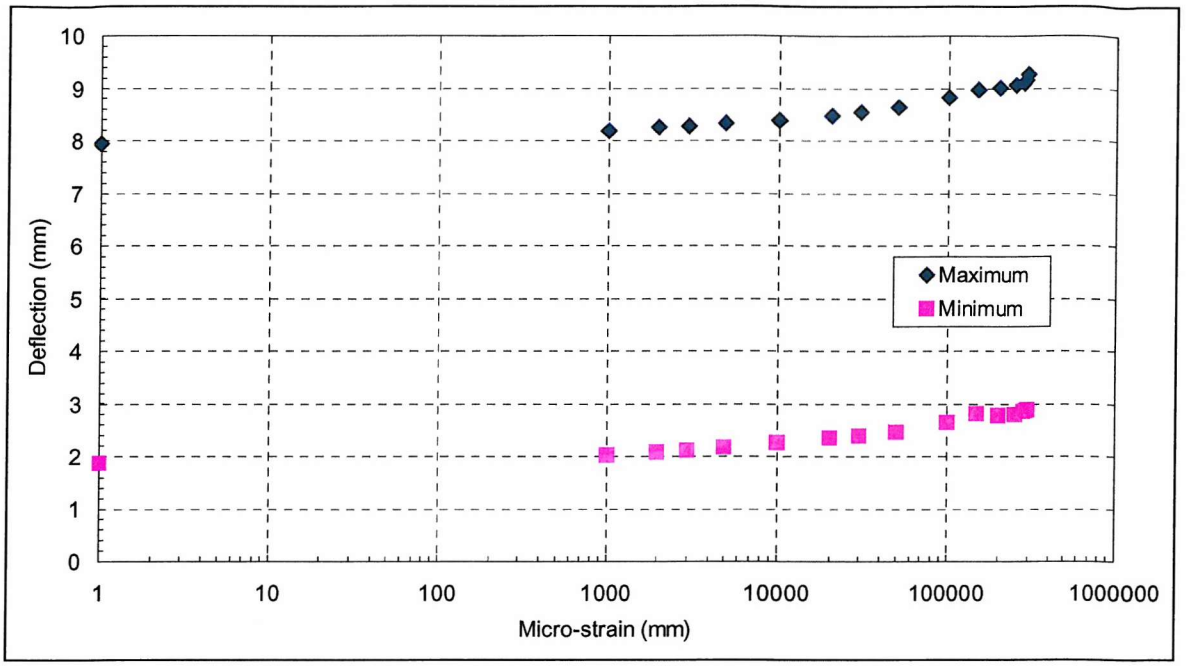

Figure 56: Variation of maximum and minimum deflections with number of cycles

6.4.3 Damage formation, crack initiation and growth

At the end of the fatigue life, core shear yielding sets in the core and increases with cycle numbers; deformations in the damage process zone then become more intense. Larger strains induce plastic bending, yielding and crack-nucleation at weak cell walls, or at pre-existing flaws. The decohesion between the cells then intensifies. This results in rotating the cell walls towards the direction of maximum principal stress, tensile stress in this context. This is in clear agreement with the behaviour presented in Gibson and Ashby[21].

Observations show that the damage process zone is located along the middle plane of the core. The damage process zone is expected to be located at the centre as the maximum shear stress is suppose to occur at the centre. This is supported by previous FE analyses[44] showing maximum shear stresses occurring near the centreline. A second reason for the location of the damage process zone is the variation of the core density. The density varies moderately across the thickness with a minimum value in the middle plane - this is believed to be due to the manufacturing process.

As microcracks density increases and the cell lattice breaks down, flaw lengths become critical. A few of the larger cracks become prevalent and start propagating. Finally, one will grow to the facings faster than the others and will induce the ultimate failure. The cracks become visible just before the end of the fatigue life. In a multiple crack case, no single larger flaw is present and no crack is initiated. The damage process zone undergoes the same deformation for a little longer period; crack onset is delayed. Finally, the multiple cracks initiate in the larger flaws along the centreline and begin to propagate. The fracture

process can be described as ductile. The damage formation and growth of single crack, though, are different. Here, the fracture is more brittle. In the single crack case, a single larger flaw becomes dominant and starts growing. This occurs before any important core shear yielding sets in. The crack deforms, absorbs most of the energy, and thereby reduces the stresses in the rest of the damage process zone. The crack becomes visible a little earlier than in the case of the multiple cracks.

6.4.4 Crack growth rates correlation

For 4PTB single-shear-cracked specimens, crack growth rates da/dN_{4PTB} are presented in Table 19 and Table 20. The values range from 0.006 to 0.012 mm/cycle near the end of the fatigue life, constantly increasing until final failure.

Crack growth rates under mode-I, mode-II and mixed-mode loading conditions were determined using the CTS specimen, see Chapter 5. da/dN_{CTS} were found to vary from 0.00025 mm/cycle to 0.12 mm/cycle. Under mode-II loading, mode-II da/dN_{CTS} were found to be of the order of 10^{-4} mm/cycle, whereas mode-I da/dN_{CTS} were higher: up to about 10^{-2} mm/cycle before final fracture. This was due to crack growth in the k_I direction with a low accompanying k_{II}.

The mode-I crack propagation rates, obtained for both CTS and 4PTB specimen under mode-II loading, are of the same order towards the end of the fatigue life. The final crack propagation rates are of the order of 10^{-2} mm/cycle. Fatigue crack growth in a 4PTB foam cored sandwich beams can be considered to be K_I-controlled. Further observation on initial crack propagation angle supports this explanation.

6.4.5 Fatigue crack propagation angle

For both single and multiple cracks, the fatigue crack propagation angle is measured to run at about 63° relative to the neutral axis of the beam. The value differs from the static propagation angle, i.e. 45°. The fatigue crack propagation angle is correlated by the findings presented in Chapter 5 for cracked CTS foam specimen. Under pure mode-II fatigue loading, initial crack propagation angle was found to be equal to approximately 65°.

6.5 Conclusions

From the results and the discussion, one can draw several conclusions. The 4PTB specimen is an appropriate apparatus for experimental flexural fatigue characterisation. Experimentally obtained S-N curves have shown good accuracy and compare well with independent results. The flexural fatigue is characterised by 2 regimes: a creep regime inducing small permanent deformation followed by fatigue and fracture regime, typically much shorter, responsible for a catastrophic shear stiffness degradation. For medium and

high cycle fatigue, the dominant phenomenon is creep until just prior to failure. For low cycle fatigue, crack initiation and growth are the dominant phenomenons. It is during the creep regime that damage formation first occurs along the core centreline. After a phase of intensification of shear deformations and cell decohesion, crack initiation sets in causing one of several microcracks to appear. Finally, crack grows to the facings inducing the ultimate failure. The damage formation and growth of multiple cracks appears more ductile as cracks propagate in more damaged material than that of single shear crack. Correlation for between structure and material response over the fatigue life have been established. Mode-I crack propagation rates, da/dN_{4PTB}, are of the magnitude, 10^{-2} mm/cycle, towards the end of the fatigue life. Crack growth rates obtained for CTS and 4PTB specimens support each other. Fatigue crack growth in a 4PTB foam cored sandwich beam can be considered to be K_I-controlled. The failure process model is supported by the fatigue crack propagation angle, i.e. 63°, characteristic of mode-I propagation under mode-II loading conditions; this is correlated by results from Chapter 5.

7 NUMERICAL ANALYSIS OF SHEAR CRACK IN FOAM CORE SANDWICH BEAMS

7.1 Purpose and objectives

Chapter 6 discussed the flexural fatigue in FRP sandwich beams through experimental investigations using the 4PTB test specimen. The investigation presented in this chapter seeks to extend the understanding of the fracture behaviour and to map the fracture parameters for shear cracks in foam core sandwich beams through numerical studies of the same 4PTB test specimen .

The main objectives of the study are to determine strain energy release rate G and stress intensity factors K_I and K_{II} for a range of physical and mechanical properties that are characteristic of a typical sandwich beam. The second goal is to study the relationship between the stress intensity factors. A practical objective is to predict the failure load of a cracked sandwich beam by correlating results from experimentally-determined fracture envelop and stress intensity factors calculated numerically. A final objective is to establish a correlation between stress intensity factors calculated numerically and stress intensity factors at fracture under mixed-mode conditions derived from experiments.

7.2 Finite element model

Model description

A 4PTB test specimen was chosen to be modelled, illustrated in Figure 57. The model had the dimensions of 550 x 35 x 34 mm, see Figure 58. The specimen was modelled using about 2000 eight node quadratic collapsed rectangular and triangular elements under plane strain conditions. The mesh was refined around the two crack tips; 200 collapsed triangular elements of edge length down to 0.1 mm were used, see Figure 59. The mesh was refined several times until convergence of the fracture parameters. Results were also compared with independent results[26]. Around the crack tip 16 quadratic elements with quarter point location, displaying a $1/r^{0.5}$ stress field singularity, were used, see Figure 60 and Figure 61. A half model was used due to the symmetry of the four-point-bending configuration. The crack length ratio, a/w, was varied between 0.45 and 0.55. The method used to calculate the stress intensity factors was a simple displacement extrapolation method; this was performed automatically in ANSYS postprocessor using the LPATH and KCALC commands. The calculations were performed with a multi-purpose FE program, ANSYS 5.3, 5.4 and 5.5, running on SUN station.

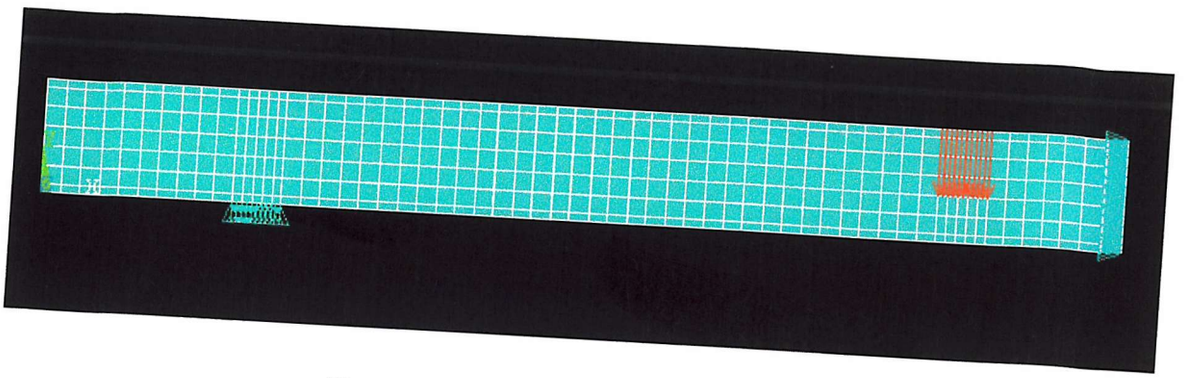

Figure 57: FE model of a 4PTB beam specimen

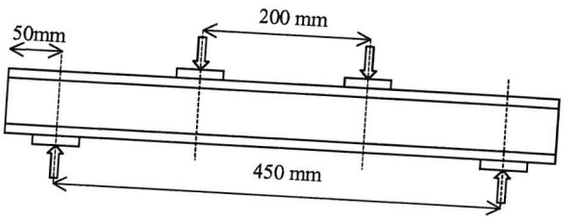

Figure 58: dimensions of the 4PTB finite element FE model

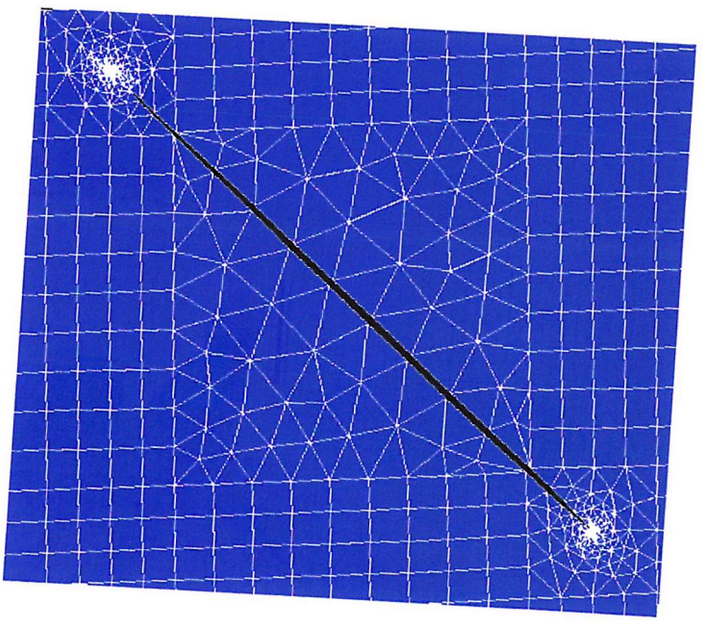

Figure 59: Local mesh refinement near the 2 crack tips

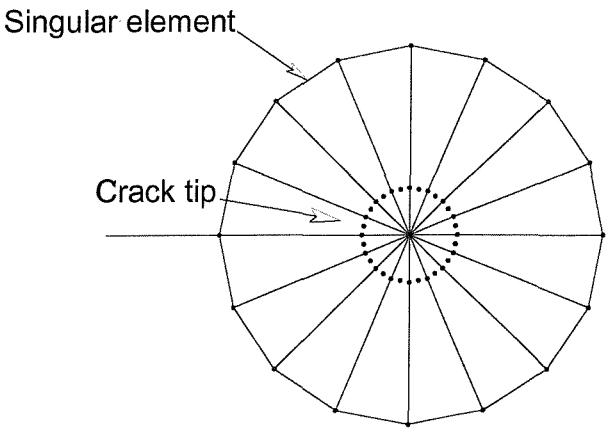

Figure 60: 16 triangular singular elements centred on the crack tip

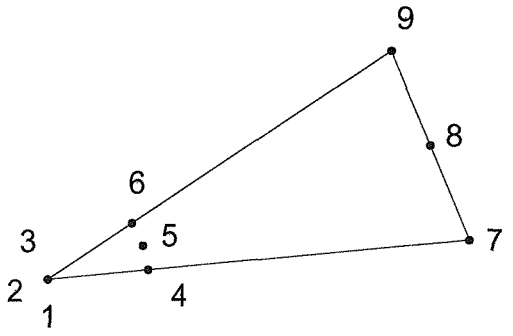

Figure 61: A quadratic collapsed triangular element

Stress intensity factor computation

The calculation method used is based on displacement extrapolation technique. It involves correlation of the elements displacements and tractions with the theoretical values.

The displacement fields on the crack surface can be written as:

$$u_2(\theta=\pi)-u_2(\theta=-\pi)=\frac{\kappa+1}{\mu}.K_I.\sqrt{\frac{r}{2\pi}} \tag{30}$$

$$u_1(\theta=\pi)-u_1(\theta=-\pi)=\frac{\kappa+1}{\mu}.K_{II}.\sqrt{\frac{r}{2\pi}} \tag{31}$$

and the tractions ahead of the crack along θ=0 as:

$$t_1=(\sigma_{11}.n_1+\sigma_{12}.n_2)=\frac{1}{\sqrt{2\pi r}}.(K_I.n_1+K_{II}.n_2) \tag{32}$$

$$t_2=(\sigma_{12}.n_1+\sigma_{22}.n_2)=\frac{1}{\sqrt{2\pi r}}.(K_{II}.n_1+K_I.n_2) \tag{33}$$

If considering 2 points, B and C with r=l/2, see Figure 62,the stress intensity factor can be found from:

$$K_I^{BC} = \frac{2\mu}{\kappa+1}\sqrt{\frac{\pi}{l}}.\left(u_2^B - u_2^C\right) \tag{34}$$

$$K_{II}^{BC} = \frac{2\mu}{\kappa+1}\sqrt{\frac{\pi}{l}}.\left(u_1^B - u_1^C\right) \tag{35}$$

Similarly for points D and E with r = l,

$$K_I^{DE} = \frac{\mu}{\kappa+1}\sqrt{\frac{2\pi}{l}}.\left(u_2^D - u_2^E\right) \tag{36}$$

$$K_{II}^{DE} = \frac{\mu}{\kappa+1}\sqrt{\frac{2\pi}{l}}.\left(u_1^D - u_1^E\right) \tag{37}$$

Now K_I and K_{II} are obtained by linear extrapolation of K_I^{BC}, K_I^{DE} and K_{II}^{BC}, K_{II}^{DE} to the tip at A; then

$$K_I = 2K_I^{BC} - K_I^{DE} \tag{38}$$

$$K_{II} = 2K_{II}^{BC} - K_{II}^{DE} \tag{39}$$

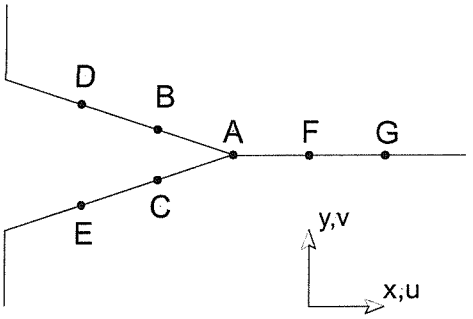

Figure 62: Node in the vicinity of the crack tip

In addition, the stress intensity factor can also be obtained from the extrapolation of the traction ahead of the crack to the tip.

The extrapolation is usually performed automatically in many FE packages. In ANSYS, it is done in the general postprocessor by means of the LPATH and KCALC commands.

The strain energy release rate G is calculated from the following equation:

$$G = \frac{\left(K_I^2 + K_{II}^2\right)(\kappa+1)}{2G_c} \tag{40}$$

where G_c is the core shear modulus.

7.3 Results of parametric study

The ratio a/L* is defined as the ratio between the actual crack length and the maximum length the crack can run at 45° to the interface, or $\sqrt{2}\,t_c$. The distance d^* is the distance between the crack tip on upper interface and the beam end – indicating the offset from the crack.

7.3.1 *G* sensitivity to a/L*

Sensitivity of strain energy release rate *G* to relative crack length a/L* is presented in Figure 63. *G* is plotted against a/L*. *G* value converge towards zero as a/L* tends towards zero. *G* increases as a/L* increases. *G* reaches values close to unity for a/L* values close to 1.

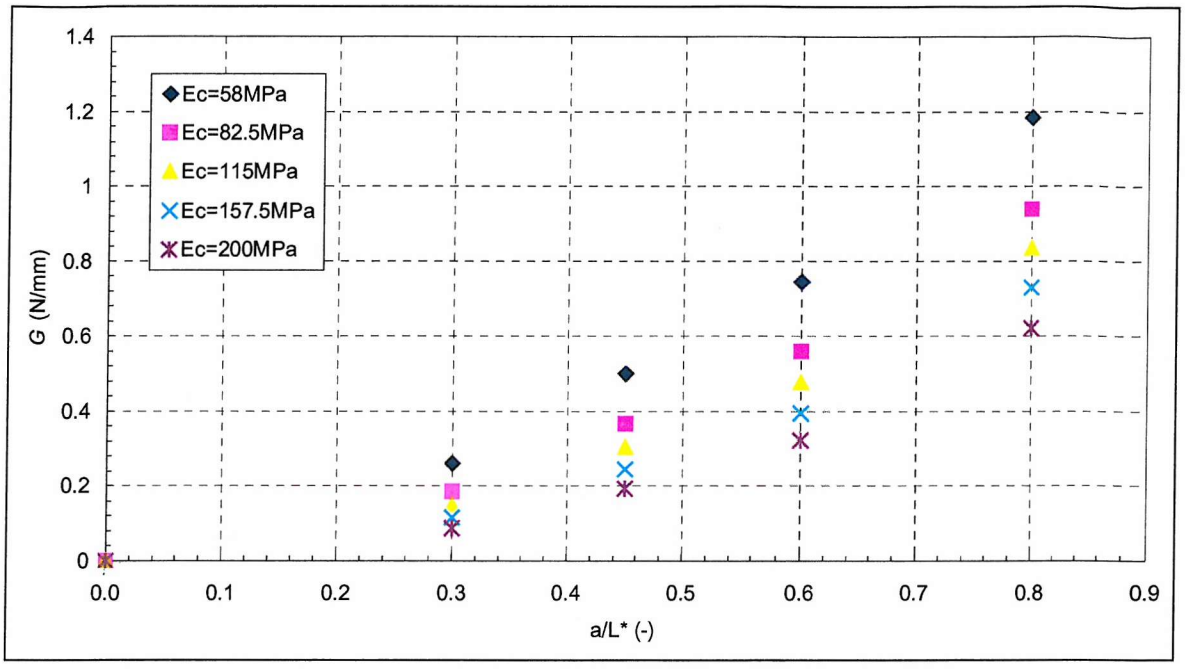

Figure 63: *G* vs. a/L* - *G* sensitivity to core elastic moduli E_c (and G_c), i.e. for E_c=115 MPa, G_c=50 MPa according to the material properties of each foam density.

7.3.2 *G* sensitivity to E_c and G_c

Strain energy release rate *G* sensitivity to the core Young's modulus E_c and shear modulus G_c is presented in Figure 63. *G* is plotted against a/L* for 5 different E_c and G_c pair of values (corresponding to foam core of density varying from 50 to 200 $kg.m^{-3}$). Figure 63 shows that, for a given crack length, *G* increases with decreasing E_c. For short crack length, the effect of E_c on *G* is smaller compared to the effect for larger crack length.

7.3.3 *G* sensitivity to t_c

Strain energy release rate *G* sensitivity to the core thickness t_c is presented in Figure 64. *G* is plotted against a/L* for 6 different t_c values. *G* values for t_c = 10 mm and short crack lengths are not presented because, for this case, the numerical investigation did provide any good results; a slightly modified mesh would have been necessary to obtain the fracture parameters values. However, the *G* values can be extrapolated from the graph. Figure 64 shows that, for a given crack length, *G* increases with decreasing t_c. For short crack lengths, the effect of t_c on *G* is smaller compared to the effect for larger crack length.

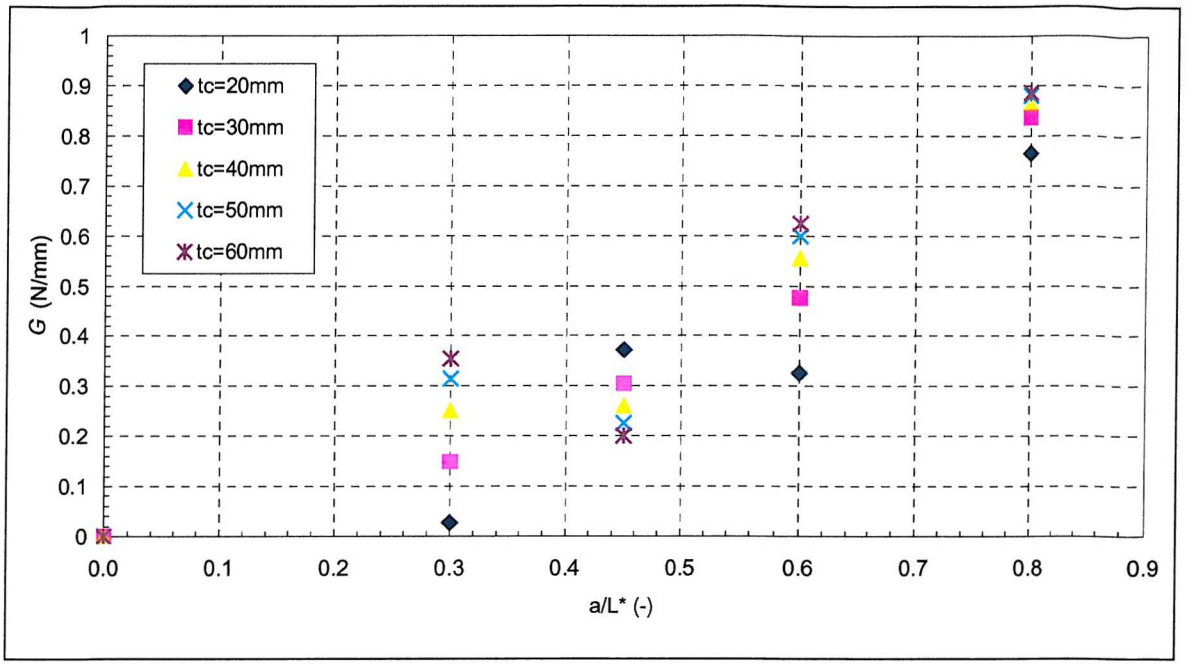

Figure 64: *G* vs. a/L* - *G* sensitivity to core thickness t_c

7.3.4 *G* sensitivity to longitudinal crack position

Sensitivity of strain energy release rate *G* to longitudinal crack position d* is presented in Figure 65. *G* is plotted against d* for a/L*=0.5. Figure 65 shows that *G* values are fairly constant - although slowly decreasing with increasing d* - when the crack is not situated near from the support (d* = 100 mm) or close to the load application point (d* = 350 mm). If the crack is near these two positions, *G* decreases as the crack gets closer to the critical location.

Figure 65 presents *G* sensitivity to d, but *G* vs. a/L* for 6 different d* values. *G* values for the offset value of 130 do not seem to be as consistent as for the other offset values. Figure 66 shows that *G* varies very little with d. For a/L*≅ 1 *G* is almost constant whatever d* is. For a/L*< 0.7, *G* slowly decreases with increasing d. For a/L*> 0.7, *G* moderately increases with increasing d.

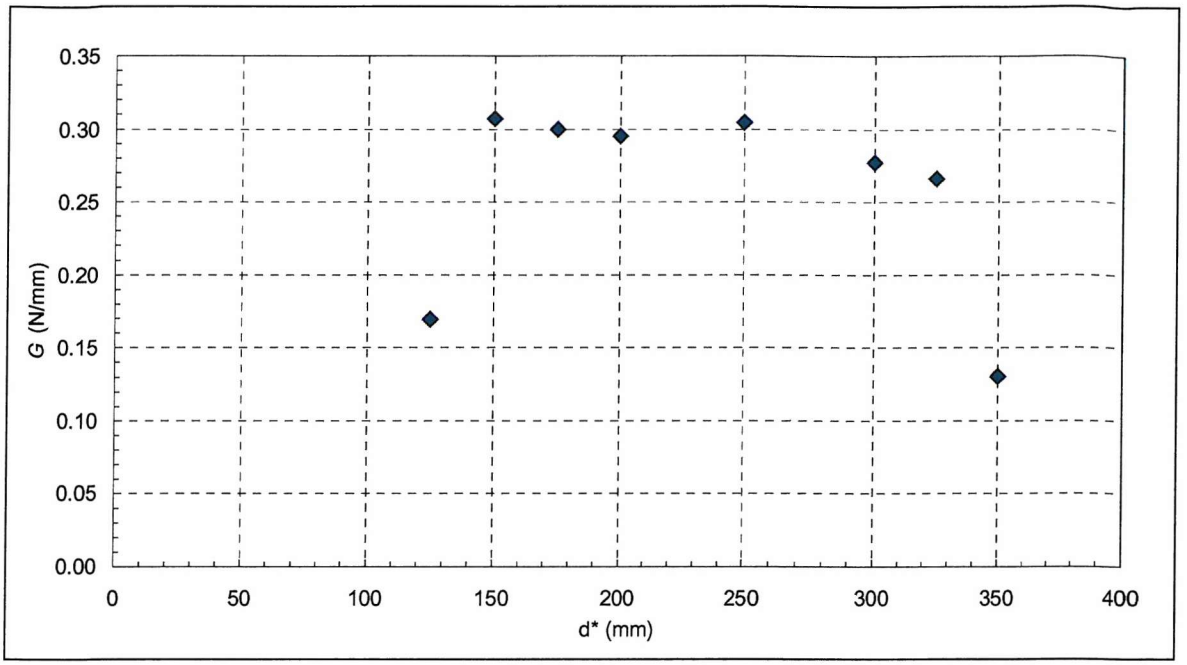

Figure 65: *G* vs. d* for a/L* = 0.5

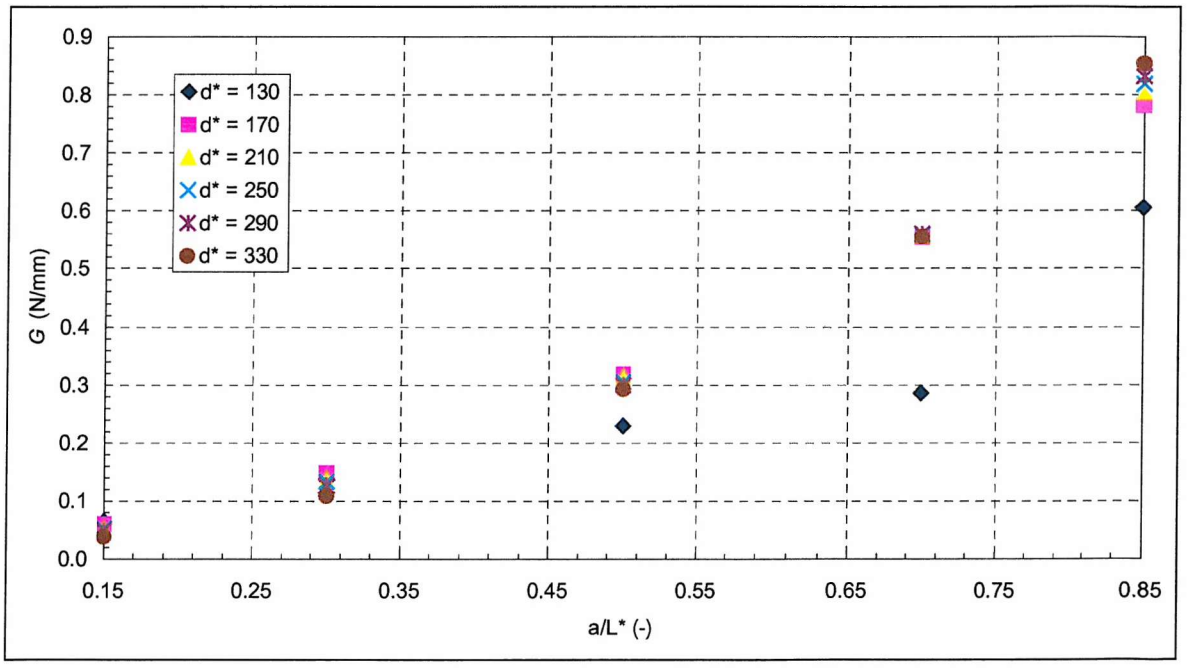

Figure 66: *G* vs. a/L* - *G* sensitivity to longitudinal crack position d*

7.3.5 K_{II} / K_I sensitivity to a/L*

Sensitivity of stress intensity factor K_{II}/K_I to relative crack length a/L* is presented in Figure 67. Ratio K_{II}/K_I is plotted against a/L*. For small E_c<100 MPa, K_{II}/K_I increases as a/L* increases. For E_c>100 MPa, K_{II}/K_I decreases with increasing a/L* down to a minimum value and then increases.

Sensitivity of stress intensity factors K_I and K_{II} to relative crack length a/L* is presented in Figure 80 and Figure 81. K is plotted against a/L* for various E_c.

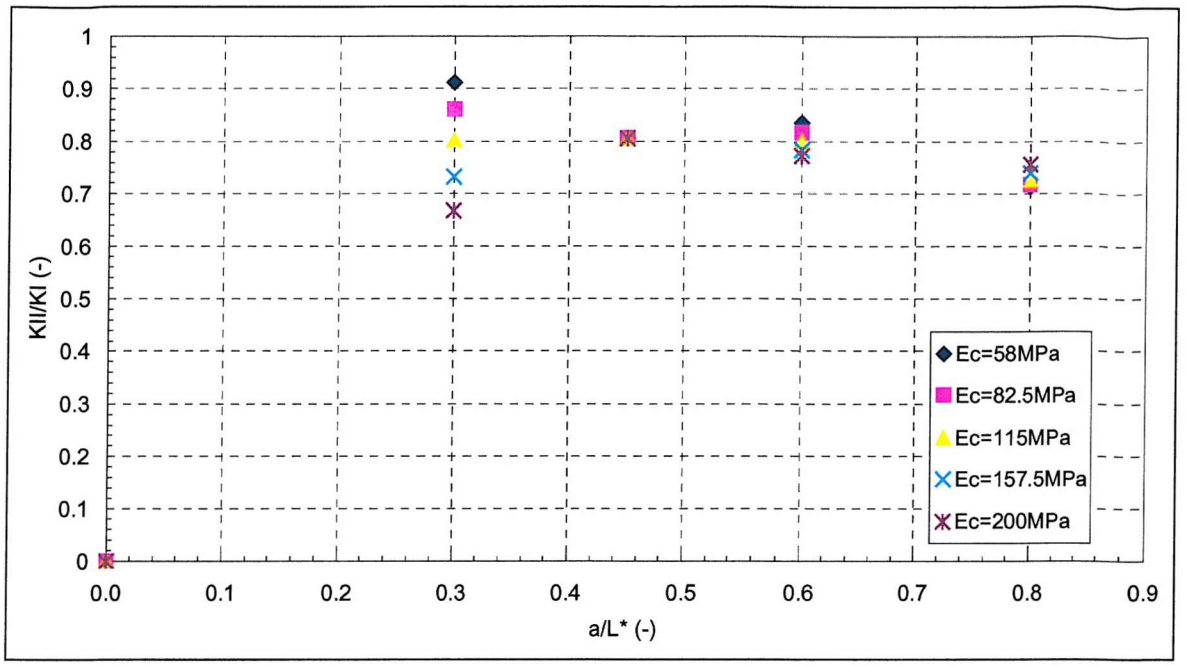

Figure 67: K_{II}/K_I vs. a/L* - K_{II}/K_I sensitivity to core elastic moduli E_c and G_c

7.3.6 K_{II} / K_I sensitivity to E_c and G_c

Sensitivity of stress intensity factor K_{II}/K_I to the core Young's modulus E_c is presented in Figure 67. Ratio K_{II}/K_I is plotted against a/L* for 5 different E_c values. Figure 67 shows that, for a given crack length, K_{II}/K_I increases with increasing E_c. As a/L* increases up to 0.75, all K_{II}/K_I ratios converge - some increasing and some decreasing with increasing a/L* - towards $K_{II}/K_I \cong 0.125$. For a/L* > 0.75 the trend inverts itself; K_{II}/K_I increases with decreasing E_c. Minimum K_{II}/K_I ratio value only exist for Ec > 100 MPa. Minimum K_{II}/K_I increases with increasing E_c.

7.3.7 K_{II} / K_I sensitivity to t_c

K_{II}/K_I ratio sensitivity to the core thickness t_c is presented in Figure 68. K_{II}/K_I is plotted against a/L* for 6 different t_c values. For t_c = 10 or 20 mm and for a/L* < 0.3, and 0.5 respectively, K_{II}/K_I values are not presented for the same reasons as those explained hereinbefore. For a given t_c, K_{II}/K_I is almost constant for a/L* lying between 0.25 and 0.75. For a given a/L*, K_{II}/K_I increases with increasing t_c.

Stress intensity factors K_I and K_{II} versus relative crack length a/L* is presented in Figure 82 and Figure 83.

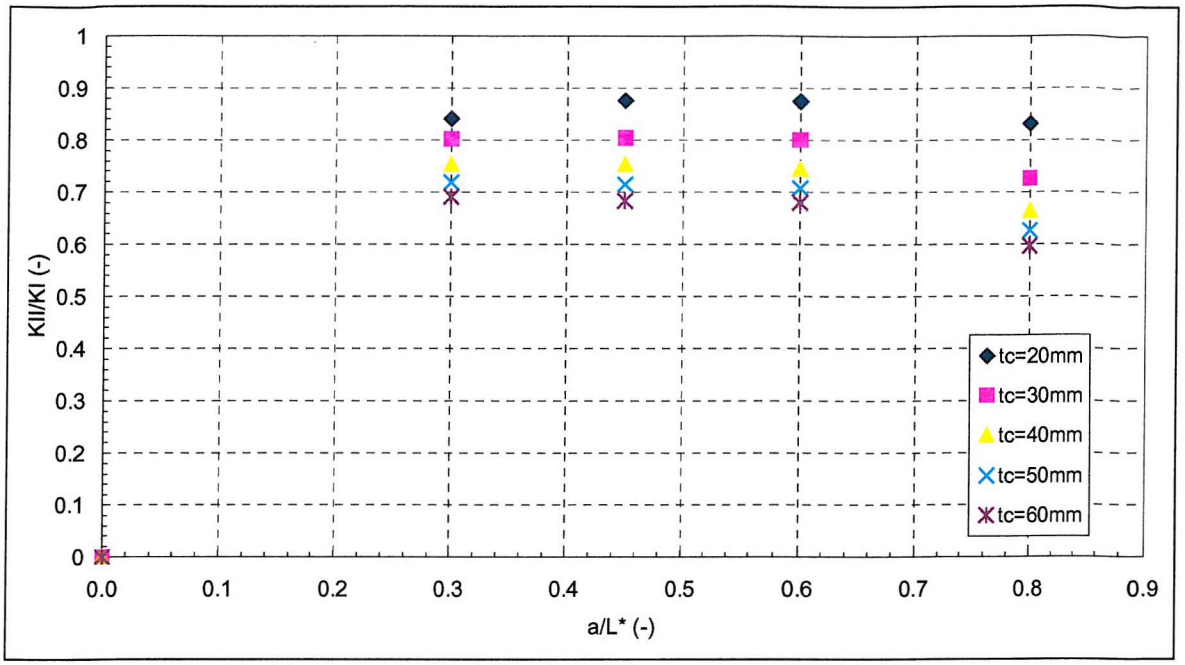

Figure 68: K_{II}/K_I vs. a/L* - K_{II}/K_I sensitivity to core thickness t_c

7.3.8 K_{II} / K_I sensitivity to longitudinal crack position

K_{II}/K_I ratio sensitivity to longitudinal crack position is presented in Figure 69. K_{II}/K_I is plotted against a/L* for 6 different d* values. For d* = 130 and 170 mm, K_{II}/K_I increases very dramatically with decreasing a/L*. For larger d* values, K_{II}/K_I lies mainly between 5 and 11. At a given a/L* inferior to 0.5, K_{II}/K_I increases with increasing t_c. The trend reverses itself for a/L* > 0.5.

Figure 84 and Figure 85, representing respectively K_I and K_{II} vs. a/L* and found in the Appendix, show that K_I values are more stable than K_{II} ones.

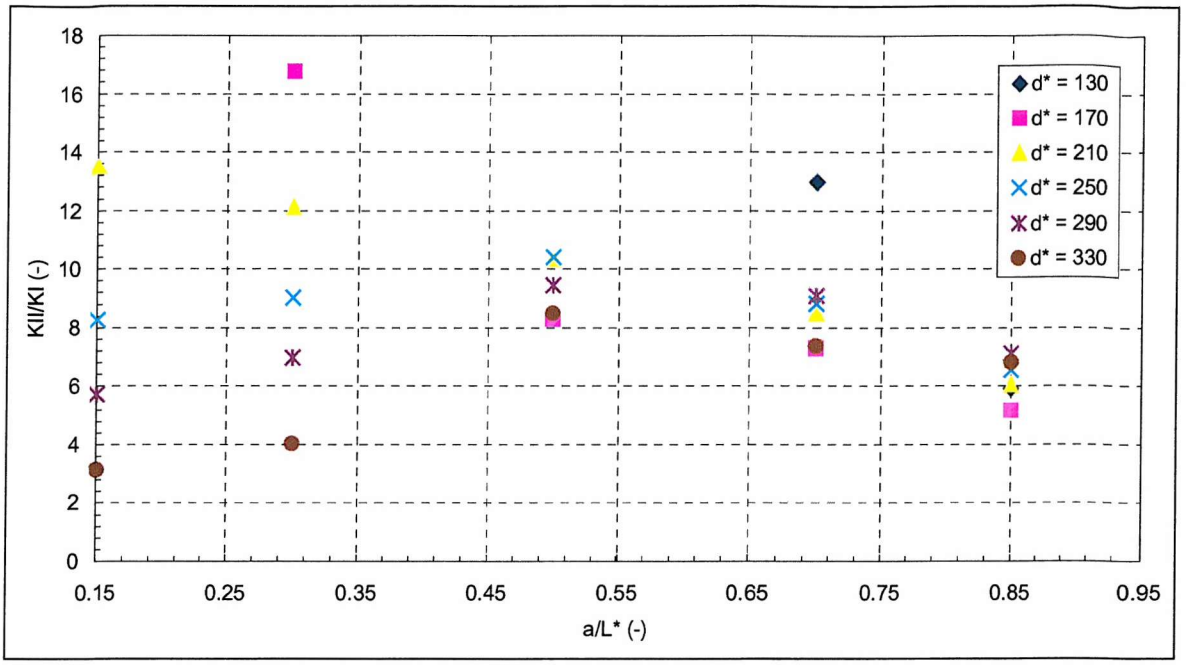

Figure 69: K_{II}/K_I vs. a/L* - K_{II}/K_I sensitivity to longitudinal crack position d*

7.4 Discussion

7.4.1 Fracture load prediction – Correlation with static CTS testing

Although computational methods are very useful in fracture mechanics, they cannot replace experiments - fracture toughness K_{Ic} and K_{IIc} can only be experimentally determined. A numerical fracture simulation of a cracked body can compute crack tip parameters, but such an analysis alone cannot predict when fracture will occur. To do so, experimental fracture boundary curve or accurate fracture criteria are also required.

7.4.1.1 Experiment on foam core under static mixed-mode loading

The aim of the experiment presented in Chapter 4 was to determine the stress intensity factors K_I and K_{II} under in plane loading mode-I, mode-II, and mixed-mode. K_Q is computed from

$$K_Q = \frac{P_Q \cdot \sqrt{\pi \cdot a}}{w.t} \cdot f\left(a/w\right) \qquad (41)$$

Results for the foam C70.130 are presented in Table 22 and plotted in Figure 70.

Table 22: Mean stress intensity factors K for C70.130 foam

	mode-I	mixed-mode		mixed-mode		mode-II
α	0°	30°		60°		90°
	K_I	K_I	K_{II}	K_I	K_{II}	K_{II}
K	0.283	0.220	0.061	0.106	0.089	0.148

7.4.1.2 Comparison of numerical K_{II}/K_I values vs. experimental K_{II}/K_I

Numerical results show that the mean value of K_{II}/K_I ratio is about 1/10. The results compare well with independent investigation[27]. Although the beam is loaded in *quasi*-pure shear, fracture propagation mainly due to direct stresses, i.e. opening mode. Though mode-I dominates, mode-II is always present. This is in agreement with the findings of Chapter 4 and 5. K_{Ic} should be considered as a main design parameter. Experimental values of kinking angle for mode-I is approximately equal to 0 degree. Crack path remains at 45° to the faces and does not kink, or does so very moderately.

7.4.1.3 Fracture envelope and crack propagation

Numerically-determined crack tip parameters can be used in conjunction with an experimental data to predict fracture load for a given damaged sandwich beam or conversely critical crack length for an applied load on a structure.

A given beam configuration was selected; mechanical and physical properties are shown in Table 23.

Table 23: Mechanical and physical properties of a selected beam

t_f	t_c	width	a/L*	E_f	G_f	ν_f	E_c	G_c	ν_c
(mm)	(mm)	(mm)	(-)	(MPa)	(MPa)	(-)	(MPa)	(MPa)	(-)
2	30	35	0.5	22000	2500	0.28	109	50	0.32

Stress intensity factors K_I and K_{II} are determined numerically for a range of loads. Results are shown on Figure 70; K_{II}/K_{IC} is plotted against K_I/K_{IC}, together with experimentally determined K values.

Figure 70 shows that numerically-determined stress intensity factor values K_I and K_{II} increase with increasing load. There is a critical load value, P_{cr}, at which the fracture locus lays on the fracture boundary curve. At P_{cr} - approximately equal to 1575 N - the crack is expected to propagate. For points lying within the boundary - bottom left part of the graph - fracture conditions are such that no crack extension is expected to occur. Stresses at the crack tip are lower than the fracture stress. The damaged beam can withstand the applied load. For the fracture loci situated outside this region, crack is expected to propagate.

Table 24: Numerically obtained fracture parameters for the damaged beam

P	K_I	K_{II}	K_I	K_{II}	K_I / K_{IC}	K_{II} / K_{IC}	G
(N)	(MPa.mm$^{0.5}$)	(MPa.mm$^{0.5}$)	(MPa.mm$^{0.5}$)	(MPa.mm$^{0.5}$)	(-)	(-)	(N/mm)
1225	6.7415	0.7149	0.2132	0.0226	0.7528	0.0798	0.0266
1400	7.7045	0.8170	0.2437	0.0258	0.8604	0.0912	0.4548
1435	7.8971	0.8374	0.2498	0.0265	0.8819	0.0935	0.4778
1470	8.0898	0.8579	0.2558	0.0271	0.9034	0.0958	0.5014
1505	8.2840	0.8783	0.2620	0.0278	0.9251	0.0981	0.5255
1540	8.4750	0.8987	0.2680	0.0284	0.9464	0.1004	0.5502
1575	8.7676	0.9191	0.2773	0.0291	0.9791	0.1026	0.5756
1610	8.8602	0.9396	0.2802	0.0297	0.9894	0.1049	0.6015
1645	9.0528	0.9600	0.2863	0.0304	1.0109	0.1072	0.6278
1680	9.2454	0.9804	0.2924	0.0310	1.0325	0.1095	0.6548
1715	9.4380	1.0008	0.2985	0.0317	1.0540	0.1118	0.6824
1750	9.6307	1.0213	0.3046	0.0323	1.0755	0.1141	0.7105
1925	10.5937	1.1234	0.3350	0.0355	1.1830	0.1255	0.8598

However, it is not known whether the crack propagation is stable. To be able to assess the stability of the crack propagation in the core material, an R-curve determined for the structure would be necessary; G and R would have to be plotted against crack length. Only G values have been determined numerically in this investigation but R-curve could be determined numerically using an accurate fracture criterion. It would be, however, a long process, and experimentation would be more accurate and quicker.

Figure 70 shows that scatter is present in the experimental results. This should be taken into account when trying to estimate the load at which the crack propagates; lower bound values should be used for safe design approach.

Sandwich panels can fail in different ways; faces and core can yield plastically or fracture depending on the nature of the materials from which they are made. According to Triantafillou[96], 3 modes of failure appear to be relevant for sandwich beams made from face or core that yield plastically: face wrinkling, face yield and core shear. Critical failure mode, which occurs at the lowest load, may not be necessarily core shear depending on the properties and the design of the beam.

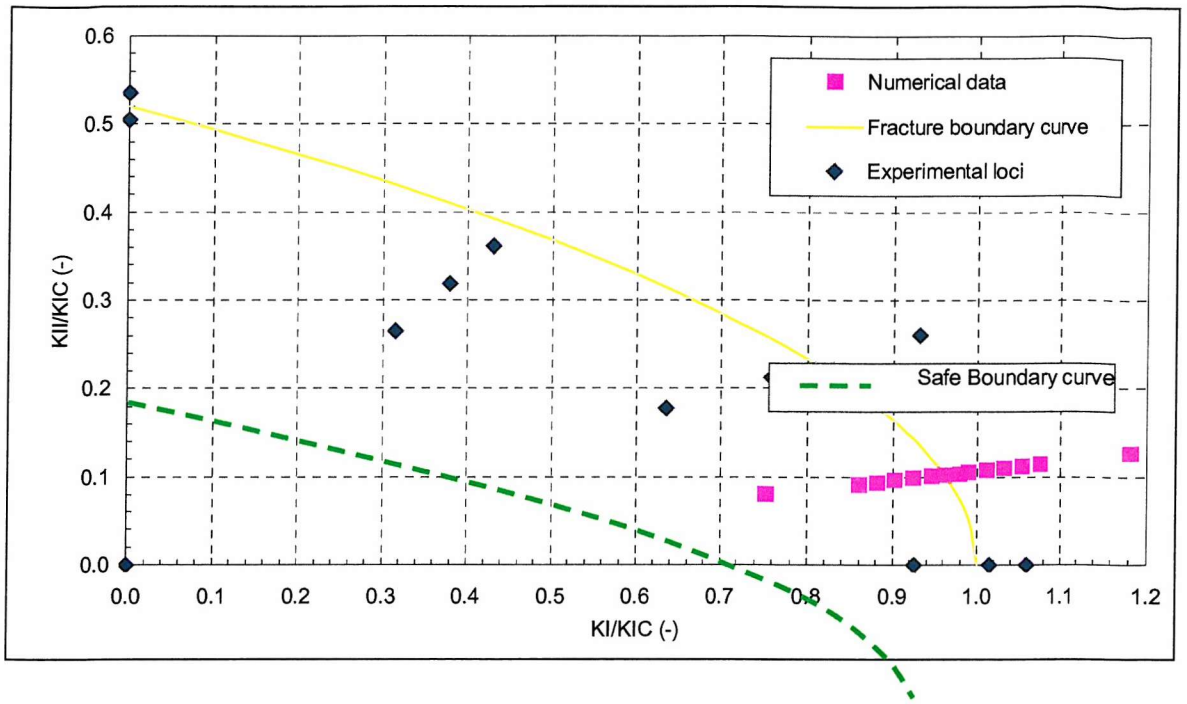

Figure 70: Foam core shear fracture boundary for a given cracked sandwich beam

7.4.2 Stress intensity factor – correlation with fatigue 4PTB testing

Using the mapping of K_I for various beam geometry and material configuration presented in the previous chapters and in the Appendix, stress intensity factor variation can be extracted.

Correlation between crack growth rates and stress intensity factor variation was established between the CTS and 4PTB test specimen in Chapter 6. These were found to be of the order of 10^{-2} mm/cycle and about 8.0 MPa.mm$^{0.5}$ respectively at the end of the fatigue life, see Figure 29.

Assuming a crack length of about 30 mm (or a/L*=0.42) at the end of the fatigue life, material properties pertaining to the C70.130 variety, and identical beam and crack topology, numerical K_I value can be extracted from Figure 80. The figure indicates K_I being equal to about 5 MPa.mm$^{0.5}$. This result can be compared the experimental K_{max} value, i.e. 8.0 MPa.mm$^{0.5}$, determined at the end of the fatigue life of 4PTB specimens. The comparison shows that they are not in accordance but of same order of magnitude. Considering all the approximations on load level, crack fracture length and topology, this result can be estimated as qualitatively satisfactory. Further modelling work and testing should lead to more accurate results.

7.5 Conclusions

Numerical results show logical trends and compare well with independent investigations. The strain energy release rate G decreases as crack length increases; it decreases with decreasing E_c and G_c, i.e. density; it decreases with decreasing t_c; it is constant over the part of the beam subject to pure shear loading. Under pure shear loading, fracture propagation is

mainly due to opening stresses, mode-II is always present though. Fracture toughness K_{IC} can be used as a design parameter for engineering purposes. Fracture boundary curve may successfully be used in conjunction with FE analysis to determine a range of critical load or critical crack length. Qualitative correlation between stress intensity factors variations extracted from FE analysis and derived from experimental results has been successfully established.

8 DISCUSSION

The fatigue and fracture behaviour of PVC foam core in sandwich structures has been investigated.

Existing numerical models for calculating mode-I and mode-II stress intensity factors, or strain energy release rates for cracks have been extended. Previous knowledge on fatigue and fracture of polymeric foam has been broadened by applying for the first time experimental techniques to determine fracture and fatigue crack behaviour under a variety of loading conditions. Further, former damage and crack growth process at both macro- and microstructural level have been refined and extended to the variety of cross-linked PVC foam.

8.1 Correlation between numerical and experimental

8.1.1 Numerical crack tip parameters and experimental fracture envelope

Numerically-determined crack tip parameters have been obtained from FEA for a CTS specimen. Fracture boundary curve have been derived from set of experimetally-determined fracture loci, and from a semi-empirical criterion based on experimentally-determined fracture toughness value K_{IC}. A correlation between the results have enabled prediction of the fracture load for a given damaged sandwich beam, or conversely critical crack length for an applied load on a structure.

8.1.2 Damage process zone – FE models

FE analysis has shown that, for a 4PTB sandwich test, the zone of highest stresses, is typically located at the centre of the area situated between the support and load point – although the state of shear stress between the support and load point is not absolutely constant[47].

Final fracture in 4PTB specimen takes place at the end of the fatigue life as a result of repeated large shear deformations occurring in the zone situated between the support and load application point. Experimental evidence supports the FE analysis findings.

8.1.3 Numerical crack tip parameters and crack propagation under mode-II loadings

Owing to the large number of possible sandwich configuration, it has been important to determine strain energy release rate G and stress intensity factors K_I and K_{II} for a range of physical and mechanical properties that are characteristic of a typical sandwich beam.

It has been found for this material that, under pure shear loading, fracture propagation is mainly due to opening stresses, mode-II is always present though. This is supported by the crack growth rates measured on 4PTB sandwich specimens. Under mode-II loading, the

shear crack tip grows according to mode-I propagation, but with a low accompanying mode-II.

8.1.4 Measured crack growth rate on the 4PTB specimen and the numerical K_I value

Using the mapping of K_I for various beam geometry and material, stress intensity factors K_I have been extracted. The numerical results have indicated K_I being equal to about 5 MPa.mm$^{0.5}$. This result is not in accordance with the derived K_{max} value of 8.0 MPa.mm$^{0.5}$ – originally for the 4PTB specimen. Considering the numerous simplifications and assumptions (crack length at fracture of 30 mm), this results can be estimated as qualitatively satisfactory. Further tests and analyses are needed to lead to more accurate results.

8.2 Correlation between material and structure

8.2.1 Crack growth rates

Crack growth rates have been determined for 4PTB single-shear-cracked specimens. The values range from 0.006 to 0.012 mm/cycle near the end of the fatigue life, constantly increasing until final failure. Crack growth rates under mode-I, mode-II and mixed-mode loading conditions have also been determined using the CTS specimen. For this specimen, the crack growth rates have been found 0.00025 mm/cycle to 0.12 mm/cycle. Under mode-II loading, mode-II da/dN_{CTS} are of the order of 10^{-4} mm/cycle, whereas mode-I da/dN_{CTS} are up to about 10^{-2} mm/cycle before final fracture. This was due to crack growth in the K_I direction with a low accompanying K_{II}.

The mode-I crack propagation rates, obtained for both CTS and 4PTB specimens under mode-II loading, are of the same order towards the end of the fatigue life. The final crack propagation rates are of the order of 10^{-2} mm/cycle. Fatigue crack growth in a 4PTB foam cored sandwich beams can be considered to be K_I-controlled. Observation on crack propagation angle in 4PTB specimens supports this explanation.

8.2.2 Crack propagation angles

In the 4PTB specimen, for both single and multiple cracks, the fatigue crack propagation angle has been measured to run at about 63° relative to the neutral axis of the beam. The value differs from the static propagation angle, i.e. 45°. The fatigue crack propagation angles have been correlated by the findings presented in Chapter 5 for cracked CTS foam specimen. Under pure mode-II fatigue loading, crack propagation angle was found to be equal to approximately 60°. Further, crack propagation angles under mode-II loading, the shear crack tip grows according to mode-I propagation, but with a low accompanying mode-II.

8.3 Correlation between static and fatigue

8.3.1 Fracture toughness K_{IC} and K_{IIC} and stress intensity variation ΔK_I

The experimental results on pure mode-I and mode-II fracture toughness of AIREX C70 foam have shown that fracture toughness K_{IC} is equal to about 0.28 to 0.26 MPa.$m^{0.5}$. Fatigue crack growth tests, using the same CTS test method, have shown that stress intensity variation ΔK_I equal to 9.7 MPa.$mm^{0.5}$ (or 0.31 MPa.$m^{0.5}$). This value corresponds to a K_{max} value that is a few percent higher than the K_{IC} value obtained from static testing. Further, fracture toughnesses have been found to differ according to the direction of the material; the difference may reach 10%.

8.3.2 Kinking angle

Experimentally obtained deflection angles from static fracture tests compare well with initial path behaviour for fatigue conditions. The hoop stress criterion is in better agreement than the four other criteria. Here, if no experimental kinking angle value is available, the maximum hoop stress criterion is the best predictive model, as previously established for this material under static loading conditions. The theory however appears to be deficient in predicting accurately both fracture locus and fracture angle. There are convincing arguments and indications showing that the micromechanics of the cell is the key to the formulation of better fracture criteria for mixed-mode and mode-II loadings; this will be expended on later in this chapter.

8.4 Correlation between mode mixity

8.4.1 Fracture envelope and dominant mode-I

As suggested earlier, the hoop stress criterion is in better agreement than the four other criteria. Further, Richard's criterion, using experimentally obtained K_{IIC} and K_{IC}, is the best in predicting both fracture locus and fracture angle accurately.

Experimental investigations using the CTS test method have suggested that mode-I is dominant and, if loaded in mode-II, the crack kinks in order to align itself in the direction of least energy for further propagation. This has been observed in the 4PTB and CTS test series under static and fatigue.

8.4.2 Co-planar growth under pure mode-II loading

The incidence of co-planar growth in the mode-II tests has clearly shown the existence of a pure shear growth mode in cellular foam material. The early arrest of shear crack growth is a well-established phenomenon in metallic systems, and is generally attributed to friction force set up in the shear crack wake. The implications of crack wake friction in the present

system are not known. However, the present results are consistent with this process being significant. The existence of a pure shear growth mode in this material indicates that, under different loading conditions, e.g. shear and compression, the K_{II} controlled co-planar crack growth may be significant.

8.5 Creep, stiffness degradation, damage formation and growth

8.5.1 Creep and stiffness degradation

Previous studies on high cycle fatigue have shown that flexural fatigue could be characterised by an increase in deflection and constant stiffness for most of the fatigue life. Just before final failure, stiffness reduction occurs.

For medium and high cycle fatigue, the dominant phenomenon is creep until just prior to failure. However, it has been found that, for low cycle fatigue, crack initiation and growth are the dominant phenomenons. Large shear deformation occurs very early in the fatigue life, inducing early damage formation and crack nucleation. The distinction of the transition of the two fatigue regimes is not obvious as damage initiation and crack nucleation is only visible afterwards.

Also, for most engineering structures, creep measurement is probably a good indicator of the integrity of the sandwich structure.

8.5.2 Damage formation model

Large core shear yielding inducing damage and causing subsequently the stiffness degradation has been described in earlier models for the linear variety of PVC foams and for the cross-linked type mainly manufactured by DYVINICELL.

For cross-linked foam manufactured by AIREX, the damage formation has shown some degree of difference. After a phase of intensification of shear deformations and cell decohesion, crack initiation sets in by the nucleation of either one single shear crack or several multiple cracks aligned horizontally along the centreline in the damage process zone. Further, the damage formation and growth of multiple cracks appears more ductile as cracks propagate in more damaged material than that of a single shear crack.

8.5.3 Crack propagation model and criteria

An early microstructural crack propagation model proposed a cell by cell crack advance for polymeric cellular material – for a variety of foam different than the cross-linked PVC one. A microstructural model for the fatigue crack propagation at low ΔK proposed a crack extension by one cell diameter through cell wall after repeated flexion of the cell wall in front of the crack tip.

Observation supports this model for low ΔK. However, for a high ΔK, an improved microstructural model taking into account the strong microstructural effects is proposed:

- the crack propagates through not necessarily one but possibly several cell walls at a time
- the crack advances after a sufficient amount of damage has built up in the zone ahead of the crack tip. A variable number of cycles is required to produce the critical amount of damage
- the crack length increment and the number of cycle required for this increment are dependent on the topology of the cell walls in the viscinity of the crack tip for a given ΔK

Fatigue crack growth rates for other polymeric cellular materials have previously been determined using different test methods. In this investigation, a novel Paris power law relationship has been established for cross-linked PVC cellular foam showing a linear variation of log da/dN with log ΔK .

Forceful findings related to crack growth (being governed by local plastic deformations and local damage accumulation process) suggested that a strain-based model could be used to model crack growth rate with, for example, volume average local strain, or plastic work done over a given volume, instead of using the Paris law relation based on ΔK.

It is also reasonable to suggest strain-controlled criterion for fracture prediction. Fracture criteria for metals based on stress (or K) parameters have been used to predict successfully the fracture locus and fracture angle of PVC foam. These criteria have however been deficient in predicting both fracture locus and fracture angle for mixed-mode and mode-II load cases.

In fact, the fracture criteria and the damage growth model do not represent the material behaviour at microscopic level. For foam core materials, crack growth appears to be governed by local plastic deformations and local damage accumulation process. There are convincing arguments and indications showing that the micromechanics of the cell is the key to the formulation of better models for mixed-mode and mode-II loadings. However it is beyond the scope of this work to formulate full micromechanical models.

9 FUTURE WORK

The current work has highlighted some areas which require further investigations:

9.1 Fundamental studies

Micro-fatigue and micro-fracture mechanics of the closed-cell belonging to polymeric cellular foam

Microstructural assessment of fracture criteria

Initiation and propagation of cracks in polymeric cellular foam monitoring using acoustic emissions techniques

New monitoring method for detection of crack initiation

Fatigue finite element analysis of crack propagation in polymeric cellular foam core sandwich structures

Interfacial fatigue crack initiation and growth in polymeric cellular foam core sandwich structures

Elastic- plastic fracture mechanics of cellular materials single and multiple shear cracks

Evolution of micro-crack density as a function of stress and fatigue or creep parameters

9.2 Applied studies

Static and cyclic creep in polymeric cellular foam core sandwich structures

Fatigue threshold crack growth measurement ΔK

Prediction of constant amplitude fatigue crack growth in polymeric cellular foam core sandwich structures

Comparison between current predictions methods for crack propagation in polymeric cellular foam

Prediction of variable amplitude fatigue crack growth in polymeric cellular foam core sandwich structures

Effects of loading history on crack initiation and propagation in sandwich structures

Probabilistic fatigue of polymeric cellular foam

Probabilistic fracture mechanics applied to polymeric cellular foam.

10 CONCLUSIONS

The work has been concerned with the characterisation of foam core materials with repeats to fatigue and fracture and the correlation of these results with sandwich structures subjected to flexural loading conditions.

New experimental investigations on mixed-mode fracture and fatigue crack growth have been carried out. Experimental and numerical studies related to practical applications in marine operations, i.e. 4PTB testing, have also been carried out.

The ultimate aim of the research work presented in the thesis has been to broaden the current understanding of the fatigue fracture behaviour and foam-cored sandwich structural specimens under a variety of tensile, shear and mixed-mode static and cyclic fatigue load cases.

The main conclusions from this work are as follows:

- linear elastic fracture mechanics can be applied to the PVC foam for both static and cyclic loading
- CTS specimen, in association with a special loading device, is an appropriate apparatus for experimental mixed-mode fatigue and fracture analysis
- mode-I and mode-II fracture toughness values have been determined for a range of densities; values range from 0.01 to 0.5 $MPa.m^{0.5}$
- K_{IC} fracture toughness is higher in either one of the x or y-direction with variations up to 10%.
- Richard's criterion, using experimentally obtained K_{IIC} and K_{IC}, seems to be the best in predicting fracture locus and fracture angle accurately for static and cyclic loading
- maximum hoop stress criterion also predicts the fracture angle well for static and cyclic loading
- fracture criteria appear to be deficient in predicting accurately both fracture locus and fracture angle
- under pure shear loading, fracture propagation is mainly due to opening stresses, mode-II is always present though.
- micro-structural cell size effect can be a source of scatter in the experimental results
- a refined model for fatigue fracture crack advance is described and proposes improvement for high stress intensity conditions at the crack tip
- crack growth regime is accurately modelled by the Paris law
- crack growth appears to be governed by local plastic deformations and local damage accumulation process

- mode-II co-planar crack propagation can occur in this material
- the flexural fatigue is characterised by 2 regimes: a creep regime inducing small permanent deformation followed by fatigue fracture regime, typically much shorter, responsible for a catastrophic shear stiffness degradation
- for medium and high cycle fatigue, the dominant phenomenon is creep until just prior to failure, whereas, for low cycle fatigue, crack initiation and growth are the dominant phenomenons
- a damage formation has been described; accounts have been made for single shear crack. and multiple shear cracks
- mode-I crack propagation rates, da/dN_{4PTB}, reaches a value of 10^{-2} mm/cycle, towards the end of the fatigue life
- fatigue crack growth in a 4PTB foam cored sandwich beams can be considered to be K_I-controlled.
- fracture parameters, G and K have been mapped as functions of material properties and topology
- fracture boundary curve may successfully be used in conjunction with FE analysis to determine range of critical load or critical crack length
- qualitative correlation between stress intensity factor variations extracted from FE analysis and derived from experimental results has been successfully established

11 APPENDICES

11.1 Introduction

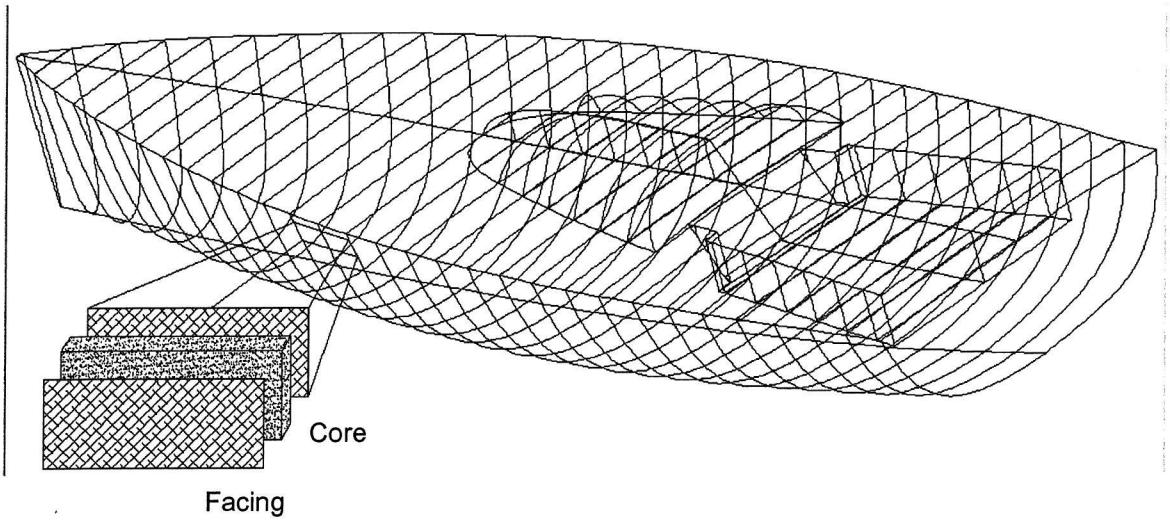

Figure 71:Racing yacht hull made out of sandwich panels

11.2 Mode-I, mixed-mode, mode-II fracture of sharp crack in rigid cellular PVC foam

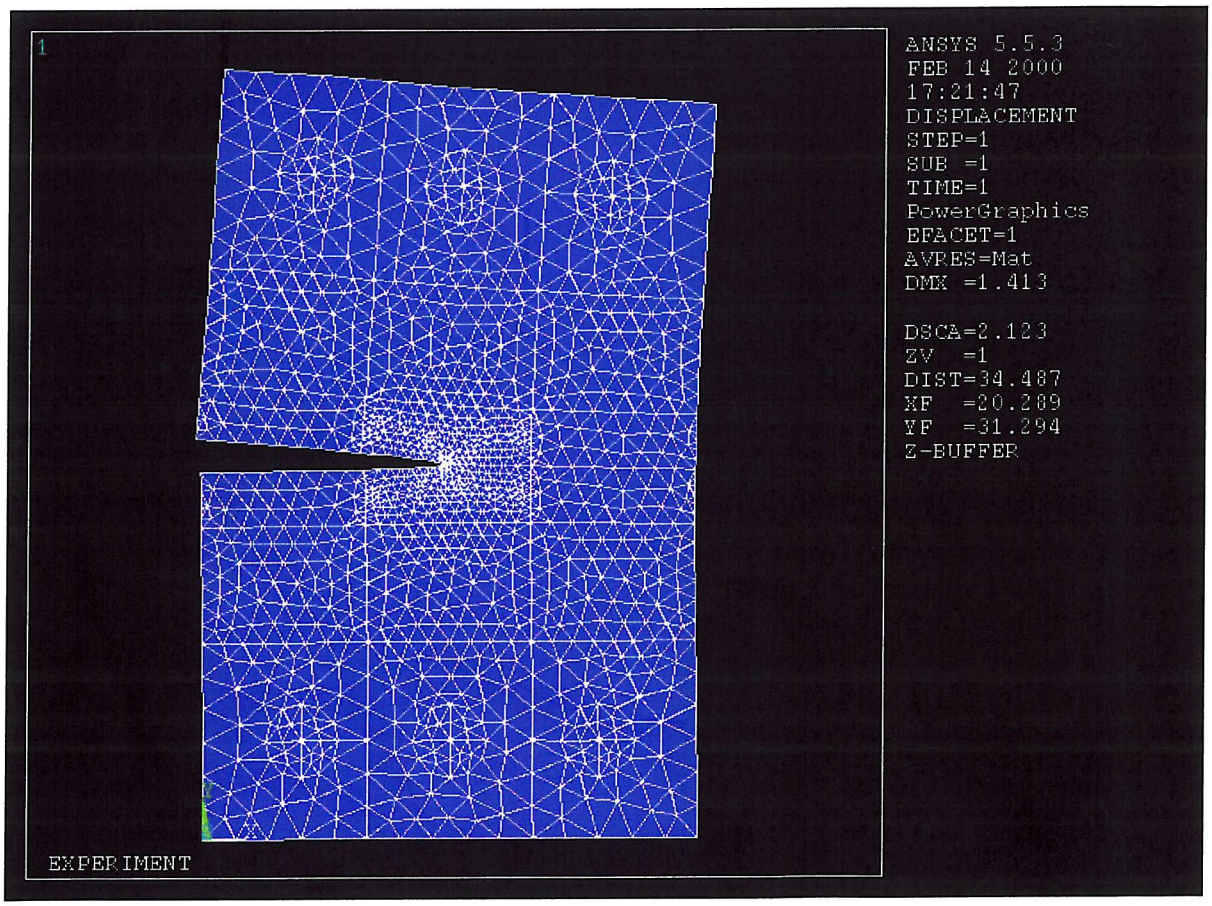

Figure 72: Deformed shape of CTS specimen at fracture load for C70.200 at $\alpha = 30°$ from FEA

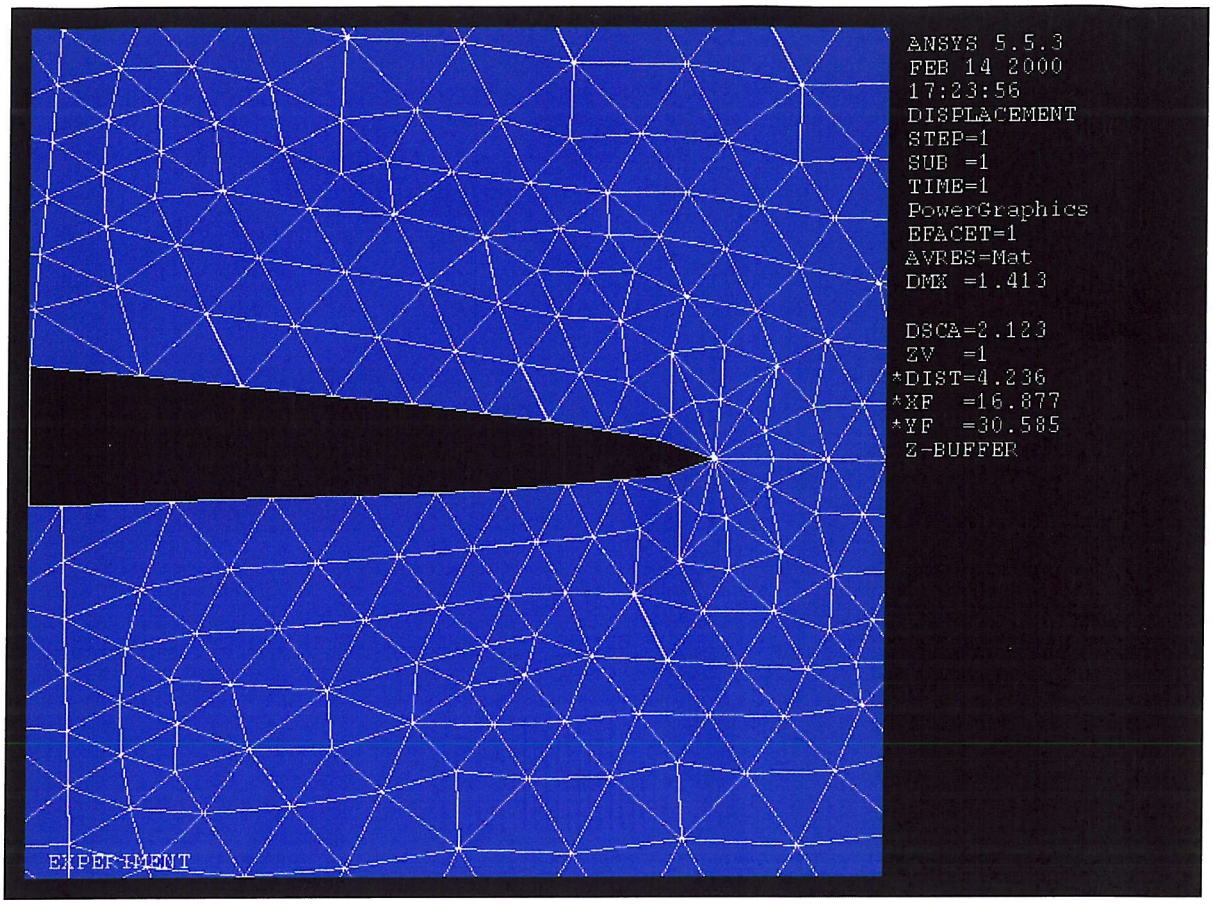

Figure 73: Close up view of deformed shape of CTS specimen at fracture load for C70.200 at $\alpha = 30°$ from FEA – identical to previous figure

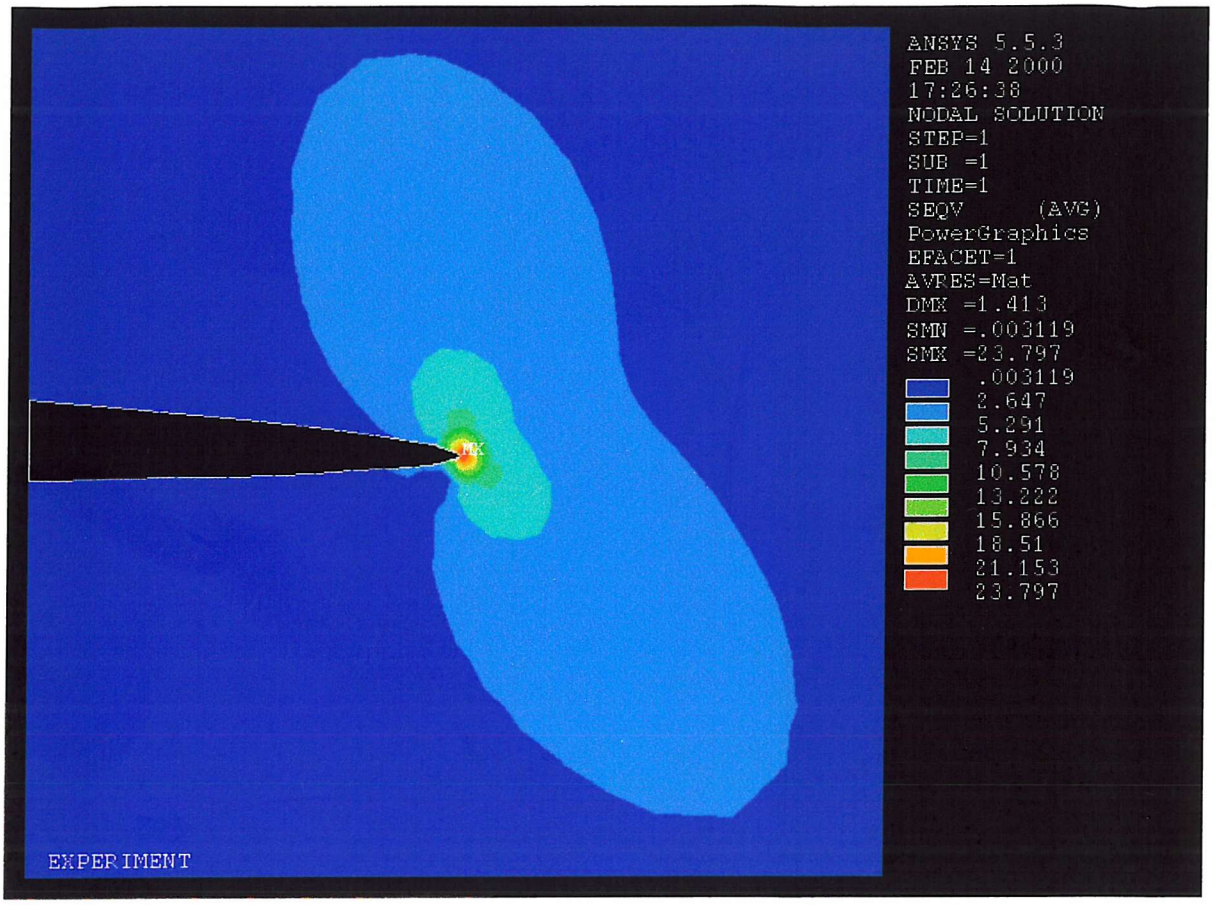

Figure 74: Von Mises isostress lines at fracture load from FEA for C70.200 at $\alpha = 30°$

11.3 Crack growth in rigid PVC cellular foam under mode-I, mixed-mode, mode-II cyclic loading

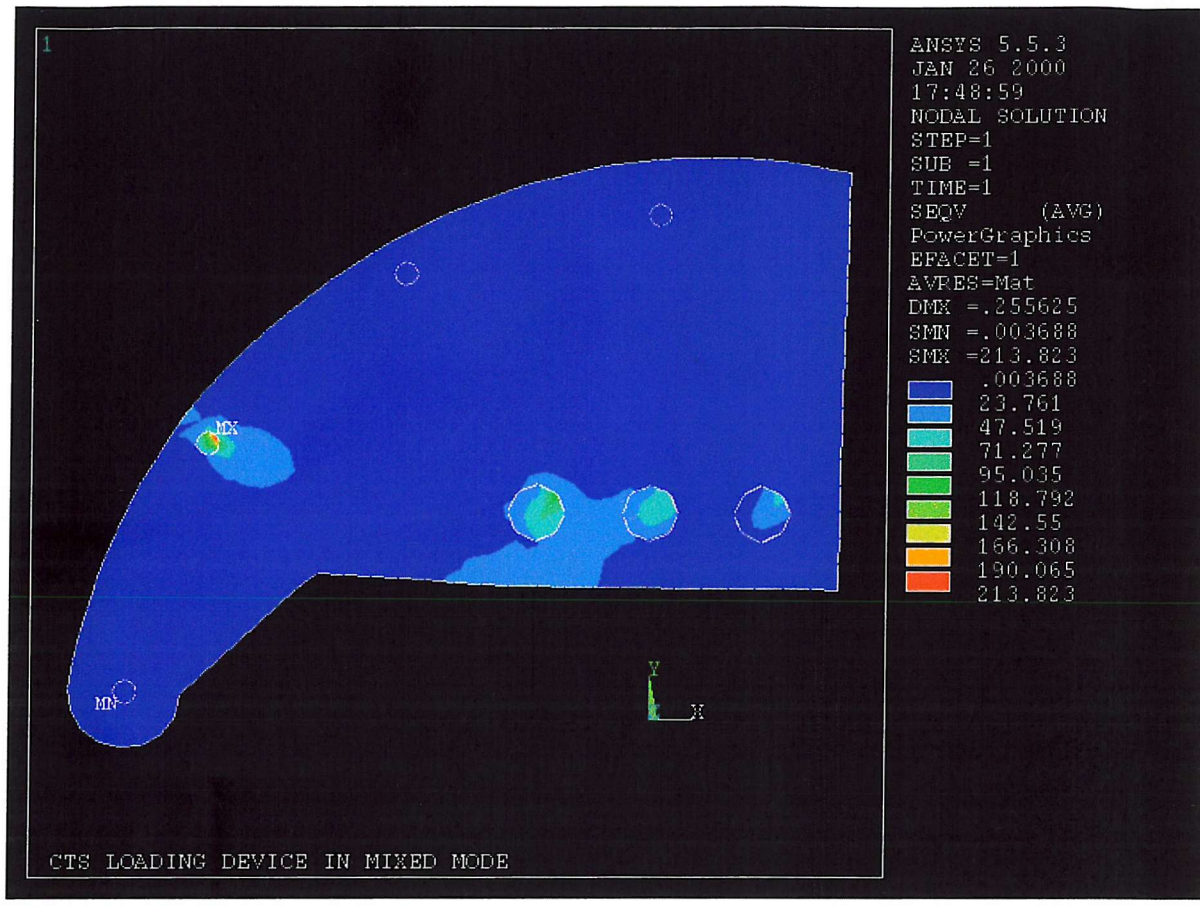

Figure 75: Von Mises stress contours from a FEA of loading device for mixed mode loading case

11.4 Flexural fatigue and fracture in foam cored sandwich beams

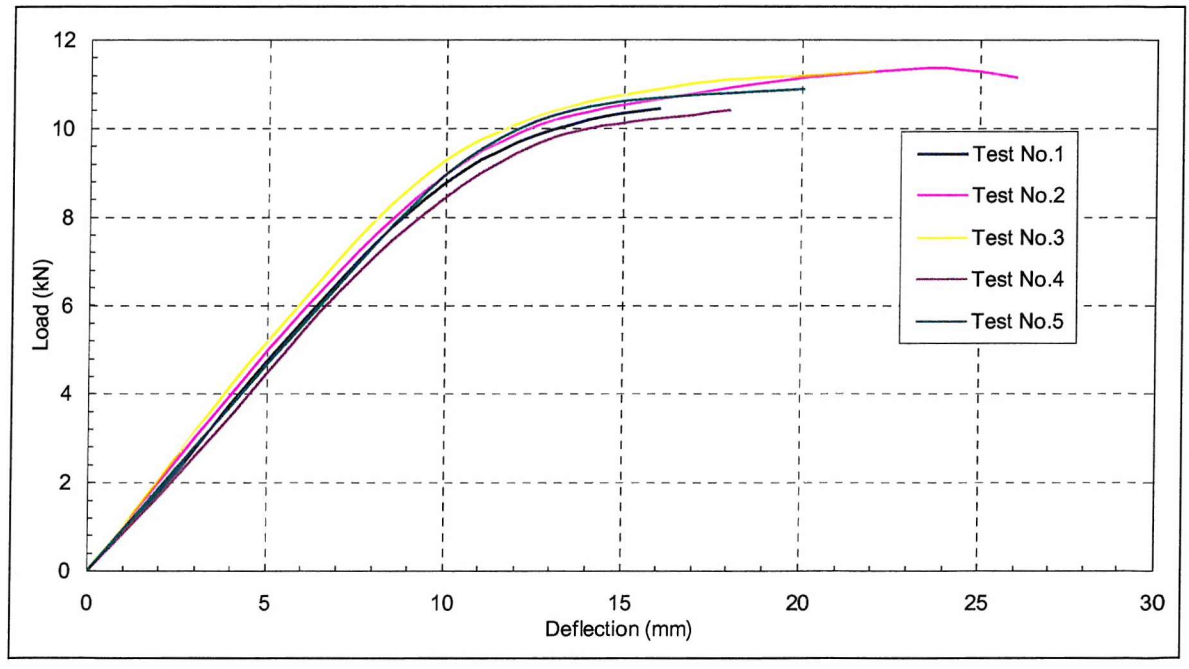

Figure 76:Load vs. deflection curve

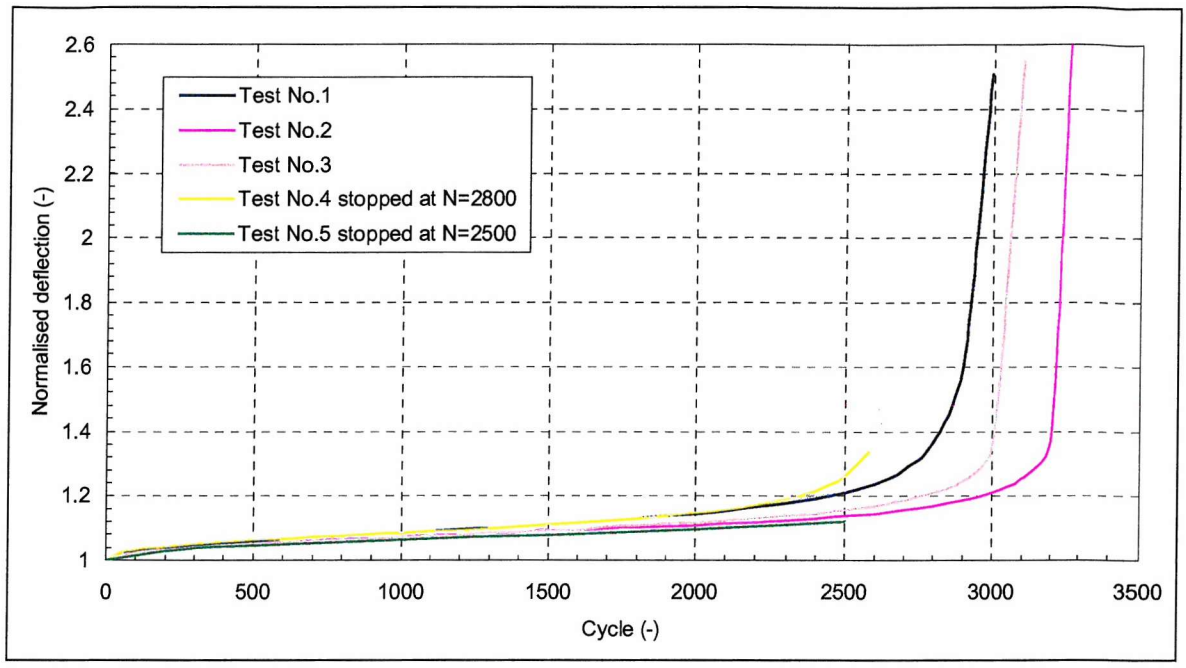

Figure 77: Deflection vs. number of cycles for 75%P_{ult}

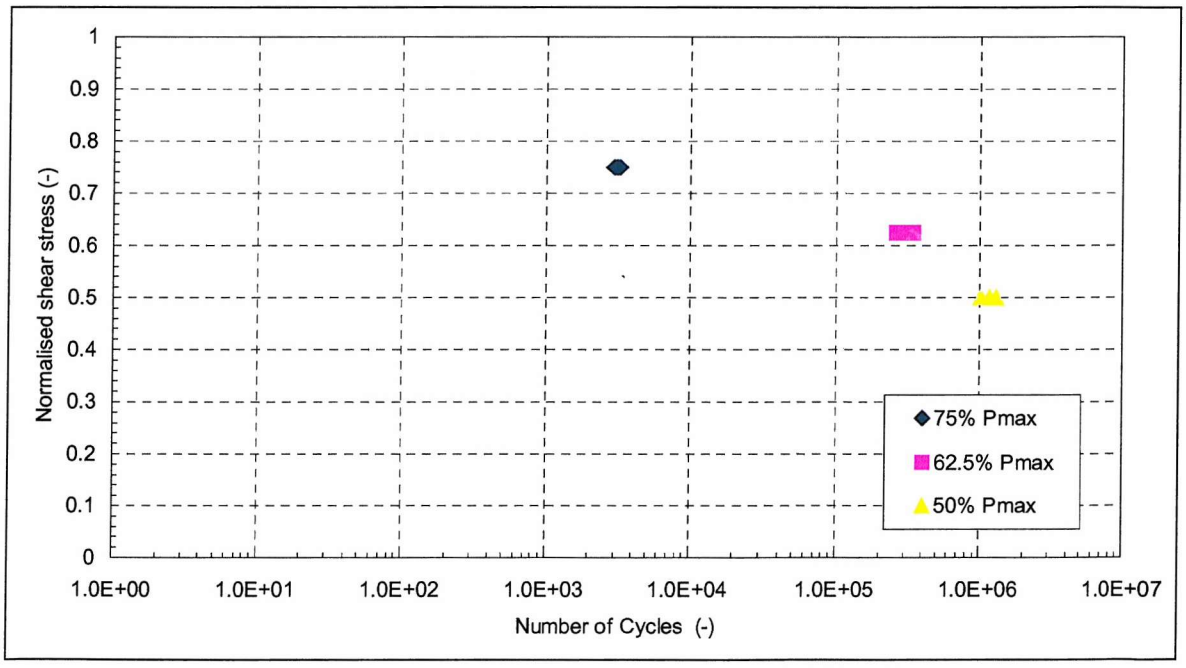

Figure 78: S-N curves

11.5 Numerical analysis of shear crack in foam core sandwich beams

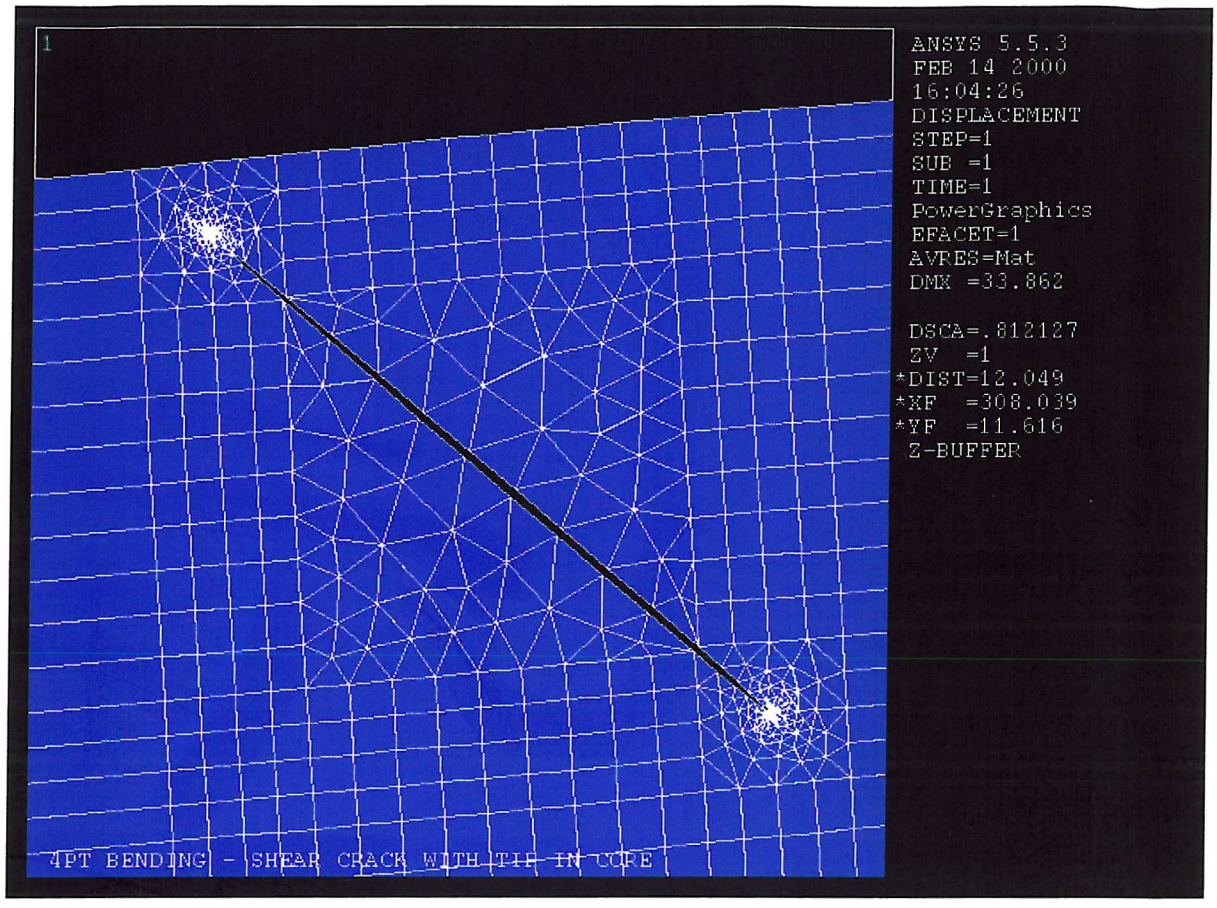

Figure 79: Deformed shape of simulated crack in a 4PTB specimen from FEA

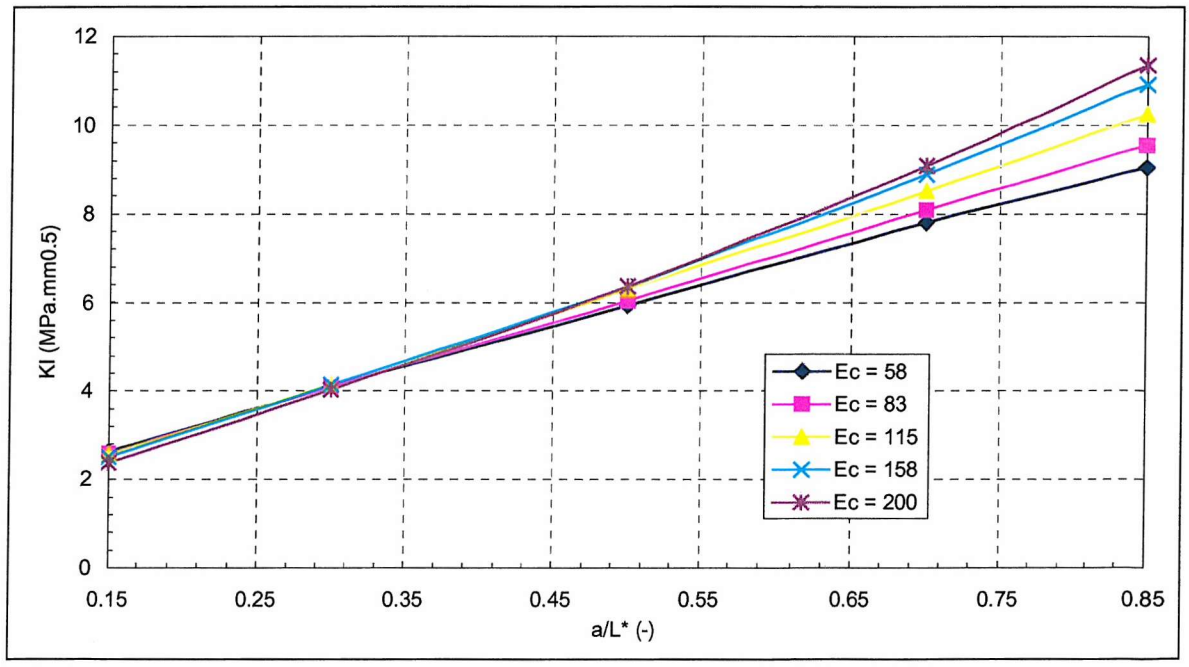

Figure 80: K_I vs. a/L* - K_I sensitivity to core elastic moduli E_c and G_c

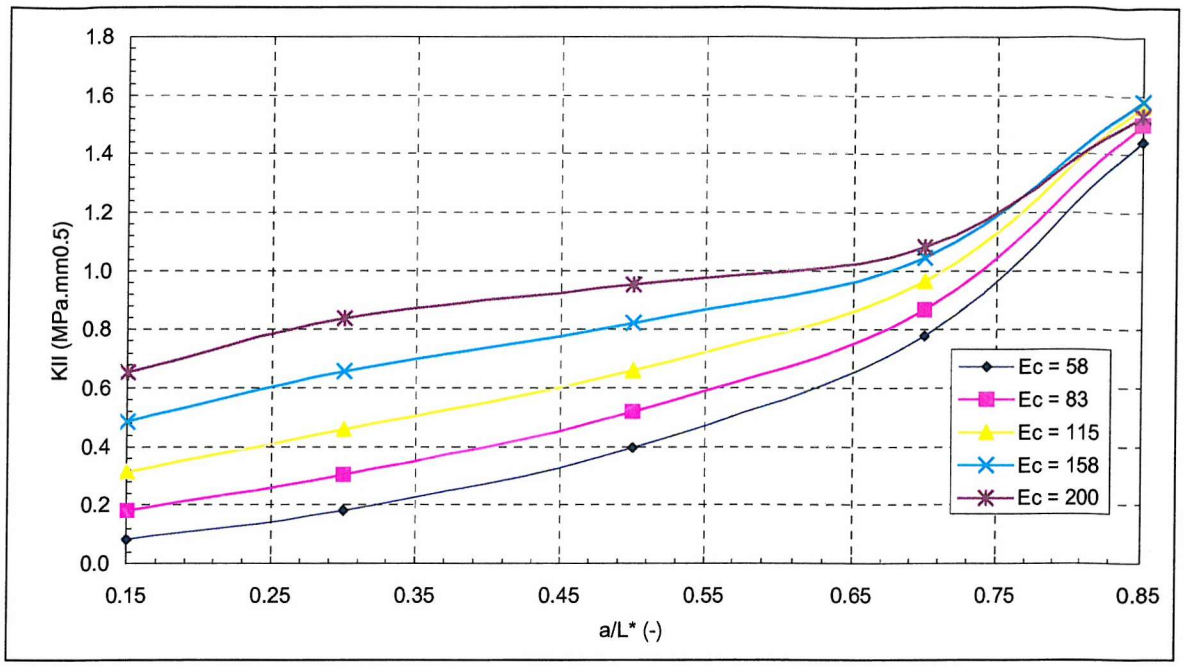

Figure 81: K_{II} vs. a/L* - K_{II} sensitivity to core elastic moduli E_c and G_c

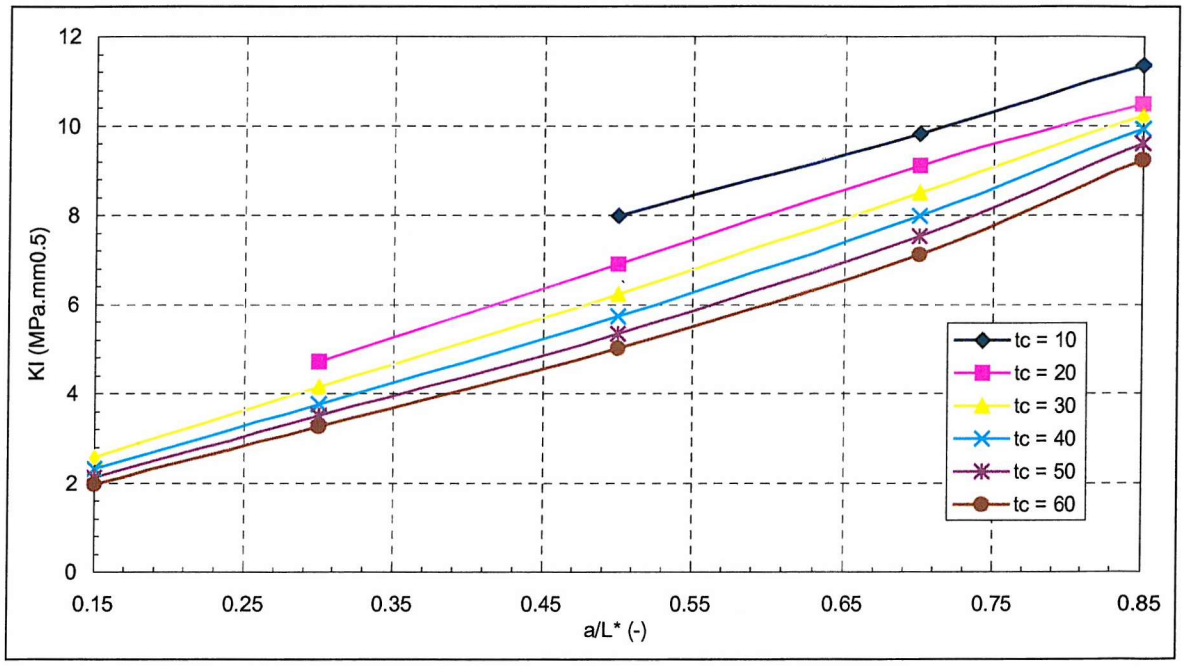

Figure 82: K_I vs. a/L* - K_I sensitivity to core thickness t_c

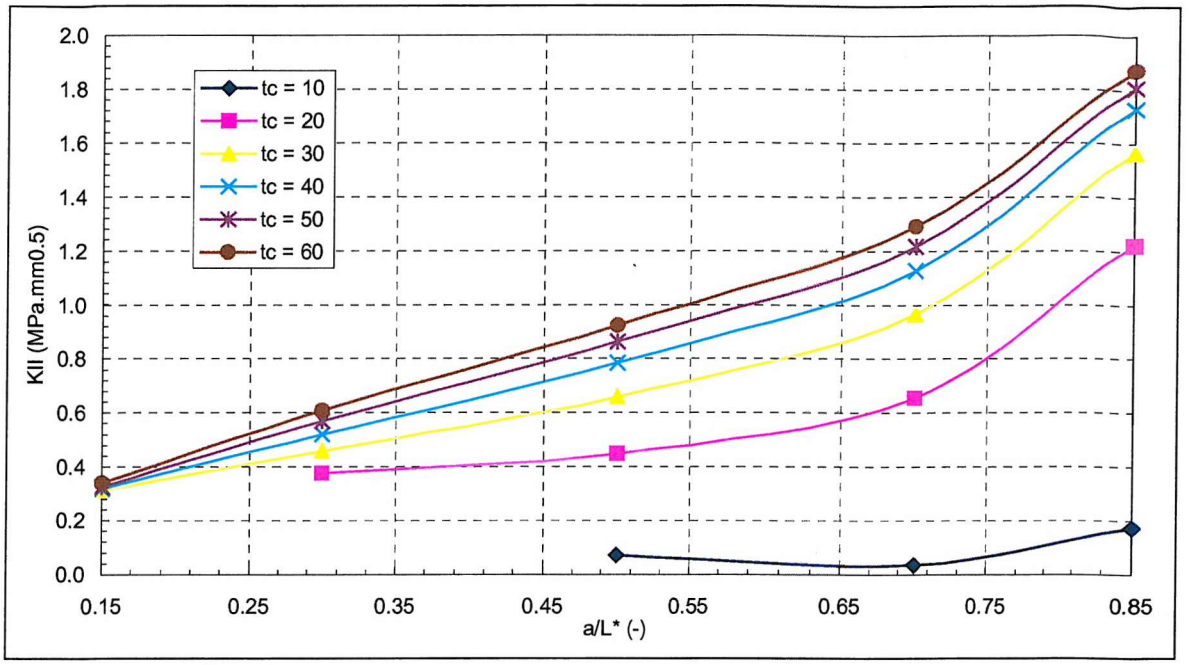

Figure 83: K_{II} vs. a/L* - K_{II} sensitivity to core thickness t_c

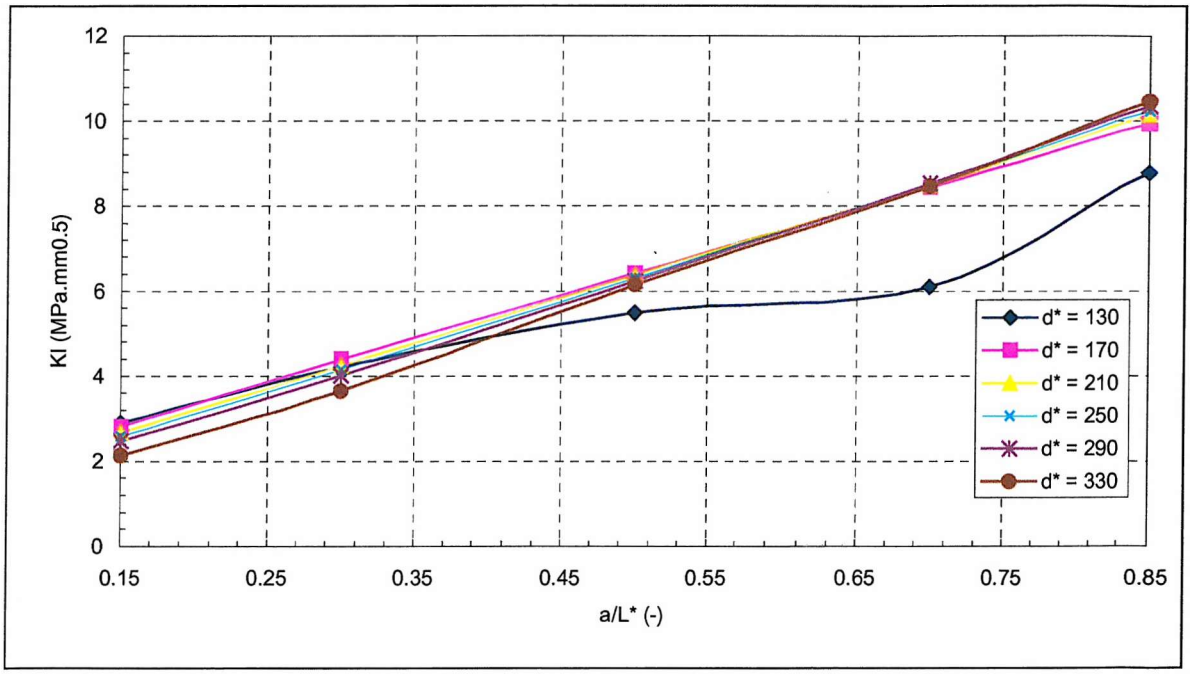

Figure 84: K_I vs. a/L* - K_I sensitivity to longitudinal crack position d*

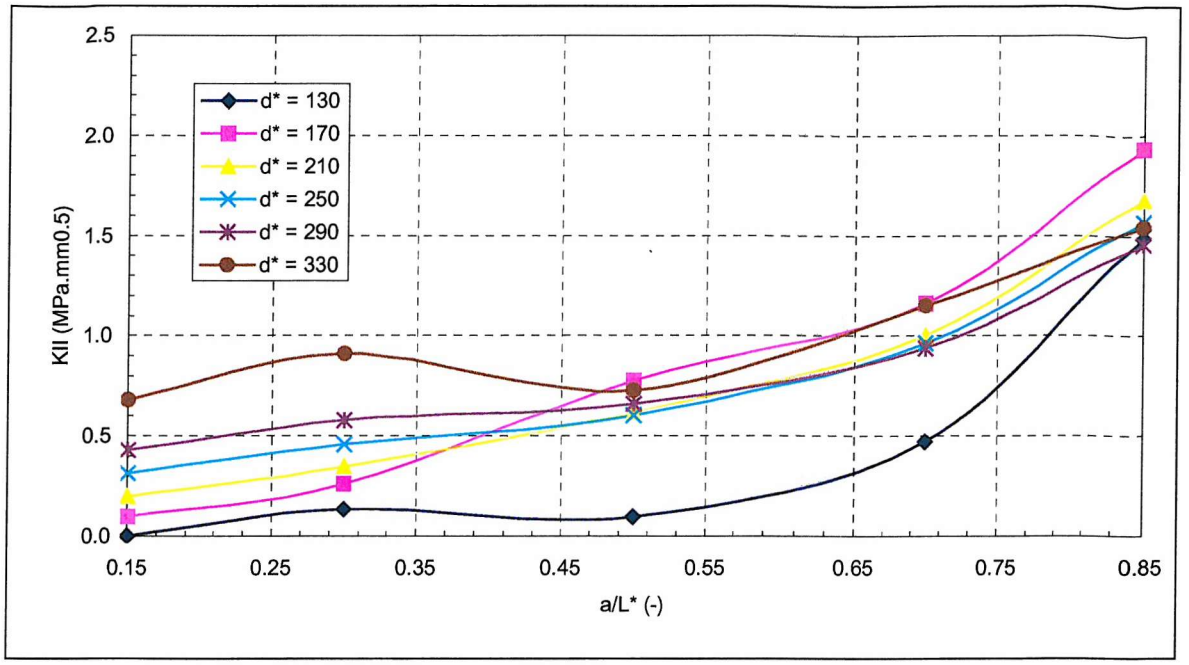

Figure 85: K_{II} vs. a/L* - K_{II} sensitivity to longitudinal crack position d*

12 REFERENCES

[1] ASTM, *Annual book of ASTM Standards*, Technical Report, American Society for Testing and Materials, Philadelphia, Pennsylvania, USA, 1991

[2] SMITH, C., *Design of Marine Structures in Composite Materials*, Elsevier Applied Science, London, 1990

3 GULLBERG, O., OLSSON, K., *Design and Construction of GRP Sandwich Ship Hulls,* Maritime Structures, Vol.3, No.2, 1990

[4] OLSSON, K., LÖNNÖ, A., *Sandwich Construction - Recent Research & Development,* Proc. 1st Int. Conf. on Sandwich Construction, Vol.2, Florida, USA, March 1991

[5] KUENZI, E. W., *Minimum Weight Structural Sandwich*, U.S. Forest Service Res., Note FPL-086

[6] UENG, C. E. S., LIU, T. L., *Least Weight of a Sandwich Panel*, in R. R. Craig(Ed), Proc. ASCE Engineering Mechanics Division 3rd Speciality Conf., University of Texas at Austin, September 17-19, 1979, ASCE, New York, pp 41-44

[7] FROUD, G.R., *Your Sandwich Order, Sir?*, Composites, 11 (1980) 133

[8] CIBA-GEIGY, *Aeroweb Honeycomb Sandwich Design*, Inst. Sheet AGC33a, Part 2, 1980, Bonded Structures Division, Duxford, Cambridge, Cambridge

[9] ALLEN, H. G., *Analysis and Design of Structural Sandwich Panels*, Pergamon, Oxford, 1969

[10] HALL, D.J., and ROBSON, B.L., *A Review of the Design and Materials Evaluation Programme for the GRP/Foam Sandwich Composite Hull of the RAN Minehunter*, Composites, 15 (1984) 266-276

[11] HONG, C. S., and JEONG, K. Y., *Stress Intensity Factors in Anisotropic Sandwich Plate with a Part-Through Crack under Mixed-mode Deformation*, Eng. Fract. Mech., 21 (2) (1985) 285-292

[12] AKERS, P., *The Efficiency of Sandwich Struts Utilising Calcium Alginate Core*, Rep. Memo. 2015, 1945, U.K. Aeronautical Research Council, Farnborough, Hants

[13] WITTRICK, W. H., *A Theoretical Analysis of the Efficiency of Sandwich Construction Under Compressive End Load*, Rep. Memo. 2015, 1945, U.K. Aeronautical Research Council, Farnborough, Hants

[14] WRZECIONIARZ, P. A., *Stability Investigations of Variable Core Sandwich*, J. Eng. Mech., 109 (1983) 1460-1471

[15] COMPOSITES I, *Seahorse*, 159, May 93, p. 49

[16] COMPOSITES II, *Seahorse*, 160, June 93, p. 34

[17] SHENOI, R., *Principal Aspects Concerning Structural Design of High Speed Craft,* Proc. Int. Conf. on High Speed Passenger Craft, RINA, London, 15-16 June 1993

[18] HAYMAN, B., *Response of Sandwich Structures to Slamming and Impact Loads,* Composite Materials in Marine Structures, Vol.2, Cambridge University Press, Cambridge, 1991, p.161-176

[19] HARVEY, G., *Composite Construction: A Design Process Guide*, International Conference on Lightweight Materials in Naval Architecture, RINA, Southampton, 28-29 February 1996

[20] COMPOSITES III, *Seahorse*, 161, Jul. 93, p. 41

[21] GIBSON, L., J., and ASHBY, M., F., *Cellular Solids - Structures and Properties*, Pergamon, Oxford, 1988

[22] BRANNER, K., *Capacity and Lifetime of Foam Core Sandwich Structures*, Ph.D. Thesis, Department of Ocean Engineering, Technical University of Denmark, Lyngby, Denmark, 1996

[23] FOWLKES, C.W., *Fracture Toughness Tests of Rigid Polyurethane Foam*, Int. J. Fract. 10 (1974), 99-108

[24] ASHBY, M. F, GIBSON, L.J., and MAITI, S.K., *Fracture Toughness of Brittle Cellular Solids*, Scr. Metall., 18 (1984), 213-217

[25] McINTYRE, A., ANDERTON, G. E., *Fracture Properties of Rigid Polyurethane Foam over a Range of Densities*, Polymer, Vol. 20, 1979, pp. 247-253

[26] ZENKERT, D., BACKLUND, J., *PVC Sandwich Core Materials: Mode-I Fracture Toughness*, Composites Sc. and Tech., Vol. 34, 1989, pp. 225-242

[27] ZENKERT, D., *PVC Sandwich Core Materials: Fracture Behaviour under Mode-II and Mixed-mode Conditions*, Materials Science and Engineering, A108 (1989), pp. 299-240

[28] SIH, G.C., *Strain Energy Density Factor applied to Mixed-mode Crack Problems*, Int. J. Fract., Vol. 10, 305, 1974

[29] SIH, G.C., *Some Basic and New Concepts in Fracture Mechanics*, Eng. Fract. Mech., Vol. 5, 365, 1973

[30] WILLIAMS, J.G., *Fracture Mechanics of Polymers*, Ellis Horwood, Chichester, West Sussex, UK, 1984, 74

[31] GRENESTEDT, J., HALLSTRÖM, S., and KUTTENKEULER, J., *On Cracks Emanating from Wedges in Expanded PVC Foam*, Eng. Fract. Mech., Vol.54, No. 4, 445-456, 1996

[32] CARLSSON, L. A., SENDLEIN, L. S., MERRY, S. L., *Characterisation of Face Sheet/Core Shear Fracture of Composite Sandwich Beams*, J. of Composite Materials, Vol. 25, 1991, pp. 101-116

[33] CARLSSON, L. A., PRASAD, S., *Interfacial Fracture of Sandwich Beams*, Eng. Fract. Mech., Vol. 44, No. 4, 1993, pp.581-590

[34] PRASAD, S., CARLSSON, L. A., *Debonding and Crack Kicking in Foam Core Sandwich Beams - I Analysis of Fracture Specimens*, Eng. Fract. Mech., Vol. 47, No. 6, 1994, pp. 813-824

[35] ZENKERT, D., *Strength of Sandwich Beams Interface Debondings*, Report No. 90-8, Dept. of Aeronautical Structures & Materials, Royal Institute of Technology, Stockholm, Sweden

[36] OSGOOD, C., *Fatigue Design,* Int. Series on Strength & Fracture of Materials & Structures, Pergamon Press, 1982

[37] CURTIS, P., *The Fatigue Behaviour of Fibrous Composite Materials,* Journal of Strain Analysis, Vol. 24, 1989

[38] CURTIS, P., *Theory Predictions of Failure Mechanics and Strength,* Composite Materials in Marine Structures, Vol. 1, loc cit 18

[39] SIMS, G., *Test Procedure & Standards,* Composite Materials in Marine Structures, Vol. 1, loc cit 18

[40] ASTM, *Standard Test Method for Shear Fatigue of Sandwich Core Materials*. C394-62, ASTM Standards & Literature References for Composite Materials, 2nd Edition, pp 149-150, 1990

[41] OLSSON, K., LÖNNÖ, A., *Sandwich Construction - Recent Research & Development*, Vol.2, Proc. 2nd Int. Conf. on Sandwich Constructions, Florida, USA, March 1991

[42] HAYMAN, B., SUND, O., *Shear Properties of GRP Sandwich Beams subjected to Slamming Loads*, Vol. 2, loc cit 18

[43] BUENE, L., ECHTERMEYER, A., *Assessment of Long Term Effects of Slamming Loads on FRP Sandwich Panels*, Proc. 1st Int. Conf. on Fast Sea Transportation (FAST'91), Trondheim, Norway, 1991, Vol. 1, pp365-379

[44] ECHTERMEYER, A., BUENE, L., *Four-point-bend test of GRP Sandwich Beams*, Nordic Composites and Sandwich Meeting, Stockholm, Sweden, 31-37, 1991

[45] SHENOI, R.A., AKSU, S., *Flexural Sandwich Characteristics of FRP Sandwich Beams*, Fatigue Fract Eng. Mater. Struct, Vol. 16, No.6, 649-662.

[46] BURMAN, M., *On Crack Initiation and Growth in Cellular Foams subjected to Fatigue Shear Loading*, Proc. of Fatigue'96, 1549-1554, 1996

[47] BURMAN, M., *Fatigue Crack Initiation and Propagation in Sandwich Structures*, Ph.D. Thesis, KTH, Report 98-29, Stockholm, Sweden, 1998

[48] NOBLE, F.W., *Fatigue Crack Growth in Polyurethane Foam*, J. of Materials Science, 16, 1981, 1801-1808

[49] YAU, S.S., MAYER, G., *Fatigue Crack Propagation in Polycarbonate Foam*, J. of Materials Science and Engineering, 78:111-114, 1986

[50] FLECK, N., PARKER, P., *Part II Project Report*, Cambridge University Engineering Department, 1988 (un-available)

[51] OLSSON, K-A., LÖNNÖ, A., *Test Procedure for Foam Core Materials,* Proc. 1st Int. Conf. on Sandwich Constructions, Eds. K-A. Olsson and R.P. Reichard, EMAS Ltd, UK, pp293 – 318, 1989

[52] HEDLUND-ASTROM, A., OLSSON, K-A., SORENSSON, L., *Fatigue Testing of Sandwich Core Material DIVINYCELL H250,* ILK Report A-61, Department of Aeronautics, KTH, Stockholm, Sweden, 1993

[53] SCHOLTE, H., *Fatigue Characteristics*, Composite Materials in Marine Structures, Vol. , loc cit 18

[54] TALREJA, R., *Fatigue of Composite Materials,* Technomic Publishing Company, Lancaster, USA, 1987

[55] OGIN, S., *Fatigue in Composite Materials,* Composite Materials Technology, University of Surrey, July 1989

[56] REIFSCNEIDER, K., TALUG, A., *Analysis of Fatigue Damage in Composite Materials,* Int. Jour. of Fatigue, Jan 1980

[57] ALLEN, H., *Theory of Sandwich Beams and Plates,* Composite Materials in Marine Structures, Vol. 1, loc cit 18

[58] SMITH, C., *Design of Marine Structures in Composite Materials*, Elsevier Applied Science, London, 1990

[59] SHENOI, R., *An Engineering Approach to the Prediction of the Elastic Properties of a Laminate*, Composite Materials in Marine Structures, Vol. 1, loc cit 18

[60] PHILIPPS, L., *Design with Advanced Composite Materials*, The Design Council, London, 1989

[61] BROUTMAN, L., AGARWAL, B., *Analysis and Performance of Fibre Composites*, John Wiley & Sons Inc, 1990

[62] ALLEN, H., RAYBOULD, K., *High Performance Composites and their Effectiveness in Sandwich Panels*, Proc. 6th Int. Conf. On High Speed Surface Craft, London, Jan 1988

[63] CAPRINO, G., TETI, R., *Sandwich Structures Handbook*, Il Prato, April 1989

[64] ZENKERT, D., *An Introduction to Sandwich Construction*, EMAS, 1995

[65] ZENKERT, D., *The Handbook of Sandwich Construction*, EMAS, 1997

[66] VINSON, J.R., *The Behaviour of Sandwich Structures of Isotropic and Composites*, Materials, Technomic, Lancaster, Pennsylvania, USA, 1999

[67] ALLEN, H., *Analysis and Design of Structural Sandwich Panels*, Pergamon Press, London, 1969

[68] PAGANO, N., *Exact Solution for Rectangular Bi-directional Composite and Sandwich Plates*, Journal of Composite Materials, p.20, 1970

[69] MACE, M., *A Sandwich Plate Theory*, Proc. Int. Conf. on Nautical Construction with Composite Materials, IFREMER, Paris, France, 7-9 December 1992

[70] THEULEN, J., PEIJS, J., *Optimisation of Bending Stiffness & Strength of Composite Sandwich Panels*, Composites Structures, Elsevier Science Publishers, 1990

[71] GRIFFITH, A. A., *The Phenomenon of Rupture and Flow in Solids*, Phil. Trans. Roy. Soc., London, A-221, pp163-198, 1920

[72] SNEDDON, I. N., *The Distribution of Stress in the Neighbourhood of a Crack in an Elastic Solid*, Proceedings, Royal Society of London, Vol. A-187, 1946, pp. 229-260

[73] DAVALOS, J., BARBERO, E., *A 2-D Laminated Finite Element with Layer Wise Constant Shear*, Vol. 1, Proc. 2nd Int. Conf. on Sandwich Constructions, Florida, USA, March 1991

[74] STARLINGER, A., RAMMERSTORFER, F., *A Finite Element Formulation for Sandwich Shells Accounting for Local Failure Phenomena*, Vol. 1, Proc. 2nd Int. Conf. on Sandwich Constructions, Florida, USA, March 1991

[75] ZHENG-CHANG, L., *Finite Element Analysis of Sandwich Plates*, Vol. 1, Proc. 2nd Int. Conf. on Sandwich Constructions, Florida, USA, March 1991

[76] ROTSCHILD, Y., ECHTERMEYER, A., *Simulation of Field of Plastic Flow of 3-D Sandwich Foam Cores*, Vol. 1, Proc. 2nd Int. Conf. on Sandwich Constructions, Florida, USA, March 1991

[77] DAMONTE, R., *Finite Element Analysis of Composites*, Composite Materials in Marine Structures, Vol. 1, loc cit 18

[78] SHIH, C.F., MORAN, B., and NAKAMURA, T., *Energy Release Rate along a 3-dimensional Crack Front in a Thermically Stressed Body*, Int. J. of Fract., Vol.30, 1986, 79-102

[79] ZENKERT, D., *Damage Tolerance of Foam Core Sandwich Constructions*, PhD. Thesis, Dept. of Aeronautical Structures and Materials, Report No.90-8, Royal Institute of Technology, Stockholm, 1990

[80] ZENKERT, D., FALK, L., *Interface Debonds in Foam Core Sandwich Beams and Panels*, Dept. of Aeronautical Structures and Materials, Report No. 92-23 , Royal Institute of Technology, Stockholm, 1990

[81] FALK, L., *Foam Core Sandwich Panels with Interface Disbonds,* Composites Structures, Vol.28, pp. 481-490, 1994

[82] AIREX Manual, Material Properties

83 ASTM E 399 -83, *Standard Test Method for Plane Strain Fracture Toughness and Strain Energy Release Rate of Metallic Materials*, Annual Book of ASTM Standards, Philadelphia, 1983

[84] ASTM D 5045-95, *Standard Test Method for Plane Strain Fracture Toughness and Strain Energy Release Rate of Plastic Materials*, Annual Book of ASTM Standards, Philadelphia, 1995

[85] ERDOGAN, F., SIH, G.C., *On the Crack Extension in Plates under Plane Loading and Transverse Shear*, J. of Basic Engineering 85, 519-525

[86] FISHER, K.F., *On the Formulation of a Principal Strain Criterion in Crack Fracture Mechanics*, Int. J. of Fracture, 17, 1981, R3-R6

[87] RICHARD, H.A., *Specimen for Investigation of Biaxial Fracture and Fatigue Processes,* Proc. 2nd Int. Conf. on Biaxial/multiaxial Fatigue, Sheffield, 1985

[88] STIBE, M., *Fracture toughness of Dyvinicell H100, H130 and H200,* Report TR91-44, Barracuda Technologies AB, Sweden, 1991

[89] SHENOI, R.A., WELLICOME, J.F. (Eds.), *Composite Materials in Maritime Structures*, Ocean Technology Series, Cambridge University Press, 1993

[90] DIVINYCELL, *Technical Manual H-Gradel*, Divinycell International AB, laholm, Sweden, 1991

[91] NOURY, P.M., SHENOI, R.A., and SINCLAIR, I., *On Mixed-mode Fracture of PVC Foam*, Int. J. of Fracture, 92: 131-151, 1998

[92] ASTM E647-93, *Standard Test Method for Measurement of Fatigue Crack Growth Rates*, Annual Book of ASTM Standards, Philadelphia, 1983

[93] LIU, H.W., *Shear Fatigue Crack Growth: a Literature Survey*, Fatigue Fract. Eng. Mat. Struct., vol. 8, No. 4, pp295-313, 1985

[94] ASTM, *Standard Test Method for Flexural properties of Flat Sandwich Constructions.* C393-62, ASTM Standards and Literature References for Composite Materials, 2nd Edition, 1990

[95] CLARK, S.D., *Comparative Study on the Performance of Sandwich Structures*, Proc. 4th Int. Conf. Sandwich Construction, June 9-11, 1998, Stockholm, Sweden

[96] TRIANTAFILLOU, T.C., GIBSON, L.J., *Failure Mode Maps for Foam Core Sandwich Beams*, Materials Science and Engineering, 95 (1987) 37-53